

Master Thesis, Department of Geosciences

Reservoir characterization of the Upper Triassic Snadd Formation in the southwestern Barents Sea

*A comparison study between Bjarmeland Platform and
Hammerfest Basin deposits*

Chloé Marcilly



UNIVERSITY OF OSLO

FACULTY OF MATHEMATICS AND NATURAL SCIENCES

Reservoir characterization of the Upper Triassic Snadd Formation in the southwestern Barents Sea

*A comparison study between Bjarmeland Platform and
Hammerfest Basin deposits*

Chloé Marcilly



Master Thesis in Geosciences

Discipline: Geology

Department of Geosciences

Faculty of Mathematics and Natural Sciences

University of Oslo

December 1st, 2016

© **Chloé Marcilly, 2016**

Tutor(s): Prof. Jens Jahren, Phd. Lina Hedvig Line

This work is published digitally through DUO – Digitale Utgivelser ved UiO

<http://www.duo.uio.no>

It is also catalogued in BIBSYS (<http://www.bibsys.no/english>)

All rights reserved. No part of this publication may be reproduced or transmitted, in any form or by any means, without permission.

ACKNOWLEDGMENTS

First, I would like to express my deepest thanks to my supervisor Professor Jens Jahren. Thank you very much to have created this thesis for me but also for your help in its elaboration. I learned a lot by doing it and developed a pronounced taste for research.

I would like to thank my co-supervisor and PhD student Lina Hedvig Line who has been a great support all along this thesis. Thank you very much for your kindness and all the time you spent helping me. I really enjoyed elaborating theories with you.

I would also like to express my gratitude to Berit Løken Berg for helping with the SEM analysis, to the PhD student Beyene Girma Haile for his help during the preparation of the XRD analysis. I would also like to thank all the teachers and staff of the University of Oslo to have made my stay here such a great and interesting experience. Mostly, my friends and colleagues of the room 214 for all the nice moments spent with them.

Among my friends, I would like to thank particularly Timea Gyenis, my co-Barents Sea student buddy. A special thank goes to my friend Anna Clark to have made me better with my English. Thanks a lot!

I owe a particular thank to my family, especially my mum and sister: *Merci de m'avoir soutenue, écoutée, calmée et consolée durant les durs moments de cette année. Je vous aime plus que tout.*

The biggest of my thanks goes to my boyfriend and co-geologist, Orhan Mahmic. Thank you so much for all those evenings talking about the thesis, for your patience and understanding when my nerves were reaching their limits. Without you, I would have drowned in the Barents Sea.

Tusen Takk – Merci

Chloé

ABSTRACT:

The Barents Sea is the new target area for the oil industry, particularly the Triassic and Jurassic strata. Deeply buried sandstone reservoirs have proved to have good quality in the North Sea due to presence of chlorite coating. The aim of this study is to investigate the processes and factors influencing the reservoir quality of the Late Triassic Snadd Formation in the southwestern Barents Sea. The Snadd Formation includes a large range of depositional environments and this study highlights their impact on the reservoir quality by comparing between datasets from the Hammerfest Basin and the Bjarmeland Platform. This thesis is part of the project **Trias North** reconstructing the Triassic Barents shelf.

Core material and well data from two wells were examined using sedimentological and petrographical as well as petrophysical approach. The sedimentological and petrographical analyses are composed of core logging, optical and scanning electron microscopy (SEM) associated with X-ray diffraction. Wireline logs were used to make the petrophysical analysis.

Both studied locations show poor reservoir potential for oil due to the low porosity resulting from high compaction and abundant clay minerals from deposition and infiltration. Those clay minerals greatly participate to the reduction of the porosity and permeability due to burial diagenesis processes such as illitisation and quartz cement. The thick sandstone deposits of the Bjarmeland Platform, even if the overall porosity is close to the 10% cut off, can still represent a good reservoir for gas production. The potential stacking of the fluvial channel deposits may reinforce the value of the reservoir.

This study proves that the initial composition of the deposits, as well as their depositional environments, is decisive for the reservoir quality as they govern the diagenetic processes controlling it. Some particular features proper to each well such as the presence of dolomite and sphaerosiderites have been investigated in view to qualify their influence on the local reservoir quality.

Table of Contents

TABLE OF CONTENTS	- 7 -
I. INTRODUCTION	- 10 -
II. GEOLOGICAL SETTINGS	- 11 -
2.1 STUDIED AREA:	- 11 -
2.2 EVOLUTION OF THE BARENTS SEA WITH FOCUS ON THE TRIASSIC	- 12 -
2.2.1 <i>Triassic times in the Barents Sea</i>	- 12 -
2.2.2 <i>The Kapp Toscana Group and Snadd formation:</i>	- 14 -
2.2.3 <i>Depositional environments of the Snadd formation:</i>	- 14 -
2.3 POST-TRIASSIC TIMES	- 16 -
2.4 STRUCTURAL ELEMENTS CONCERNED IN THIS STUDY	- 18 -
III. THEORETICAL BACKGROUND	- 20 -
3.1 RESERVOIR QUALITY AND DIAGENESIS	- 20 -
3.2 DIAGENESIS IN SANDSTONES AND MUDSTONES :	- 21 -
3.2.1 <i>Early diagenesis processes</i> :	- 21 -
3.2.2 <i>Intermediate burial diagenesis: 2 - 3.5 km (50-120°C)</i>	- 27 -
3.2.3 <i>Deep diagenesis: > 3,5 - 4 Km (>120°C)</i>	- 28 -
3.2.4 <i>Uplift related processes:</i>	- 29 -
3.3 POROSITY PRESERVING PROCESSES:	- 30 -
IV. METHODS	- 32 -
4.1 SEDIMENTOLOGICAL CORE LOGGING:	- 32 -
4.2 MINERALOGICAL AND PETROGRAPHICAL ANALYSES:	- 32 -
4.2.1 <i>Thin section analysis</i> :	- 33 -
4.2.2 <i>Point counting</i> :	- 34 -
4.2.3 <i>Bulk XRD:</i>	- 36 -
4.2.4 <i>Clay fraction analyses:</i>	- 39 -
4.2.5 <i>Scanning Electron Microscope (SEM):</i>	- 39 -
4.3 TEXTURAL ANALYSIS :	- 40 -
4.3.1 <i>Grain size, sorting and particle shape:</i>	- 40 -

4.3.2	<i>Grain contacts:</i>	- 42 -
4.3.3	<i>Porosity estimation :</i>	- 43 -
4.4	PETROPHYSICAL ANALYSES :	- 43 -
4.4.1	<i>Compaction trend :</i>	- 43 -
4.4.2	<i>Geothermal gradient :</i>	- 44 -
4.4.3	<i>Well logs :</i>	- 44 -
V.	RESULTS:	- 47 -
5.1	SEDIMENTOLOGICAL ANALYSIS:	- 47 -
5.1.1	<i>Facies description :</i>	- 51 -
5.1.2	<i>Facies association :</i>	- 55 -
5.2	PETROGRAPHIC ANALYSIS :	- 57 -
5.2.1	<i>Well 7122/6-2: Hammerfest Basin</i>	- 57 -
5.2.2	<i>Well 7226/2-1: Bjarmeland Platform</i>	- 68 -
5.3	PETROPHYSICAL ANALYSIS :	- 82 -
5.3.1	<i>Compaction trend:</i>	- 82 -
5.3.2	<i>Gamma log and formations:</i>	- 82 -
5.3.3	<i>Sonic log:</i>	- 85 -
5.3.4	<i>Density log:</i>	- 87 -
5.3.5	<i>Neutron log:</i>	- 88 -
5.3.6	<i>Porosity estimation :</i>	- 88 -
5.3.7	<i>Uplift estimation:</i>	- 89 -
VI.	DISCUSSION :	- 92 -
6.1	PROVENANCE AND DEPOSITIONAL ENVIRONMENTS:	- 92 -
6.1.1	<i>Provenance and transport:</i>	- 92 -
6.1.2	<i>Depositional environment: Well 7122/6-2</i>	- 93 -
6.1.3	<i>Depositional environment: Well 7226/2-1</i>	- 95 -
6.2	INTERGRANULAR VOLUME EVOLUTION AND COMPACTIONAL REGIMES:	- 97 -
6.2.1	<i>Well 7226/2-1: Bjarmeland Platform</i>	- 97 -
6.2.2	<i>Well 7122/6-2: Hammerfest Basin</i>	- 100 -
6.2.3	<i>Mechanical compaction:</i>	- 101 -

6.2.4 *Origin of the matrix:*..... - 102 -

6.2.5 *Chemical compaction: formation of cements* - 104 -

6.3 PERMEABILITY EVOLUTION:..... - 117 -

6.3.1 *Influence of the chlorite coating:*..... - 118 -

6.3.2 *Influence of other clay minerals diagenesis:* - 118 -

6.3.3 *Influence of the dolomite diagenesis :* - 119 -

6.3.4 *Influence of the sphaerosiderites and siderite cement:*..... - 119 -

6.4 GEOGRAPHICAL EXTENT OF THE SNADD FORMATION RESERVOIR QUALITY..... - 121 -

VII. CONCLUSION:..... - **123** -

REFERENCES: - **123** -

APPENDICES..... - **132** -

I. Introduction

The Barents Sea has been an area of interest for the petroleum industry for over half a century. The first geophysical investigation started during the 1970's and the first drilling in the 1980's.

The Norwegian Barents Sea represents an area covering 230 000 km², 1,5 times the Norwegian section of the North Sea. More than 260 billion of m³ of gas with minor oil have been proven to be contained within the Barents Sea, mainly in Jurassic sandstones (Doré, 1995). However, some gas has been discovered in the Triassic sandstones in the Hammerfest Basin and nearby areas (Johansen et al, 1992), making the Triassic strata a new interesting target. The Triassic is believed to have potential for reservoir and source rock intervals due to algal blooms found in the Mid-Triassic strata in the Northern Barents Sea (Høy & Lundschieen, 2011; Glørstad et al, 2010).

The aim of this thesis is to increase the understanding of the distribution of the Late Triassic Snadd formation reservoir potential within the Southwestern Barents Sea. Even if this formation is well known for its sandstone intervals, it also displays large depositional heterogeneities and the reservoir quality cannot be considered as equal in the Barents Sea. The objective of this thesis is to highlight how such heterogeneities affect the reservoir quality within the Snadd formation, as well as the factors and processes linked with it.

The characterization of the reservoir is based on the description and interpretation of sedimentological core logs, petrophysical wireline logs and collected samples. The combined results of those analyses are discussed in a sedimentological and diagenetic evolution aiming to define the actual reservoir quality.

II. Geological settings

2.1 Studied area:

The Barents Sea is defined as the area between the Novaya Zemlya, Frantz Josef land, Svalbard archipelago and the eastern margin of the deep Atlantic Ocean (Doré, 1995). The area is defined by Doré (1995) as “a complex mosaic of platform areas and basins”. The basins are separated by deep-seated faults, structural highs and sub-platforms (Gabrielsen et al, 1990).

The south-western part of the Barents Sea has been the subject of many studies. The Triassic and Jurassic deposits have proved their potential in this area (Doré, 1995). The study area is located in two separate areas: the Hammerfest basin with the well 7122/6-2 and the Bjarmeland platform with the well 7226/2-1. The locations of the two cores are shown in Figure 1.

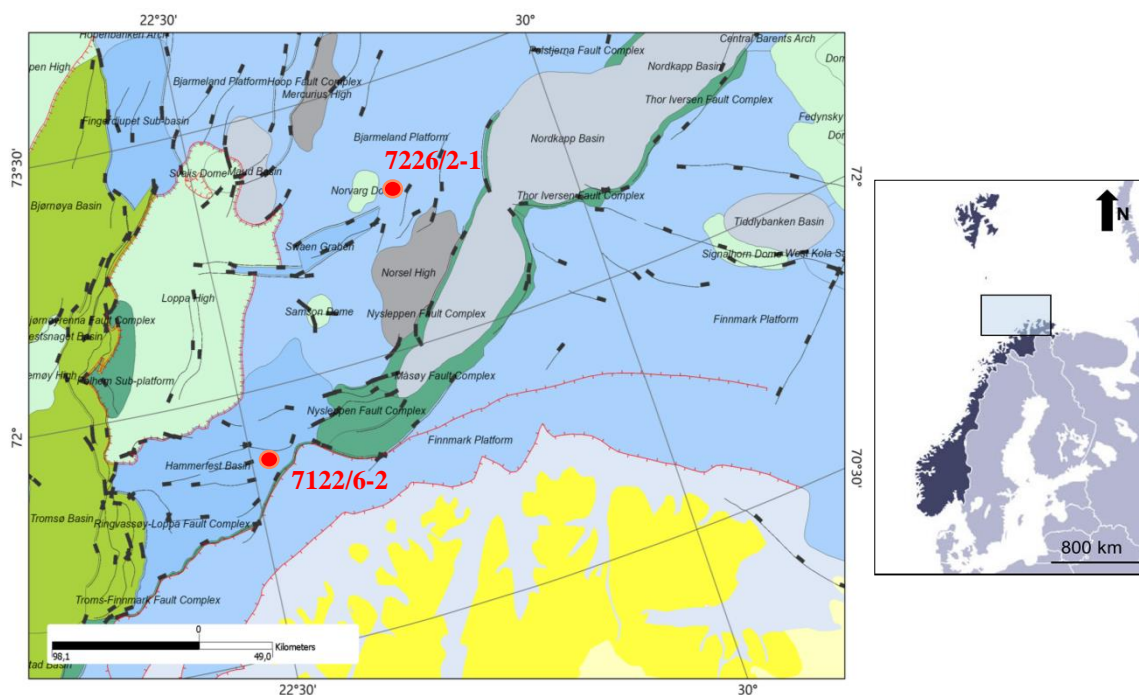


Figure 1: Map of the Southwestern part of Barents Sea showing the main structural elements from the Norwegian Petroleum Directorate website (npd.no). The red dots indicate the location of the wells used in this study.

2.2 Evolution of the Barents Sea with focus on the Triassic

Two major orogenies are responsible for the complex structure of the Barents Sea. During the Late Silurian–Early Devonian boundary, the continental plates of Laurentia (today Greenland and North America) and the Baltic plate (today Scandinavia and Western Russia) collided to form the Lurasian continent. The Caledonian orogeny and the closing of the Iapetus Ocean are the result of this collision (Doré, 1995). The second orogeny involved is the Uralian orogeny which occurred 240 million years ago, during the Permian-Triassic times (Scotese et al, 1987).

2.2.1 Triassic times in the Barents Sea

The Triassic in the Barents Sea is represented by five formations (Fig.2). Shallow marine to continental sandstones are identified as reservoir rocks and are present in all five formations (Glørstad et al, 2011).

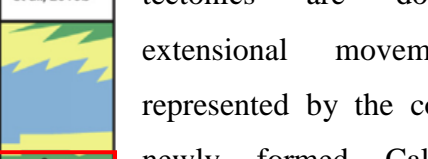
Ma.	Chronostratigraphy	Group	Formation	2nd order seq., Glørstad-Clark et al., 2010	Lithostrat., Henriksen et al., 2010b
208	Rhaetian	Kapp Toscana	Tubåen		
			Fruholmen		
227	Norian				
237	Carnian		Snadd	S5	
	Ladinian			S4	
242	Anisian	Sasendalen	Kobbe	S3	
	Olenekian		Klappmyss	S2	
252	Induan		Havert	S1	

Figure 2: Lithostratigraphic Triassic sequence modified from Henriksen et al (2011) in Glørstad et al (2011). The red square represents the time frame for this study.

The Late Paleozoic and Mesozoic tectonics are dominated by extensional movements, firstly represented by the collapse of the newly formed Caledonian and Uralian orogenic belts and later by the breakup of the Pangean supercontinent. These tectonic events created major rift basins and inverted series of platforms and structural highs (Doré, 1995).

The Late-Permian to Early-Triassic period was subjected to an intensification of this extensional phase leading to uplift and tilting of the Loppa High. This tectonic displacement placed the Loppa High as the western limit of the south-western basin during the first half of the Triassic (Skjold et al, 1998; Glørstad et al, 2010; Glørstad et al, 2011). The Loppa High was then uplifted and eroded during the

Triassic (Johansen et al, 1992). Nevertheless, the Permo-Triassic period is considered a globally tectonically quiet period associated with a regional subsidence of the Southwestern Barents Sea (Faleide et al, 1984; Johansen et al, 1992; Høy and Lunschien, 2011; Glørstad et al, 2010). The strong subsidence in the northern and southern Barents Sea led to the development of depocentres during the Early to Middle Triassic (Riis et al, 2008)

The Barents Sea drifted northwards from 20°N of paleolatitude in the Carboniferous, to 55°N in the Triassic, to 75°N its actual position (Doré, 1995). This shift in latitude resulted in a change in climatic conditions. The widespread carbonate deposition in the Devonian to Permian times was gradually replaced by clastic deposition under temperate to arid conditions in the Triassic (Doré, 1995).

The thick Triassic stratum in the Barents Sea consists of fine-grained lithologies controlled by fluctuation of sea level (Johansen et al, 1992; Faleide et al 1984). The Early Triassic is marked by a marginal marine and deltaic sedimentation (Faleide et al, 1984; Johansen et al, 1992).

During the Early to Middle Triassic, prograding transgressive-regressive sequences dominated the Barents Sea resulting in punctuating coastal progradations (Glørstad et al, 2011; Worsley, 2008).

Past studies have shown that the sediments were likely derived from the erosion of the Baltic shield in the south and the Uralian mountains in the East and Southeast (Glørstad et al, 2010, 2011; Worsley, 2008; Johansen et al, 1992). All these systems were formed in a large relatively shallow epicontinental basin, several hundred kilometers wide in the Early Triassic (Glørstad et al, 2011; Glørstad et al, 2010). Epicontinental basins are well known to show great relocation of the shoreline even with moderate variations in sea level, influencing the deposition and accommodation space. In the Southwestern part of the Barents Sea, the newly created basin was gradually filled in by basinward stepping wedges from south and south-east. Due to sediment progradation the wide and deep basin gradually became shallower through time, despite many transgressional episodes (Worsley, 2008).

The seismic facies interpretation from Høy and Lunschien (2011) demonstrates that the Triassic sediment infill was caused by a huge prograding delta system from south-east to

north-west. This statement is confirmed by Glørstad et al (2011) with their observations of defined stacked clastic wedges that had prograded toward the west and northwest.

The Late- Mid to Late Triassic is marked by the deposition of organic rich shales from deltaic and floodplain environments prograding to the west which spread over large areas (Worsley, 2008, Johansen et al, 1992). The end of the Triassic succession consists of shallow marine deposits (Johansen et al, 1992). This shallowing is observed with interbedded high and low energy sedimentation. Continental deposits are frequently observed onshore in the uppermost Triassic (Faleide et al, 1984).

2.2.2 The Kapp Toscana Group and Snadd formation:

The Kapp Toscana group includes formations from the Middle Triassic (Ladinian) to the Middle Cretaceous (Fig.2). The Lower units consist mainly of silty lithologies whereas the upper units are more composed of fine to medium grained sandstones with coal debris. This coarsening upwards succession and the coal debris had been interpreted as being part of prograding delta systems across the whole Barents shelf. The progradation observed in the Kapp Toscana group seems to continue the northwesterly trend initiated during the Early Triassic of the Sassendalen Group. However, the paleocoast had a most proximal position than previously (Worsley, 2008).

2.2.3 Depositional environments of the Snadd formation:

The Snadd Formation consists of the Late Triassic deposits (Fig.2). It shows a coarsening upwards trend, mostly composed of prodeltaic shales to marginal marine sandstones. The Snadd deposits settled on the top and in front of the northwesterly prograding shelf system (Worsley, 2008). The Snadd Formation includes three time periods: Ladinian, Carnian and Early-Norian described separately below:

Ladinian:

The very rapid and radical transgression initiated in the Late Anisian, pushed back the coastline far east. As a result of this shift, the Ladinian period is dominated by fine-grained sedimentation corresponding to open marine deposits (Skjold et al, 1998). Based on gamma ray values, the rest of the period is characterized by upwards cleaning and shallowing, identified as a regressive pattern, with building shelf edge clinofolds (100 to 500m height) as a continuation of the underlying Anisian ones. These observations lead to the conclusion

that the Snadd Formation developed on a sedimentary shelf (Klausen et al, 2015). Basinward of those clinoforms the settings shift to offshore marine organic rich mudstone in the most distal parts (Klausen et al, 2015). This rapid progradation of the shoreline occurred on the inherited shelf of the western epicontinental seaway with water depth from 100 to 500m. (Klausen et al, 2015)

Carnian:

The low delta plain established at the end of the Ladinian facilitated the shift landwards of the shoreline; the shallow platform created was rapidly reoccupied by a delta (Fig.3). The absence of deep fluvial incision indicates a progradation without a fall in sea level meaning that the sediment supply increased. It marks the maximum regressive stage of the Early Carnian (Fig.3) (Klausen et al, 2015). The second part of the Carnian is not evenly distributed in the Barents Sea and is most pronounced in the west. It consists of shoreface sandstone deposits placed just above the flooding surface marking the end of the Early Carnian (Klausen et al, 2015). During the Middle Carnian another regressive stage occurred in the Snadd Formation (Fig.3) (Klausen et al, 2015). At the end of the Carnian a rise in sea level occurred (Klausen et al, 2015) associated with a shift in basin configuration and active subsidence concentrated at the East of the Loppa High. This subsidence triggered a north-east thickening of the Carnian Strata. This tectonic change triggered a change in drainage pattern towards a NE-SW direction (Skjold et al, 1998). The highstand system tract is marked by the development of paralic successions with abundant coals and microfossils reflecting swamp type vegetation (Skjold et al, 1998).

Early Norian:

The transition between the Carnian and Norian witnesses a deep change in depositional environments reflected by the mineralogical maturity of the sandstones observed on Svalbard and in the Barents Sea (Skjold et al, 1998). Palynological studies on those sandstones suggest a change in climatic conditions from semi-arid to temperate and humid, reflected in a higher degree of weathering (Skjold et al, 1998). The uppermost part of the Snadd Formation consists of a thin transgressive sequence interpreted as marine and marginal marine (Klausen et al, 2015). By this time the epicontinental basin had been almost completely filled in by the prograding clastic wedge and the transgression occurred over low gradient delta topography (Klausen et al, 2015).

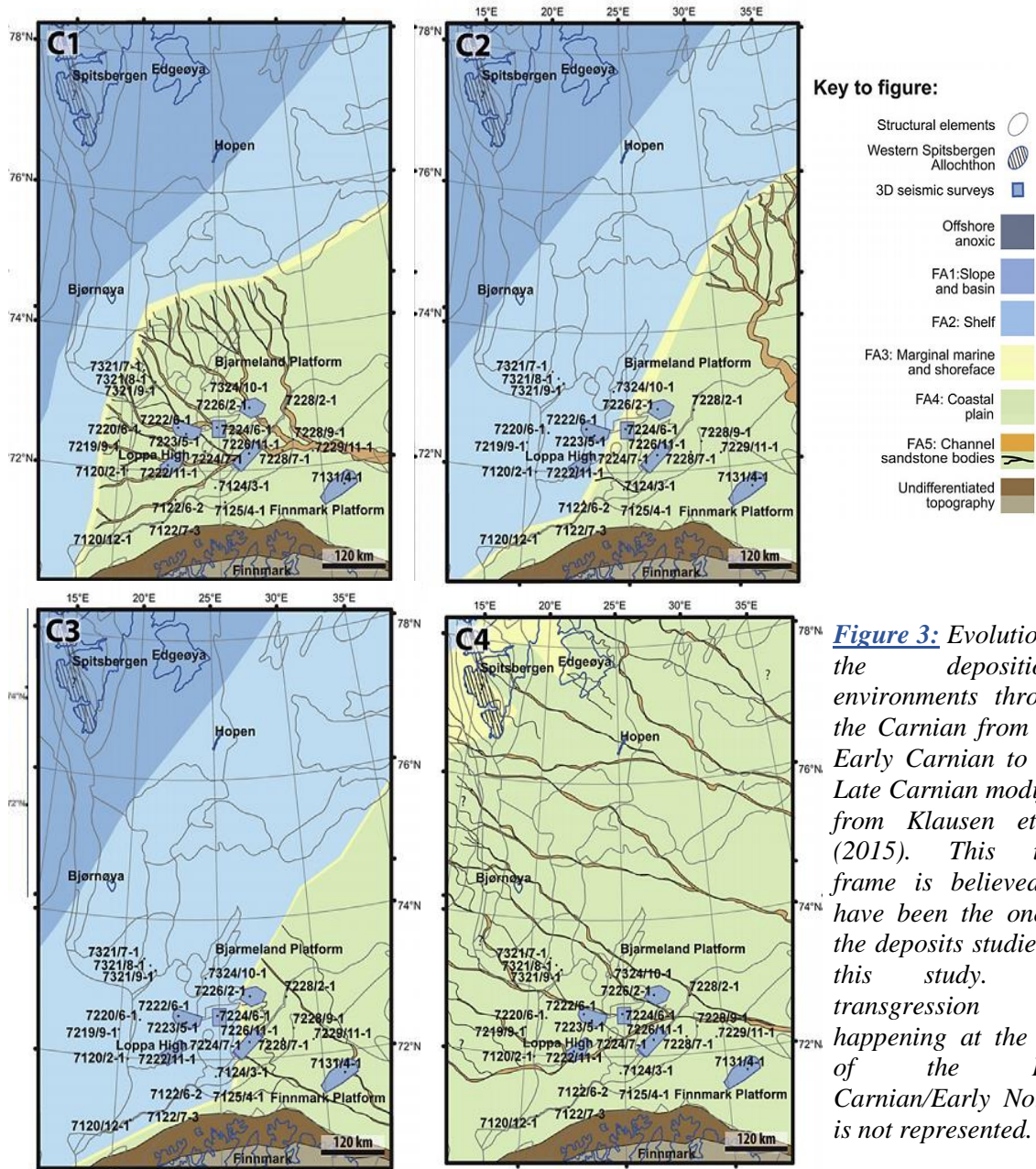


Figure 3: Evolution of the depositional environments through the Carnian from C1: Early Carnian to C4: Late Carnian modified from Klausen et al (2015). This time frame is believed to have been the one of the deposits studied in this study. The transgression happening at the end of the Late Carnian/Early Norian is not represented.

2.3 Post-Triassic times

The post Triassic eras are marked by more intense tectonic activity. Indeed, the degradation of the Pangean supercontinent initiated during the Middle Triassic–Early Cretaceous triggered tensional forces affecting the south and southwestern part of the Barents Sea. Rifting occurring during the Middle Jurassic to Early Cretaceous contributed to the uplift and erosion of part of the Triassic strata creating some gaps in the succession (Glørstad et al, 2011). This rifting event has increased the geothermal gradient in the area. During the rift phase, large deep-seated normal faults formed along the zones of weakness in the Caledonian basement. Most the tectonic movement ended in the Middle Cretaceous and

rapid subsidence affected the western part of the Barents Sea forming the main structural elements present today. At this time, the Loppa high was inverted between the subsiding Bjørnøya and Hammerfest Basins (Faleide et al, 1984).

During the Cenozoic, another transgression took place within the Paleocene (Worsley, 2008). This transgression created a marine shelf environment where fine clastics and carbonates were deposited (Worsley, 2008; Glørstad-Clark et al, 2010). During the Neogene, high amplitude repetitive subsidence-uplift and erosion occurred (Worsley, 2008; Glørstad-Clark et al, 2010). Reconstruction of the possible uplift that occurred during the Cenozoic made by Baig et al (2016) suggests an uplift in the order of 1400m in the Hammerfest Basin are which is corresponding to the location of the well 7122/6-2. The uplift in the Bjarmeland platform at the corresponding location of the well 7226/2-1 is estimated to 1250m in average, but is approximated between 1250 and 2400m to the north of the platform (Fig. 4).

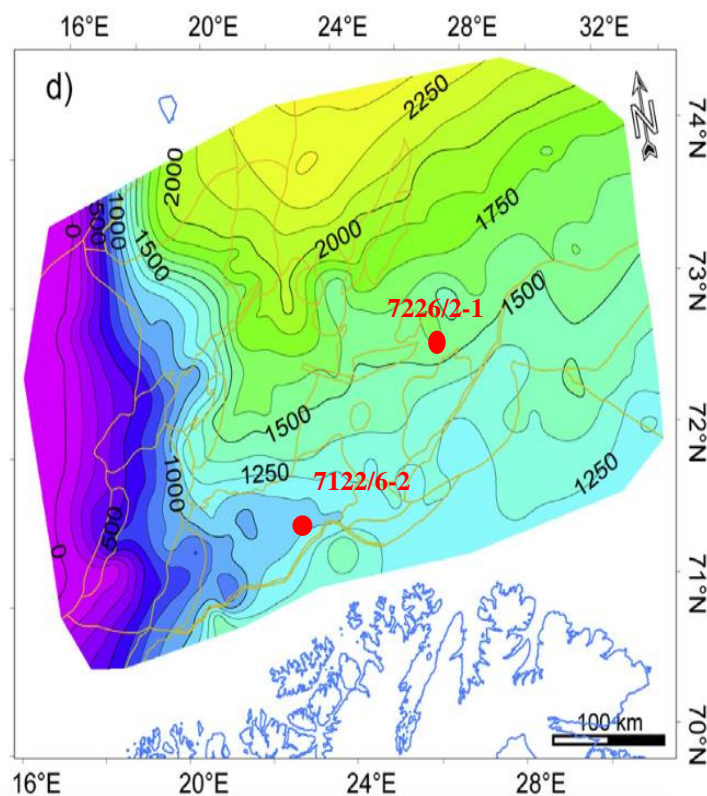


Figure 4: Cenozoic uplift reconstruction based on the combination of the datasets from sonic logs, shot gathers and vitrinite reflectance from Baig et al (2016). The positions of the studied wells are shown by the red dots.

2.4 Structural elements concerned in this study

The Bjarmeland Platform:

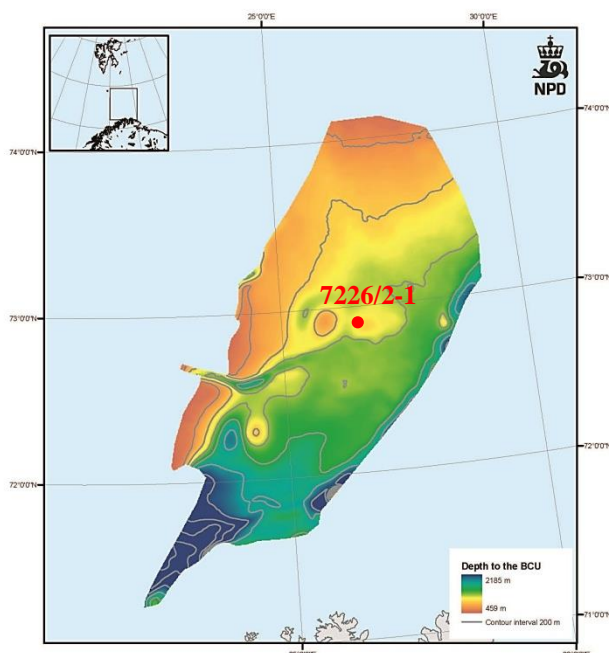


Figure 5: Contour map of the Bjarmeland platform modified from the Norwegian Petroleum directorate website (npd.no). The position of the well 7226/2-1 is illustrated by the red dot.

The Bjarmeland Platform is a stable area between the Hammerfest Basin to the south and the Nordkapp Basin to the south-east. It is bordered to the north by the Sentralbanken and Gardarbanken Highs and to the west by the Fingerdjupet Sub-basin and the Loppa High (Fig.1). The platform includes several highs such as the Norvag dome near where the well 7226/2-1 was drilled (Fig.5). As result of the tertiary uplift, the platform is gently dipping southwards but since the Late Palaeozoic the platform is considered as stable (Gabrielsen et al, 1990). The platform started to develop as a stable platform in the Late Carboniferous.

During the Late Permian-Early Jurassic the platform is assumed to have been terminated to the west by a fault zone orientated north-south. In the Late Permian–Early Triassic a pronounced structural high existed parallel with and to the east of the fault zone (Gabrielsen et al, 1990). During the Triassic era, this structural high developed a condensed Lower to Middle Triassic sequence and was transformed to a basin with its maximum thickness for the Upper Triassic deposits corresponding to the Snadd Formation in this study. The Late Mesozoic and Tertiary tectonism resulted in the present Loppa High and Fingerdjupet Sub-basin which now represent the western end of the platform. Within the platform, the structural patterns are due to salt tectonics and weak extension (Gabrielsen et al, 1990).

The Hammerfest Basin:

The Hammerfest Basin is a shallow east/northeast-west/southwest striking axis separated from the Finnmark Platform to the south, by the Troms-Finnmark platform, and from the Loppa high to the north by the Asterias Fault Complex (Fig 1). The basin is believed to have been generated from a failed rift in a triple junction (Talleraas, 1979) and has been estimated to have a depth of 6-7km (Gabrielsen et al, 1990). The basin is subdivided into a western and eastern sub-basin separated by the

extension of the Trollfjord Komaglev fault trend (Gabrielsen et al, 1989). The western part is dipping westwards towards the Tromsø Basin (Fig.6). This sub-basin is characterised by a gentle central dome parallel to the basin axis and an internal fault system (Gabrielsen et al, 1990). The Hammerfest Basin has both deep high-angle faults along the basin margins and listric normal fault detached above the Permian sequence and located more centrally in the basin while the east is less affected by the faulting (Berglund et al, 1986). The structures of the basin are the result of predominantly extensional forces, even if

it has been suggested that the deformation style could result from the reactivation by strike-slip in the Late Jurassic to Early Cretaceous (Gabrielsen et al, 1989). The basin is believed to be derived from previous basins orientated NE-SW created in the Late Devonian–Early Carboniferous. The separation of the Hammerfest Basin with the Finnmark Platform is estimated to have taken place in the Late Carboniferous (Gabrielsen et al, 1990). During the Triassic and Early Jurassic times, when the Snadd Formation was deposited, the Tromsø and Hammerfest basins were part of an epeirogenic deposition regime. The Hammerfest basin is believed to have become a separate depocentre in the Scythian (Early Triassic) (Berglund et al, 1986). The major subsidence period is the Early Cretaceous associated with pronounced activity along the major fault zones around the basin (Gabrielsen et al, 1990).

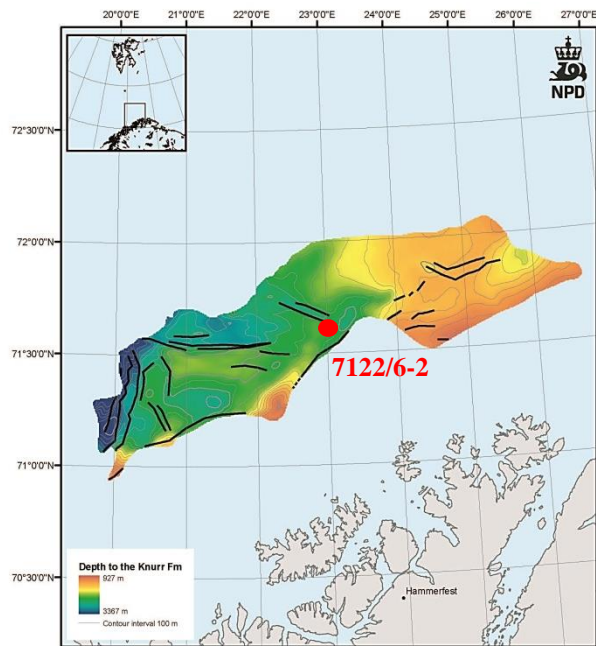


Figure 6: Contour map of the Hammerfest Basin modified from the Norwegian Petroleum directorate website (npd.no). The position of the well 7122/6-2 is illustrated by the red dot.

III. Theoretical background

3.1 Reservoir quality and diagenesis

The quality of a reservoir is defined by its capacity for hydrocarbon storage and deliverability. The possible storage is represented by the porosity of the sandstones assembly (Fig.7), the pore space available, but also by the size of the reservoir. The deliverability is represented by the permeability of the sandstones assembly and how easily fluids can flow through the system (Fig.7).

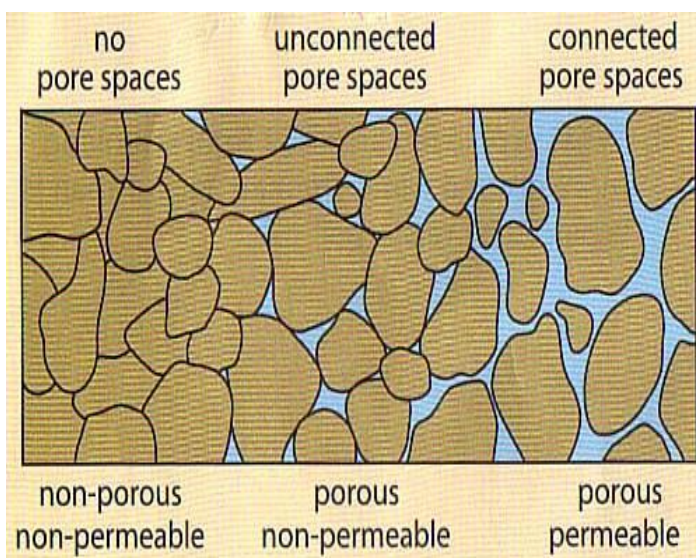


Figure 7: Representation of increasing porosity: more pore spaces, and increasing permeability: more connection between pore spaces. From <https://www.asu.edu/courses/gph111>.

Diagenesis is a term used to define all changes taking place from sediment deposition to the onset of metamorphism, converting loose sediments into sedimentary rocks (Ali et al; 2010). Diagenetic processes can enhance, modify or destroy the porosity and permeability.

Different factors influence the diagenetic processes; they are classified as sedimentary or environmental. The sedimentary

factors include particle size, fluid content, organic content and mineralogical composition, whereas environmental factors are temperature, pressure, and chemical conditions (Ali et al, 2010). Particles in a layer are subjected to different processes that directly impact the porosity and permeability of the layer such as compaction, cementation, recrystallization, replacement, differential solution and authigenesis.

Diagenetic processes can be divided into different groups. The most popular way to sort them, and the one used in this thesis, is near-surface, shallow, intermediate and deep burial diagenetic settings.

3.2 Diagenesis in sandstones and mudstones :

The quality of a reservoir depends on the porosity and permeability evolution. Those parameters are further dependent on five main parameters:

- The source area and source to sink distance will control the grain size, sorting and mineralogy. All together they control the framework of the deposits and its compressibility under an overburden. The composition and texture of the sedimentary assemblage is related to the source rocks, weathering and erosion in the source area associated with the transport processes and depositional environment (Bjørlykke, 1998).
- Climatic conditions will play an important role in controlling the intensity of weathering in the source area but also in the river discharge and depositional patterns.
- The depositional environment will govern the matrix of the assemblage. The type of material entering the pore space will then define the diagenetic evolution of the assemblage.
- The mechanical compaction from the overburden will reduce greatly the porosity. The degree of compaction depends on the sorting and mineralogy of the assemblage.
- The formation of authigenic minerals will greatly influence the porosity and permeability. Therefore, it is necessary to understand their formation and the chemical framework in which they form. Information about the local climate and geothermal gradient, burial (subsidence rate) and uplift history are tools used to define the physical conditions for chemical reactions in the basin.

It has been proven that the mechanical compaction and quartz cementation are the reasons behind great porosity loss in sandstone reservoirs (Bjørlykke et al, 1989). Nevertheless, other chemical processes occurring during burial will influence the porosity and permeability and decide the future quality of the reservoir. Those reactions occur at different burial conditions zones (temperature and pressure).

3.2.1 Early diagenesis processes :

In the earliest stage of diagenesis, the processes are significantly affected by their proximity to the surface and influenced by meteoric and sea water (Bjørlykke, 1998). The chemistry of the original pore water dominates these reactions. On land, the sediments are exposed to air and freshwater. In continental environments, the weathering reactions mostly involve oxygen

and are partly due to dissolution of minerals in freshwater (Bjørlykke & Jahren, 2010). In the sea, the water above the seabed is normally oxidizing. With burial, the oxygen is quickly consumed by the decay of organic matter, usually via bacterial activity, and the conditions become rapidly reducing (Bjørlykke & Jahren, 2010). Oxygen is also consumed in the sediment by the oxidation of iron and manganese in minerals; this is rare in marine settings but commonly occurs in continental deposits (Bjørlykke & Jahren, 2010). Iron is also precipitated below the redox boundary as iron sulphides or iron carbonate (siderite). With increasing depth, no more free oxygen can be found in the pore water and sulphate can be used by sulphate-reducing bacteria usually producing sulphides such as pyrite (Bjørlykke & Jahren, 2010).

Early marine diagenesis is also highly influenced by the accumulation of biogenic carbonate and silica on the sea floor (Bjørlykke, 1998). Biogenic activity plays an important role in the evolution of the textural composition of the deposits. Indeed, bioturbation destroys the primary structures such as clay laminae and may significantly reduce the permeability and thereby the reservoir quality.

Burrowing worms will produce fecal matter that may develop in smectite-rich clays leading to a decrease in the reservoir potential if recrystallized to illite but increase it if turned to chlorite coating. Finally, the dissolution of carbonate organism leads to the precipitation of carbonate cement, and is the principal cause of calcite cement in both sandstones and mudstones. The carbonate cementation will destroy the porosity of the cemented intervals but will also create a barrier to fluid flow, this way avoids further dissolution occurring.

The transport of dissolved solids by diffusion and fluid flow (advection) is most efficient near the surface and the potential for sediments to change their composition is therefore much higher at shallow depth than during greater burial (Bjørlykke & Jahren, 2010).

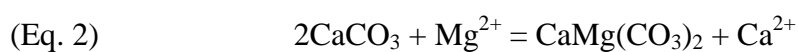
The flux of meteoric water is the main parameter controlling the intensity of the shallow burial diagenesis. This flux is at its highest in the marginal and shallow marine environments but also depends on external parameters such as climate, topography and water table (Fig.8) (Bjørlykke, 1998). The flow of meteoric water has a crucial importance in subsurface weathering. The dissolution of feldspars and mica and the precipitation of kaolinite (Eq.1) require the supply of protons H^+ and the removal of cations Na^+ and K^+ and silica is made by the fluid flow.

Carbonate cementation:

Carbonate cements may have different origins in continental and marine settings but are commonly derived from pre-deposited biogenic carbonate. In continental environments with net evaporation, carbonate cement may also form as vadose (pedogenic) or phreatic (groundwater) minerals (Maast, 2013). From modern observations, they typically form where the annual precipitation is less than 650 mm/year and the average temperature is above 5°C average. Pedogenic carbonates are linked to soil formation and are not commonly found in sandstone reservoirs. Phreatic carbonates are more common and form due to the concentration of ions in the pore water due to weathering reactions and net evaporation (Maast, 2013). This reaction mostly occurs in lowland regions where the river and groundwater have an increased salinity. These “salty” waters when exposed to semi-arid to arid regions with annual net evaporation may start precipitating phreatic cements. Carbonate cements in marine environment are usually derived from early marine cement or from biogenic carbonate minerals composed of high Mg calcite (Bjørlykke et al, 1989). During shallow burial, these minerals will transform to low Mg calcite.

Dolomitization :

Dolomitization is believed to be a diagenetic process (Hanken et al., 2010). The hydrated Mg^{2+} contained in the sea water as $Mg(H_2O)_6^{2+}$ cannot easily enter a crystal position at surface temperature, but with increasing temperature the hydration decreases (Hanken et al., 2010). Dolomite is generally not formed directly, but is the result of reactions between different forms of $CaCO_3$ and Mg^{2+} (Eq.2).



This reaction is dependent on the ratio Mg^{2+}/Ca^{2+} . The formation of dolomite will only take place if the supply of Mg maintains a high ratio (Hanken et al., 2010). The Mg is more likely to come from sea water even if other potential sources are possible, such as transformation of clay minerals.

Sulphate is also an important factor in the formation of dolomite. Experiments show that in the absence of sulphate dolomite forms rapidly, this would explain why dolomite is not common in modern marine environment as sulphate ions will prevent its formation (Baker

and Kastner, 1981). Consequently, dolomitization takes place where there are few sulphate ions, as in lakes and in brackish zones (Hanken et al., 2010).

Dolomitization requires three conditions to occur (Hanken et al., 2010):

- 1) Unstable calcium carbonate and supersaturation of the solution with respect to dolomite.
- 2) Addition of Mg^{2+} into the solution.
- 3) Absence or low concentration of formation inhibitor such as sulphate.

The dolomitization process is accelerated if the sediment has high permeability and high rate of percolation of magnesium rich pore water. Dolomite beds are often found as thin beds divided by shales due to the supply in Mg^{2+} from clay minerals (Hanken et al., 2010).

Mechanical compaction:

The degree of compaction is a function of different parameters such as sorting, grain size, but mainly the grain packing arrangement. Compaction in sandstones occurs in four processes: Grain rearrangement, plastic deformation of ductile components, dissolution and brittle fracturing (Bjørlykke & Jahren, 2010; Worden & Burley, 2003). Experimental compaction on loose sand show that the initial porosity of clean, well sorted sandstones ranges between 40-42% depending on the grain size and strength. After 2-3 km of burial corresponding to 20-30 MPa the porosity will be reduced to 35-25% (Bjørlykke & Jahren, 2010). Experiments on compaction of sand carried out by Chuhan et al. (2002, 2003) and Koochak Zadeh et al (2016) show that well sorted coarse-grained is more compressible than fine-grained sand (Fig.9).

The composition and texture of the sandstone govern the rate of mechanical compaction. Poorly sorted sands will compact more rapidly than well sorted sands and coarse grained sands will compact more rapidly than fine grained sands (Fig.9). On the same scheme, mineralogically immature sands will compact more rapidly than mature sands (Chuhan et al, 2002).

After 2km of burial (80-100°C), chemical compaction will start, with the quartz cementation stabilizing the grain framework and preventing further mechanical compaction.

The degree of porosity loss by mechanical compaction is known as the Intergranular Volume (IGV) which is the sum of the porosity, the cement and matrix observed today. In sandstones, the IGV is usually comprised between 28 and 38% and will stabilize at 26% for clean, well sorted, quartz rich sandstones due to cubic close packing of spheres (Maast, 2013). For sandstones containing significant amount of matrix the porosity will be lower but the IGV will also stabilize around 26%.

The degree of compaction differs greatly with the composition of the deposited material. Mica and lithic fragments rich assemblages containing more ductile grains are more compressible and will lose porosity more rapidly with depth.

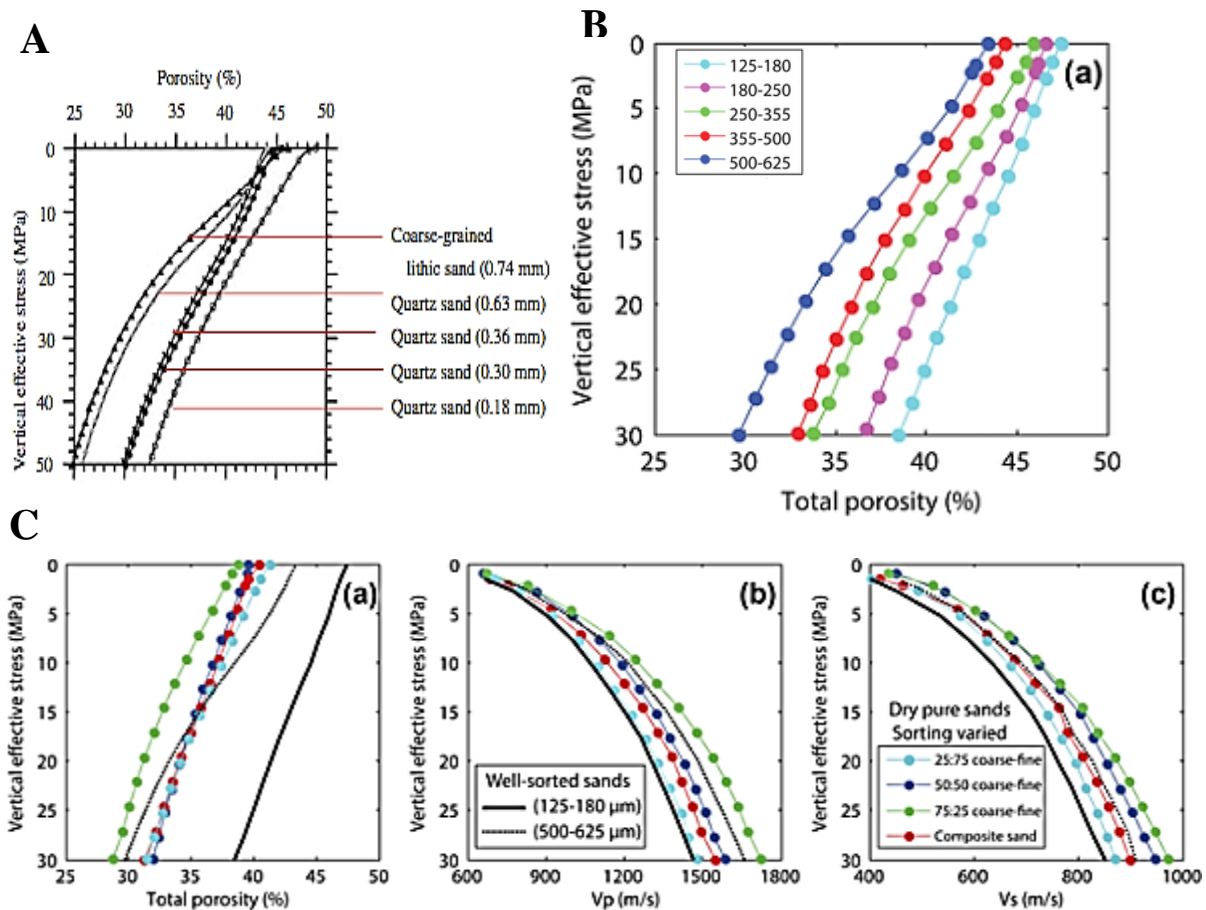


Figure 9: A) Porosity loss as a function of the grain sizes due to more grain crushing from Chuhan et al. (2003) in Bjørlykke & Jahren (2010). B) Different compaction trends in dry sand due to different grain sizes from Koochak Zadeh et al (2016). The difference in grain sizes leads to variable initial porosity as well as burial porosity. C) Different compaction trends and associated porosity loss in dry sand due to different sorting from Koochak Zadeh et al (2016).

3.2.2 Intermediate burial diagenesis: 2 - 3.5 km (50-120°C)

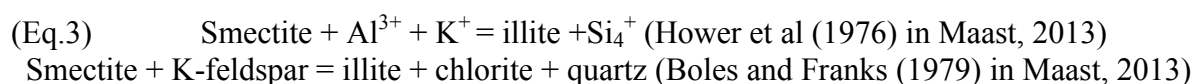
With increasing burial, clay minerals reduce their shear strength, increase the surface area of the sediments and change chemical properties such as ion exchange capacity (Bjørlykke, 1998). Diagenetic reactions are driven towards higher thermodynamic stability; the main principles for clay mineral diagenesis are therefore the same for every basin even if they have different mineral composition and thermal history (Bjørlykke, 1998).

Intermediate burial diagenesis, is defined as the stage during which buried sediments are no longer dominated by processes directly related to the surface. Cementation is the main process affecting the porosity, whereas dissolution is minor.

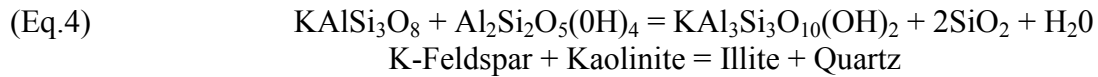
With increasing burial depth and temperature (>70°C) quartz cementation will start. The rate of precipitation increases exponentially with temperature higher than 80-100°C. Only 2-4% of quartz cement is sufficient to shut down further mechanical compaction and the system will enter the chemical compaction regime.

Most diagenetic reactions are temperature dependent. Many of them are dehydration reactions releasing volatile components of minerals. The increase in the effective stress during burial is believed to favor the precipitation of dense minerals. Minerals may dissolve, precipitate, or be replaced.

70°C is the starting point of many chemical reactions in clay minerals. Smectite present in some muddy, particularly volcanic sandstones will start to dissolve at 70-80°C and be replaced by mixed-layer minerals and illite (Eq.3) leading to bad reservoir quality.



Illite is also formed at the expense of kaolinite (Eq.4). Quartz cementation removes silica from the system and allows the transformation of kaolinite and K-feldspar into illite. This reaction starts when the burial temperature reaches 130°C where K-feldspar and kaolinite are no longer thermodynamically stable together. In sandstones poor in K-feldspar, kaolinite will be stable at greater depth and the illitisation will be retarded. The provenance of the sandstones will define its composition; associated with the early diagenesis model it can be a tool to predict the distribution of kaolinite and precipitation of illite in basins.



Grain-coating is deposited from mud rich waters in the near surface diagenesis. With depth, the precursor clays are no longer stable. Chlorite forms primarily by the transformation of Fe-rich clays at depths greater than 3km and temperatures greater than 90-100°C. The chlorite coating has been proven to be the origin of enhanced porosity in deeply buried reservoirs. This is explained by the restricted surface area available for quartz cementation which is therefore inhibited. Quartz overgrowth will appear in any disruption in the chlorite coating (Fig.10).

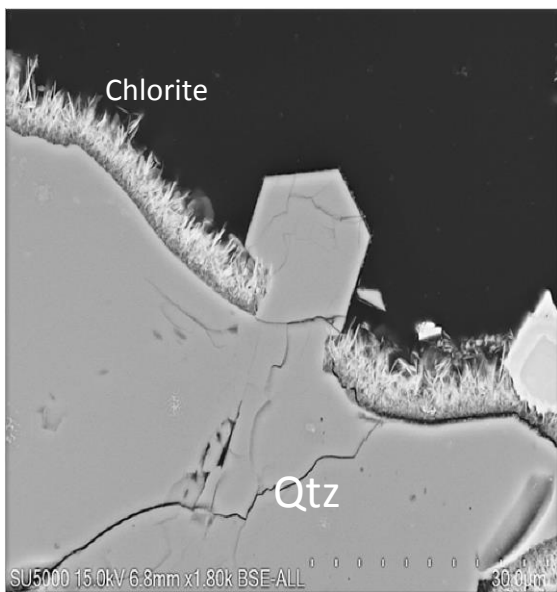


Figure 10: Break in chlorite coating allowing quartz cementation to start, SEM image. UIO

At about 3km, before the deep burial diagenesis, albite will become more stable than K-feldspar because Na^+ is normally the dominant cation in the pore water while the potassium will be reduced by the clay mineral reactions such as illitization. The albitization of plagioclases such as anorthite and release excess Al^{3+} and Ca^{2+} which can influence later cementation (Bjørlykke & Jahren, 2010; Morad et al, 2000).

Kaolinite also undergoes severe dissolution at depths between 3.0 and 3.5km (100-130°C) and recrystallizes into blocky crystals of dickite. Both mineral phases have the same chemical composition but dickite occurs as slightly thicker crystals. At depth of 3-4000 m (100-120°C) kaolinite will dissolve and reprecipitate directly as dickite (Bjørlykke & Jahren, 2010; Worden & Morad, 2003, Morad et al, 2000).

3.2.3 Deep diagenesis: > 3,5 - 4 Km (>120°C)

The deep diagenesis is mostly governed by the precipitation of quartz cement and diagenetic illite. The rate of quartz cementation increases exponentially with increasing temperature with an estimated factor at 1,7 for every 10°C increase (Bjørlykke & Jahren, 2010). The

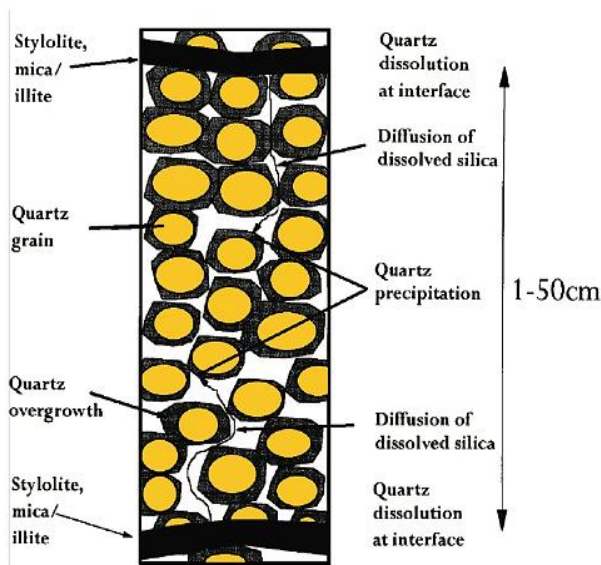


Figure 11: Schematic illustration of clay induced dissolution model for quartz cementation from Bjørkum et al (1998) in Maast (2013). Stylolites and pressure-dissolution are believed to be the main mechanism of release of silica transported by diffusion to grain surfaces from cementation. Grain coatings such as chlorite or microquartz prevent or retard the quartz cementation.

precipitation is a function of the surface area available for cementation. Therefore, as the cement is filling the pore space, fewer surfaces are available and the quartz growth decreases. The transport of silica is also one parameter controlling the quartz cementation. Silica is dissolved at grain contacts, along stylolites and clay laminae and transported by diffusion to the grain surfaces where the quartz overgrowth forms (Fig.11). The stylolites represent a barrier to fluid flow both during compaction and during production but may not be continuous laterally. Quartz cementation has then three main requirements: the pore water has to be supersaturated in respect with quartz, the temperature must be higher than 70°-

80°C and some surface area must be available. If some coatings are present on the grains surface such as chlorite, micro quartz or bitumen, the quartz cementation will be inhibited. Sandstones with grain coatings may remain uncemented down to 4-5km burial depth and will be subjected to high effective stress (40-50 MPa) causing pervasive grain crushing and new fresh surfaces for cementation (Chuhan et al, 2002).

3.2.4 Uplift related processes:

During this stage, long-buried rocks are affected by processes associated with uplift, erosion and exposure to the surface processes of meteoric water (low salinity, high CO₂ content) that is not related to the depositional environment (Worden & Burley, 2003). The upper limit is the erosional interface whereas the lower boundary is gradational and placed where erosional processes become insignificant. Dissolution by meteoric water is the major porosity forming process due to the alteration of minerals such as feldspars altered into kaolinite. This dissolution creates little porosity increase since the kaolinite will fill the pore space, if the

deposits are brought close to the surface. Even if some micro-porosity exists between the kaolinite crystals, the fluids are unable to penetrate such small pore spaces and the porosity will be considered as negligible in term of reservoir quality. The chemical compaction will continue during uplift as long as the temperature is higher than 70°C. The mechanical extension created by the loss of load by erosion will be partly compensated by the chemical compaction and quartz cement will fill open fractures.

Figure 12 summarizes the main components of the diagenesis through depths as well as during uplift.

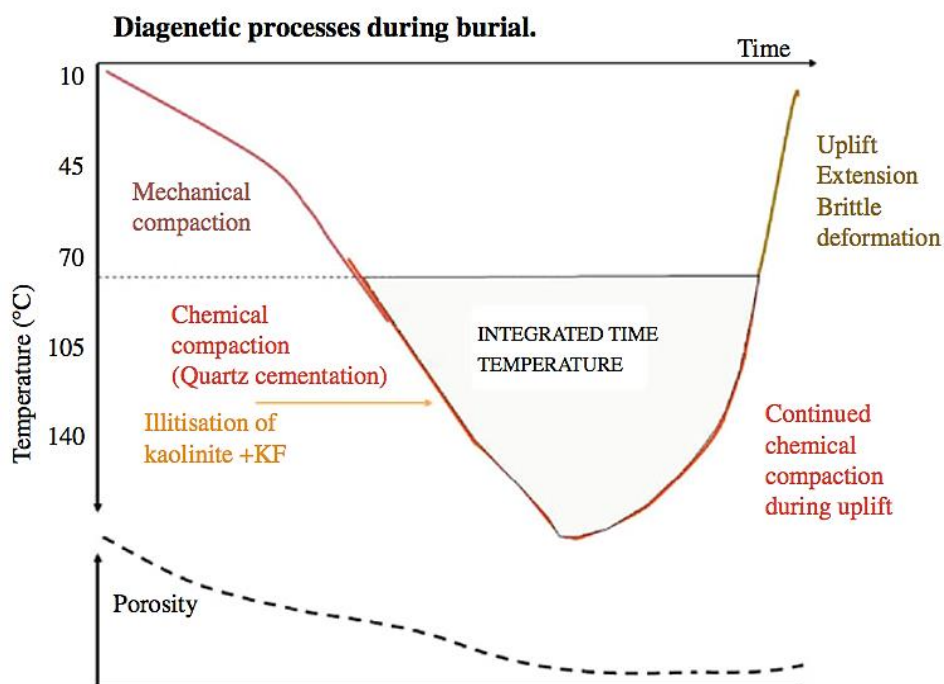


Figure 12: Main diagenetic processes as a function of time and temperature from Bjørlykke & Jahren (2010). The quartz cementation will also be active during uplift as long as the temperature exceeds 70-80°C.

3.3 Porosity preserving processes:

Clay coatings:

Pore lining clays also called grain coatings; reduce the area available for quartz cement nucleation, slowing down the cementation rate. This can explain abnormal high porosity at great burial depths. Most of the time the clay coating is composed of chlorite (Fig.10) derived from a precursor deposited simultaneously with the grains or by infiltration and turned into chlorite with increasing temperatures and pressure during burial (Bjørlykke &

Jahren, 2010; Wilson and Pittman, 1977). Fe-rich chlorites are most commonly found in marine environments whereas Mg-rich chlorites are mostly found in semi-arid continental deposits characterized by net evaporation (Bjørlykke & Jahren, 2010; Wilson and Pittman, 1977).

Microquartz coating:

Microquartz forms from highly supersaturated pore waters as opal A when opal CT dissolves. The transformation to quartz is sequenced into repetitive dissolution-precipitation process of opal A to opal CT to quartz. The transformation of silica happens at relatively shallow burial at temperatures ranging from 35 to 70°C. The precursor of microquartz coating is believed to be a sponge Rhaxella, putting some sedimentological and potential facies related constraints on their distribution (Maast, 2013).

Early hydrocarbon emplacement:

The presence of hydrocarbon pore fluids inhibiting quartz cementation depends on the wettability of the reservoir. Carbonate reservoirs are preferentially oil-wet and may therefore successfully inhibit quartz cement. On the other hand, sandstone reservoirs are most commonly water-wet and residual water will cover the grain surface instead of the oil, allowing the quartz cementation to be initiated by diffusion (Maast, 2013).

Overpressure at shallow depth:

The rapid burial associated with fluid-filled sediments and covered by an effective seal will create an overpressure zone. An overpressure zone at shallow depth will preserve the porosity by acting against the mechanical compaction. The fluid pressure of the fluids contained in the pore space will balance the effective stress from the overburden and this way preserve the intergranular porosity. An overpressure zone can be easily detected using the sonic log showing abnormally high velocities at shallow depths (Bjørlykke and Jahren, 2010). The fluid overpressure is not likely to maintain with depth and the conservation of porosity is then not guaranteed (Bloch et al, 2002). Moreover, if the fluid overpressure is developed at depth, porosity will not be preserved to significant extend since most of the mechanical compaction occurs before 2500m depth (Bloch et al, 2002).

IV. Methods

4.1 Sedimentological core logging:

The well 7122/6-2 located in the Hammerfest Basin was drilled in 2006, and reached 3070m depth in the Middle Triassic deposits (Kobbe Fm). The aim of this well was to prove gas occurrences in the sandstones layers of the Late Triassic Snadd Fm of Carnian age. The well is now being considered as resourceful (NPD) after finding gas in the top Carnian tight sandstones at 2387m depth. The drilled location had been chosen for its structural closure due to a dipping of rotated fault block enhancing its potential to find hydrocarbons.

The well 7226/2-1 is located on a dome structure in the Bjarmeland platform. The well was drilled in 2008, and reached 2991m depth and penetrated until the Early Triassic deposits (Kobbe Fm). The aim was to prove the occurrence of hydrocarbon in the Carnian age deposits of the Snadd Fm. Gas has been found only in the Early Triassic deposits of the Kobbe Fm.

The sedimentological logs of the cores 7122/6-2 and 7226/2-1 were made on the 10-11 of May 2016 at the Norwegian petroleum directorate, Stavanger, with the help of Lina Hedvig Line (UiO, PhD). The logs were executed on the B-cut of the cores. The cores were first observed and sprayed with water in view to identify the change in porosity and have a better perception of the sedimentological features. The cores were logged from the deepest section to the shallowest, following the geological evolution in time at the scale 1:50. The grain size was assessed using the Wenworth (1922) grain size classes. The samples used for mineralogical analyses were collected previously to the thesis.

The facies descriptions and associations were built using the correlated observations from core logs, pictures and thin section where observations were made about lithology, texture and structures. The term facies is used as the sum of the features related to the environmental conditions under which the given rock was deposited. A facies association is a group of facies genetically related reflecting a specific depositional environment.

4.2 Mineralogical and petrographical analyses:

The mineralogical and petrographical analyses were performed using different approaches:

Thin section observations, X-ray diffractometry analysis (XRD) and scanning electron microscope (SEM). The use of laboratory techniques and guidance for analyses were conducted under the supervision of PhD students Beyene Girma Haile and Lina Hedvig Line.

4.2.1 Thin section analysis :

The thin sections of the 36 samples were prepared at the University of Oslo by Salahalladin Akhavan of the pro-technical department. The rock samples were first impregnated by blue epoxy, to help visualizing the porosity and then glued onto a 2.5x4.5 cm glass slide. The samples were then polished until reaching 30 µm of thickness.

All the thin sections were observed using a *Nikon Optiphot-Pol* petrographic microscope, in order to extract information about the mineralogy and rock texture. The samples were studied both under plain polarized light (ppl) for the distinction of mineral characteristics, (eg. relief and pleochroism) and cross polarized light (xpl) to enhance zoning, twinning and degree of weathering of feldspars. The thin section observations focused on the mineralogy, lithology, laminations, micropaleontology, average grain size, average roundness, and average sphericity, grain contact and sorting. Pictures were taken using the integrated camera of a Samsung smartphone.

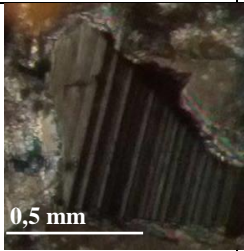
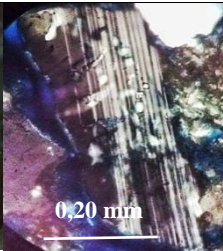
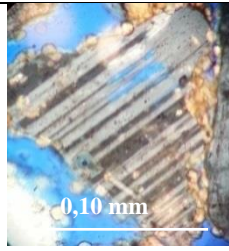
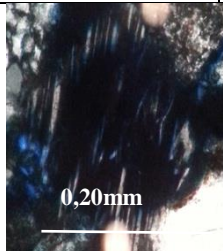
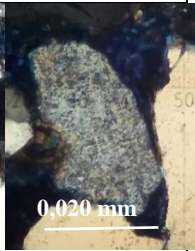
Several mineralogical features were investigated when looking at the thin sections, described as below:

- 1) A systematic description of the surface of the sample was made in term of color, texture, and possible mineralogy using “Atlas of sedimentary rocks under the microscope” by Adams et al (1984).
- 2) An estimation of the degree of roundness and sorting of detrital grains. The classification was based on Powers’ terminology (1953) while the degree of sorting was based on the classification scheme developed by Compton (1962) and correlated by the standard deviation of Folk (1974).
- 3) An estimation of the degree of weathering of feldspar grains. The degree of weathering ranges from degree 1, defining a slight alteration to degree 5, defining an almost complete dissolution of the grain (table 1). A distinction was made between K-feldspars and plagioclases. The degree of weathering gives information on the

intensity of weathering in the depositional environment and/or the intensity of the leaching from diagenetic processes.

- 4) A systematic research for quartz and feldspar overgrowth was carried out, as well as the identification of the nature of cement if any.

Table 1: Table classifying the degree of weathering from 1 to 5. The pictures are from both the samples of the Well 7122/6-2 and Well 7226/2-1

Degree	1	2	3	4	5
Image					
Description	No traces of weathering Twinning and characteristic shape well conserved	First evidence of weathering. Twinning are preserved.	Rough grain surface, evidences of dissolution. Twinning are blurry	Very rough grain surface, partially dissolved. Twinning are weak and not well spread	Totally altered or dissolved grains, almost not recognizable

Sources of error :

Thin section interpretation is based on the experience of the observer, especially when the samples are highly altered or composed of clay minerals that are difficult to identify under the microscope. The thickness of the thin-section, artificial fractures and porosity due to detaching grains during the thin section preparation must be treated with consideration mostly during the point counting.

4.2.2 Point counting :

Point counting has been carried out using a Swift (model F) counter installed on a petrographic microscope. The point counting was carried out on 32 samples of the 36 and due to their very fine grain size, four samples have been discarded. Four hundred points were counted per analysed sample. The distinction was made between 12 categories of mineral

phase found in appendix 4 (Tables 4- 11). The quartz grains were divided in monocrystalline and polycrystalline, whereas the feldspar grains were divided between K-Feldspar and plagioclase as well as their degree of alteration. The rest of the categories were divided between rock fragments, pore-filling clays, cement, nature of the matrix and overgrowths. The porosity was also counted as one category. From the point counting, the quantified fractions of elements were plot in the sandstone classification diagram (Fig.13) for determining the type of sandstone observed. The fraction of quartz is particularly important as it defines the degree of transport, leaching and reworking.

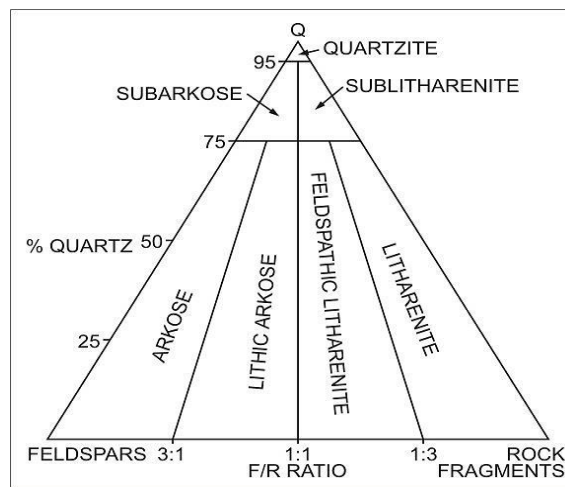


Figure 13: Sandstones classification representation from Folk (1974).

IGV calculation:

The intergranular volume (IGV) calculation was used to reconstruct the loss of porosity due to mechanical and chemical compaction. The IGV is measured by point counting and is the sum of intergranular pore space, intergranular cement and depositional matrix as expressed as below (Eq.5):

$$(Eq.5) \quad \mathbf{IGV} = \text{Volume porosity} + \text{Volume of cement} + \text{Volume of depositional matrix}$$

The volumes are expressed as percentage of the whole rock volume. The porosity refers only as the primary porosity as the secondary porosity used to be part of the framework grains. The cement volume represents all the diagenetically induced products occupying the pore space such as calcite or quartz cement but also authigenic clay minerals such as kaolinite, chlorite platelets or illite. The matrix is defined as depositional silt and clay size particles that fill the space between framework grains. The percentage of matrix is represented by the

allogenic clay minerals but the recrystallization of minerals such as mica into chlorite pseudomatrix may lead to overestimation of the matrix content. The IGV reflects the proximity of the framework grains and is a valuable tool to indicate both the mechanical and chemical compaction (pressure solution) in grain supported material (Paxton et al, 2002).

The percent of original porosity destroyed by mechanical compaction is estimated using the equation proposed by Houseknecht (1987), as expressed below (Eq.6):

$$(Eq.6) \quad \text{\% of mechanical compaction} = \frac{40 - IGV}{40} \times 100$$

This calculation lies on the fact that initial porosity of sandstones is averaging at 40% of porosity right after deposition. IGV will vary with a small degree with sorting, it is unaffected by grain size. The initial porosity will change according to the sorting.

The percentage of porosity lost by cementation is also defined by Houseknecht (1987) and is expressed as below (Eq.7):

$$(Eq.7) \quad \text{\% of chemical compaction} = \frac{\text{Cement}}{40} \times 100$$

Where the cement is the volume of the cement present expressed as a percentage of whole rock.

4.2.3 Bulk XRD:

Sample preparation :

The preparation for bulk XRD analysis was carried out on 36 samples. Each sample was first ground to rock powder by a swinging mill for 2, 5 min. The grain size is then reduced to less than 500 μm . The mill was carefully cleaned between each sample with soap and water, followed by ethanol to avoid any contamination and the same moment of torsion (40Nm) was used on every sample. The grain size was reduced once again the fraction size to <10 μm using a McCrone micronizer machine. For each sample 3g were taken and placed in the machine containers in addition of 9ml of ethanol and 48 pieces of agate. The container ran in the machine for 12 minutes. The samples were then left to dry overnight in an oven heated at 50-60°C.

The final step of the XRD-analysis preparation is to load the dried very fine grained powder into small XRD glass holders. The loading has been done carefully, to reduce as much as possible an orientation of the grains which could lead to a misreading of the composition by the XRD analyser. The data were collected on a Bruker D8 Advance, equipped With Lynxeye linear PSD detector, 2 kW Cu anode X-ray tube, operated at 40 kV and 40mA variable divergence slit, sample length 15mm Ni Kbeta filter 2.5 degrees soller slits (both primary and secondary), and sample rotation at 30 RPM.

XRD analysis :

XRD analysis was used in addition to the SEM to give information about the mineralogical composition of the samples when fractions are too small to be observed under microscopic analyses, as for example clay fraction, or also when the grains are too weathered to be identified. XRD analyses are based on the fact that the atoms in each mineral are arranged in different atomic planes forming a specific unit cell. The distance between its atomic planes in the lattice is characteristic to the mineral and is called d-spacing. When placed into the

Table 2: Table gathering the d-spacing values for the most common minerals found in sandstones.

Mineral	d-spacing value (Å)	Mineral	d-spacing value (Å)
Quartz	4.45	Siderite	2.79
Albite	3.18	Pyrite	2.71
Plagioclase	3.19	Kaolinite	7.0 / 3.58
K-Feldspar	3.24	Illite/Mica	10
Muscovite	10.01	Chlorite	7.0 / 3.54
Calcite	3.03	Dolomite	2.89

XRD analyser, the mineral gets bombarded with X-rays, the different atomic planes will reflect at different incident angles. Reflected and diffracted rays interfere to construct a characteristic signature, or spectrum of peaks for the mineral called diffractogram. A peak in the diffractogram means that the mineral is composed of atomic planes with a d-spacing allowing the reflection of X-rays for a particular 2θ angle. Characteristic d-spacing found in this study are listed on the table 2.

DiffraC Eva program :

DiffraC Eva software was used to evaluate and analyse X-Ray diffraction data. The program analyses the data and suggests possible peaks attributed to specific mineral phases in the diffractogram. The identification of the phases is made on the d-spacing values and the two-

theta values. The suggested minerals are extracted from the PDF (Powder Diffraction File) 2002 database edited by the International Center for Diffraction Data (ICDD). Once the user is satisfied by the fit between the suggestions on the diffractogram, the mineral is assigned to the peaks corresponding and the same is repeated until all the peaks had been assigned to a mineral. The results of the XRD data must be treated carefully because peaks of different minerals can have similar values and then be misinterpreted. The different phases listed in table 2 had been used to assign values to the diffractogram.

Quantitative analysis of Bulk XRD using Profex :

The identification of mineral phases and semi-quantitative analyses in *Diffrac Eva* were then used to quantify each phase using the software *Profex version 3.8.0*. Profex is graphical software using Rietveld refinement on powder X-ray diffraction data. The program reads and displays diffractogram patterns imported and will assign chosen mineral phases to the peaks in the diffractogram. The mineral phases are chosen based on previous identification and compared with databases from crystals structures and instrument configuration in view to quantify their abundance. The Profex program will then summarize the quantities for every phase (Doebelin & Kleeberg, 2015).

Source of errors :

One of the main potential sources of error is the artificial orientation given to the grain during the preparation. This can lead the beam to hit several times the same mineral and result to overestimation of the mineral abundance. Other potential sources of error are the misalignment of the instrument, size of the sample, and preferred orientation of the surfaces in the sample, such as cleavage. Another type of error can be related to the trust of the software to assign a correct peak-mineral correspondence based on the database used.

Moreover, the limit of detection of the XRD device is about 1-2% in multiphase geological mixtures. However, this limit might be lower in some cases, as the detection limit of a phase in a multi-mixture is dependent on the mixture itself. Example give, a small amount of quartz in a fairly pure calcite powder will have a much lower detection limit than, for example, a small amount of pyrite in a clay-rich and partly amorphous sample with 10+ phases. Longer counting time will also increase the intensity of the different phases, separating small peaks from the background noise.

4.2.4 Clay fraction analyses:

Nine samples were chosen per well for clay fraction analyses. The selection was made to represent the clay distribution through the core. Each of the chosen samples was crushed to grain size 1-2mm and mixed with 200ml of Na_2CO_3 solution at 0,125g/L of concentration. The mixed solution was stirred during 1min and placed into an ultrasonic bath for 10 min in view to accelerate the dispersion of the clay particles. The solution was then let to rest 24hours. After resting, the solution was stirred once again, and then filled with 400 added ml of Na_2CO_3 . After 6,5h of rest the first 8,5cm of the solution, containing the suspended material, were extracted and filtered using a suction pump and a filter. The filtrated material was then transferred to a silica glass slide. The samples were run 3 times in different environmental conditions. The first run was made in an air-dried condition. The second run was done in an Ethylene-Glycol (EG) vapour condition, used to identify swelling clay such as smectite. The third run consisted in a heat-treatment; the sample is heated at 350 and 550°C. At this temperature, the kaolinite becomes amorphous to the X-rays. The comparison between the heat-treatment response and the EG response will confirm the presence or absence of kaolinite.

4.2.5 Scanning Electron Microscope (SEM):

The SEM allows high-resolution study of the minerals and the pore space, especially in most cases the identification of pore filling minerals through chemical analysis. The SEM was used to identify the phases and minerals that could not be interpreted by the optical microscopy or on the doubtful assemblies found in XRD. The SEM was mostly used on the samples from the well 7122/6-2 due to their very fine-grained size, abundance of clay minerals and high degree of alteration of the minerals. The SEM analyses were carried using a *JEOL JSM-6460LV*, with a *LINK INCA Energy 300(EDS)* at the department of Geoscience at UIO, under the supervision of Berit Løken Berg and PhD student Orhan Mahmic. Before being put in the SEM the thin sections were coated with carbon, while the stubs were coated with gold, to remove charging from the sample. This process avoids the accumulation of electron on the sample and allows getting a better image resolution. Backscatter Electron Image (BEI) was used to analyse the thin sections while Secondary Electron Image (SEI) was used for the stubs. The Ultra Variable pressure Detector (UVD) was used to identify the overgrowth of quartz from the original grains as presented in Figure 14.

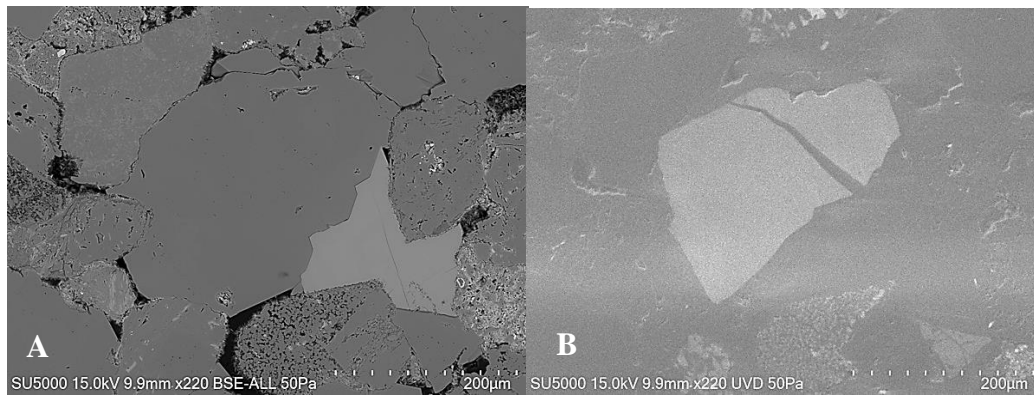


Figure 14: Identification of the quartz cement by comparison of the same image from different sensors. The **A** image is taken with the BEI whereas the image **B** is taken using the UVD detector allowing the identification of the original grain.

4.3 Textural analysis :

From the identification of the mineralogical assemblage of each sample using the optical microscopy, point counting, XRD and SEM. The amount of each mineral was collected in view to classify the sample following the scheme of classification of Sandstone from Folk (1974). The degree of transport of the grains was evaluated by looking at the grain shape, relative abundance of quartz and degree of grain leaching and weathering. The textural properties investigated in this study are average grain size, sorting, roundness, grain contact, grain preservation, porosity and intergranular volume.

4.3.1 Grain size, sorting and particle shape:

The grain size was measured using the optical microscope. The size is considered as the distance between the edges of the grain along the longest axis and carried out on an average of 100 representative grains per thin section. From the microscope, the value had to be converted in millimetres using the relationship: $\Phi = -\log_2 d$ Where Φ is the Phi size and d is the grain diameter in millimetres. The values were then compared with the Wenworth (1922) grain size classification scale of terrigenous sediments presented as the table 3.

The particle shapes presented in Figure 15, were qualitatively estimated using the degree of roundness and sphericity scale from Powers (1953). An investigation carried on 100 grains in each thin section gave the particle shape estimation. This estimation was then used to interpret the sediment transport and reworking. Higher roundness of the grain may indicate longer transport distance.

Table 3: *Wentworth size classes associated with their correspondences in mm, μm and rock type associated. From Wentworth (1922).*

Millimeters (mm)	Micrometers (μm)	Phi (ϕ)	Wentworth size class		Rock type
4096		-12.0	Boulder	Gravel	Conglomerate/ Breccia
256		-8.0	Cobble		
64		-6.0	Pebble		
4		-2.0	Granule		
2.00		-1.0			
			Very coarse sand	Sand	Sandstone
1.00		0.0	Coarse sand		
1/2	0.50	1.0	Medium sand		
1/4	0.25	2.0	Fine sand		
1/8	0.125	3.0	Very fine sand		
1/16	0.0625	4.0		Silt	Siltstone
			Coarse silt		
1/32	0.031	5.0	Medium silt		
1/64	0.0156	6.0	Fine silt		
1/128	0.0078	7.0	Very fine silt		
1/256	0.0039	8.0		Mud	Claystone
	0.00006	14.0	Clay		

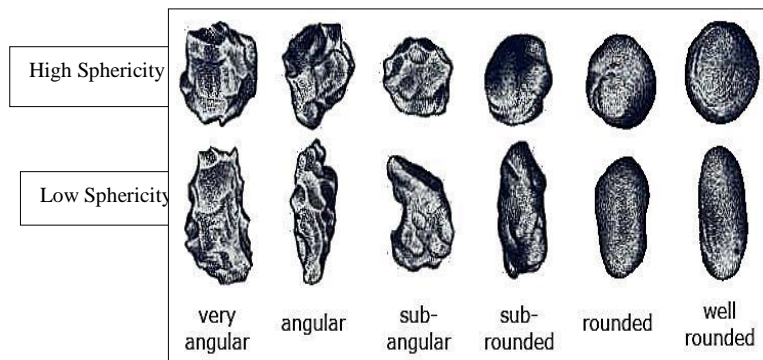
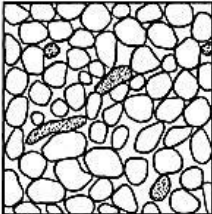
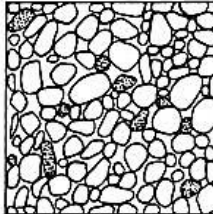
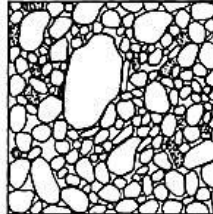
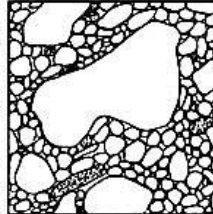
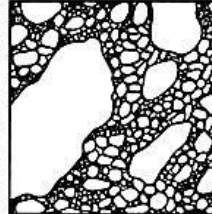


Figure 15: *Visual comparators of clast shape from Powers (1953)*

The sorting was calculated using the standard deviation values emitted by Folk et al (1957). The values were then compared with the visual estimation chart from Compton (1962). The overall gives the sorting of the thin section. The table 4 presents the data used for the comparison.

Table 4: Table gathering the sorting classes and standard deviation associated from Folk (1957, 1974). The last row of the table contains the visual comparators from Compton (1962).

Sorting class (Folk, 1974)	Standard deviation (Φ) (Folk et al, 1957): SD = $\frac{\Phi_{84} - \Phi_{16}}{4} + \frac{\Phi_{95} - \Phi_5}{6.6}$
Very well Sorted	< 0.35
Well sorted	0.35 - 0.50
Moderately well sorted	0.50 - 0.71
Moderately sorted	0.71 - 1.00
Poorly sorted	1.00 - 2.00
Very poorly sorted	2.00 - 4.00
Extremely poorly sorted	> 4.00

				
Very well sorted	Well sorted	Moderately sorted	Poorly sorted	Very poorly sorted

4.3.2 Grain contacts:

The grain contact type of 100 grains per thin section was investigated using optical microscopy associated with the visual comparator of Santin et al (2009) presented in Figure 16, in view to get a mean visual estimation of its degree of mechanical compaction in the sandstone samples. Undergoing the mechanical compaction, the grains rearrange their disposition and enter in contacts, through the different steps of the compaction; their contact is willing to change.

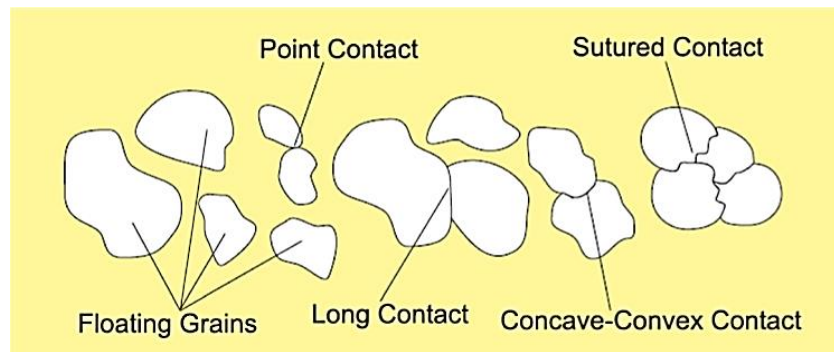


Figure 16 : Illustration from Santin et al. (2009) of the different types of grain contact.

4.3.3 Porosity estimation :

The porosity has been estimated using scanned pictures of the thin section at a resolution 1600 dpi entered in the program *Image J*. The program allows the user to calculate the percentage of color ranges. Due to the impregnation of blue Epoxy in the pore space, the porosity was estimated as being the percentage of blue range in each sample. This technique can lead to over or underestimation depending on the quality of the pictures. When the thin section contains a lot of detached grains from its preparation and when the epoxy is covering some of the grain surface, thick can lead to an overestimation. The porosity is also assessed by the point counting and neutron porosity log.

4.4 Petrophysical analyses :

Petrophysical analyses were carried out for both wells 7122/6-2 and 7226/2-1 based on the study of well logs. The evaluation of the compaction regime intervals and uplift estimation was the aim of the analyses. The well logs used in this study are sonic log, gamma log, bulk density log and neutron log.

4.4.1 Compaction trend :

Due to the increase in the overburden with depth, the physical properties of the rocks change and rearrange. With increasing depth and so on pressure and temperature the regime passes from the mechanical compaction regime (MC) to the chemical compaction regime (CC). The chemical compaction even at its very onset reduces the porosity and increases the stiffness of the assemblage. This change in stiffness is recorded in the response from the well logs by a sharp increase in the P-wave velocity from the sonic log, but also in the bulk density log.

This response characterises the boundary between the MC and CC called transition zone (TZ). As the cementation of the chemical compaction is temperature dependent, the depth of the onset of this one can be calculated from the geothermal gradient in the basin. The difference between the theoretical (calculated) and recorded transition zone is used in the estimation of uplift.

4.4.2 Geothermal gradient :

The chemical compaction regime is temperature dependent and starts around 70°C defining the onset of quartz cementation. At higher temperature (e.g. 80°C) significant presence of quartz cement is assumed. The depth of transition zone and the geothermal gradient are calculated based on these temperatures. The calculation of the gradient is an important element of the compaction study. The gradient is calculated using the following equation (Eq.8):

$$(Eq.8) \quad G = \frac{T_{bh} - T_{sf}}{D_{bh} - D_{sf}}$$

Where **G** is the temperature gradient, **T_{bh}** the bottom hole temperature of the well, **T_{sf}** the temperature at the sea floor (set as 4°C), **D_{bh}** is the maximum depth of the well (in m TVD) and **D_{sf}** being the depth to the sea floor from sea level. The calculated geothermal gradient may be different from the one existing at the sediment deposition. The present geothermal gradient might not have been the same as millions of years ago, and the present calculated temperatures are most likely underestimated.

4.4.3 Well logs :

Sonic log: Acoustic velocity

The sonic log measures the interval transit time, **ΔT**, of acoustic waves going through the rock surrounding the well. The interval transit time is the inverse of sonic transit velocity. The velocity of sound in water, here the pore water, is lower than the minerals and rocks, the measured velocity will be inversely proportional to the rock porosity (Bjørlykke, 2010). The velocity is also dependent of the quantity, nature and distribution of cement. The P-wave velocity, **V_p**, is calculated using the formula below (Eq.9):

$$(Eq.9) \quad V_p \text{ (m/s)} = \frac{1}{\Delta T} \times 304800$$

The velocity is highly dependent on the stiffness of the formation. As soon as the chemical compaction started, the cementation will increase the stiffness and consequently the V_p values. The sonic log is then a good tool to estimate the depth of the transition zone.

Gamma ray log :

The gamma ray log measures the natural radioactivity produced in the rock. The radioactive elements present in sedimentary rocks are potassium, thorium and uranium. The strongest radiation is found in shaly formations due to their high content in those elements. The gamma log is then used to discriminate the sand from the shale layers in a formation by giving a sand/shale ratio. Sandstones with a high content in feldspar and mica will show a greater gamma ray measurement than purer quartzose sandstones (Bjørlykke, 2010, 2015). The gamma ray log is here used to discriminate the lithology. Shales show the highest gamma ray, while halite, anhydrite, clean sandstones and dolomite have the lowest values

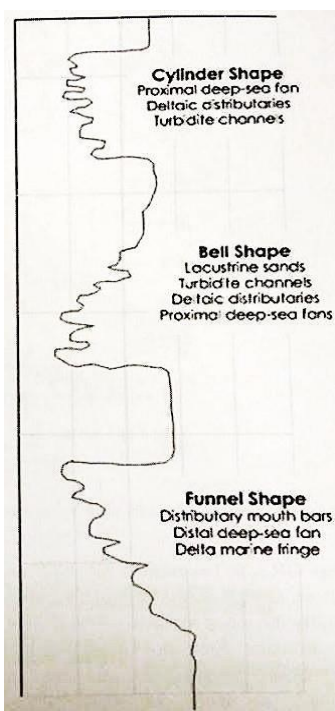


Figure 17: Representation of the different shape of Gamma ray curves from Mondol in Bjørlykke (2015)

(Mondol in Bjørlykke, 2015). The gamma ray log is also used to discriminate facies and depositional environments as shaliness usually change gradually with depth and this way suggests a litho-facies and depositional environments. By analysing the shapes of the gamma ray curve illustrated in Figure 17, the interpretations below can be made from Mondol in Bjørlykke (2015):

- Cylinder shapes: uniform deposition, interpreted as aeolian dune, tidal sand, fluvial and turbidite channel, as well as proximal deep sea fan deposits.
- Bell shapes: finning upwards sequences, interpreted as tidal sand, alluvial sand, fluvial channel, point bar, lacustrine, delta, turbidity channel and proximal deep sea deposits.
- Funnel shapes: coarsening upwards sequences, interpreted as barrier bar, beach sand and crevasse splay, distributary mouth bar and distal deep sea fan deposits.

Bulk density log:

The density log measures the density of the rock and its pore fluid by measuring their electrodensity. The electrodensity is closely related to the bulk density in g/cm^3 , giving

important information to identify the lithology of the formation.

The density log is also used to calculate the porosity using the formula below (Eq.10):

$$(Eq.10) \quad \text{Porosity} = \frac{\rho_m - \rho_b}{\rho_m - \rho_{fluid}}$$

Where ρ_m is the density of the rock matrix ($\rho_m=2.65 \text{ g/cm}^3$ in pure sandstones), ρ_b the density driven by the log, the bulk rock density, and ρ_{fluid} is the fluid density (ρ_{fluid} is brine water = 1.025 g/cm^3). From this the density log can record a change in fluid. The most common densities of mineral in sandstones used in this thesis are presented in table 5.

Table 5: Table gathering the most common densities of mineral found in sandstones.

Mineral or fluid	Density (g/cm ³)	Mineral or fluid	Density (g/cm ³)
Quartz	2.65	Kaolinite	2.59
Calcite	2.71	Illite	2.66
Dolomite	2.87	Smectite	2.1-2.6
Albite	2.61	Formation water	1.025
Biotite	2.90	Oil	0.85
Muscovite	2.83	Drilling mud	1.35
Chlorite	2.80		

Neutron log :

The Neutron log measures the hydrogen index of the formation. Most of the hydrogen atoms are contained in fluids so the hydrogen index can be correlated to the amount of pore space in the formation. However, even if the neutron log is a good tool to determine porosity, it can lead to overestimation in clay-rich formation as hydrogen is contained within the structure of clay minerals, called the shale effect. In gas bearing formation, the neutron porosity will lead to an underestimation of the porosity because gas has fewer hydrogen atoms per unit of volume than water or oil, called the gas effect. In the same settings, the neutron log can be used as discriminator between gas and oil bearing formations. Organic matter has a high hydrogen index, and in clean sandstones and limestones, the neutron log is a great tool to determine the porosity of reservoir rocks (Bjørlykke, 2010, 2015)

Permeability estimation:

The permeability is defined by the ability of the fluid to pass through the pore space. This ability depends on the interconnectivity between the pore spaces. The permeability

estimation is one of the most important parameter for the reservoir characterization but is the least predictable (Torskaya et al, 2007). Porosity is the most important factor influencing the permeability but not the only one. Other factors, such as pore throat diameter and shape, wetting angle, capillary pressure and the presence of impermeable shale layers acting as barrier have also to be taken in account. The large amount of factors makes the permeability very difficult to assess using well logs and is usually estimated using helium injected in samples or by CT scans. Wyllie and Rose (1950) suggested an empirical equation to calculate permeability using porosity and water saturation from neutron porosity log (Torskaya et al, 2007). The Timur's equation as presented below was used to calculate the permeability.

$$K = a \frac{\phi^b}{S_{wi}^c}$$

Where, **K**- is permeability, **S_{wi}**- is the water saturation and, **a= 8, 58**; **b=4,4**and **c=2** are model parameters (Torskaya et al, 2007).

V. Results:

5.1 Sedimentological analysis:

The sedimentological analysis of the Triassic Snadd Formation is based on the observations of the cores and thin sections of samples from those cores. The sedimentary facies description is made jointly for the two wells 7122/6-2 and 7226/2-1.

The log of the section of the well 7122/6-2 (2452-2506m) presented in Figure 19 shows a general and very gradual coarsening upwards from mud to fine sand grain size. The mud/sand ratio is very varying all along the core; even up-core where the grain size is coarser the mud/ratio stays high (Fig.19). The mud-rich coarsening upwards sequence is disturbed by highly bioturbated sand rich units of approximately 5m every 10m throughout the core (Fig.19). Some cyclic dolomite rich intervals have been observed, 1,5m thick interval every 1.5m over the upper half of the core (2452-2480m). In those intervals, the dolomite is present in very varying size of crystals and mixed with some clastic deposits and clay minerals. The dolomitic intervals are often cut by thin sand lenses of 30cm thickness. Heterolithic bedding is observed throughout the core with higher intensity middle to down

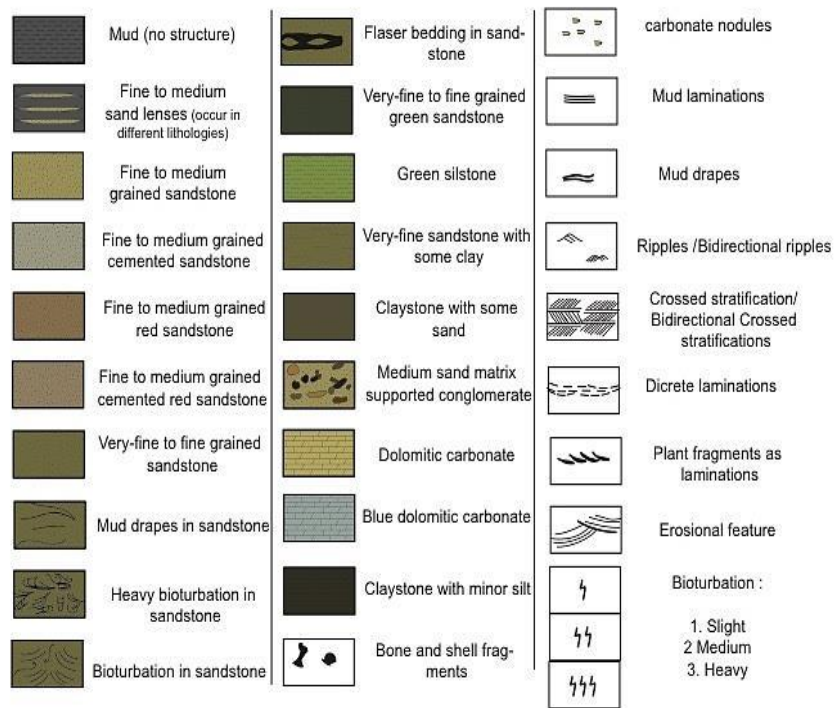
core (2470-2506m depth). One conglomerate and bone fragments unit is occurs as one single event in a 50cm interval up core (2453m depth).



Figure 18: Pictures from the interval 1368-1369m (A) and from 1380-1382m (B). The higher mud content (A) compared to the lower part of the core makes them more visible.

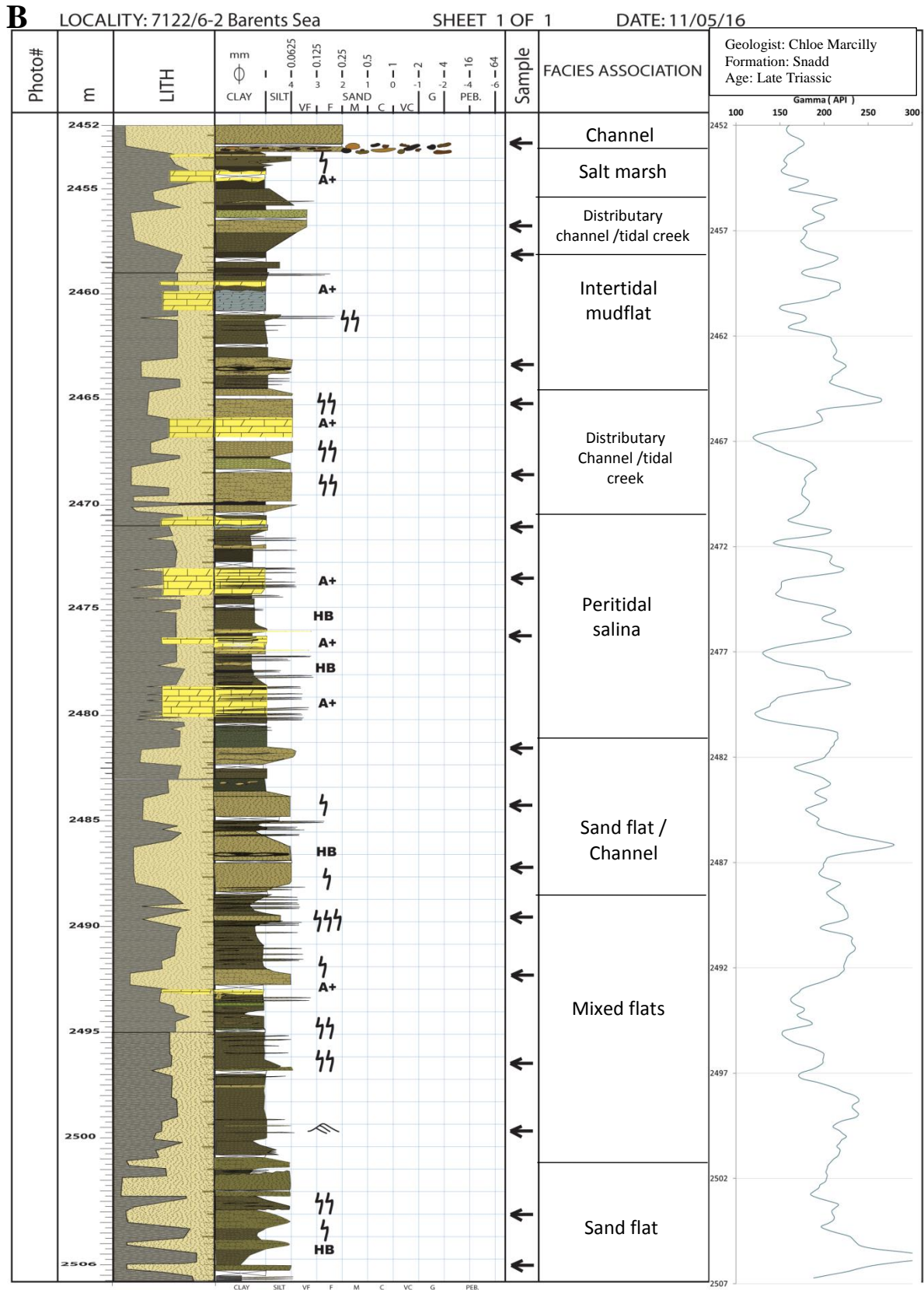
The log of the section of the well 7226/2-1 (1365-1418m) presented (Fig. 20) shows a constant lithology of fine to medium sandstone with cross bedded intervals. Only unidirectional cross bedded units are found in the lower-middle part of the core (1370-1418m) whereas the upper part of the core is marked by bidirectional cross beds (Fig.18). The mud content increases gradually up core. Mud clasts and plant fragments are found as laminations throughout the core and no sign of bioturbation was observed. Some calcite cemented intervals have been observed; no pattern in their appearance could be noticed. Red colored beds also occurred sparsely.

A Legend for the logs of Core 7226/2-1 and 7122/6-2



A+ responds to acid treatment HB Heterolithic bedding L-WB Lenticular to wavy bedding FB Flaser bedding

Figure 19: A) Legend for the digitized compressed logs of the sections for the 7122/6-2 and 7226/2-1 wells (Fig.20). B) Digitized compressed log of the logged section of the well 7122/6- 2 (2452-2506m depth). The facies associations of the intervals are disposed next to the corresponding area on the right and the gamma ray signature trough depth (m) in the last column. The black arrows represent the location of the studied samples.



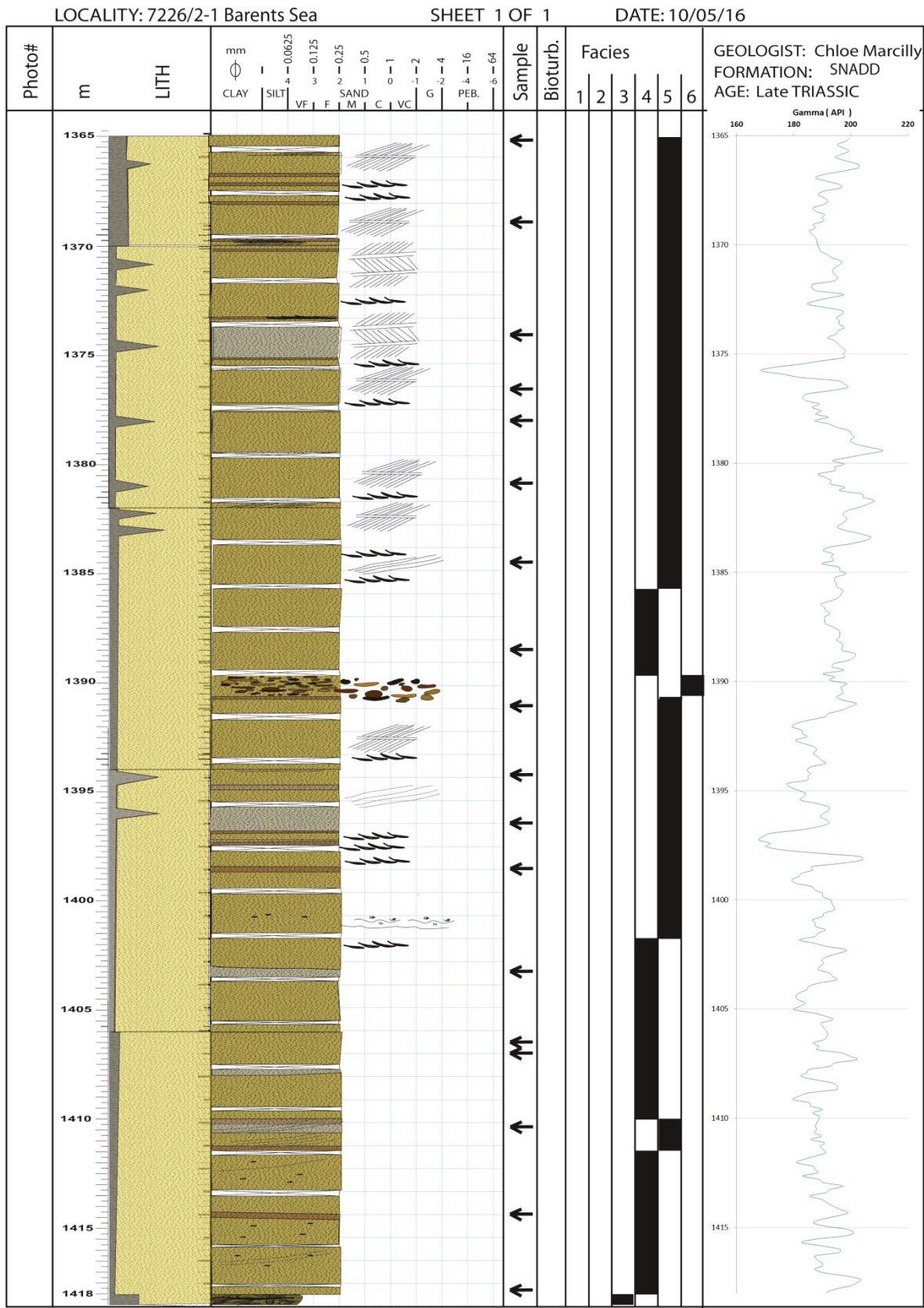


Figure 20: Digitized compressed log of the logged section of the well 7226/2-1 (1365-1418m depth). The facies associated are disposed next to the corresponding area on the right and the gamma ray signature trough depth (m) in the last column. The black arrows represent the location of the studied samples. Legend on Figure 19.

5.1.1 Facies description :

F1 : Heterolithic bedding in claystone and fine-grained sandstone :

F1 is composed of claystone or sandstone with fine, sparse sand laminations. This facies occurs repeatedly throughout the core 7122/6-2. Its thickness ranges from 3 to 5m. The laminations are changing through the cored intervals, making a subdivision of this facies necessary (Fig 21).

F1.A: Planar laminated claystone

F1. A consists of dark grey to black claystone containing thin parallel laminations of very-fine grained sand (Fig.21). The upper and lower boundaries are mostly gradual. The lamination is sometimes disturbed or destroyed by bioturbation. This sub-facies is mostly observed in the well 7122/6-2.

F1. B: Lenticular to wavy bedded claystone:

This sub-facies is alternating with facies F1. A. The amount of sand is varying, driving the sedimentary structures towards lenticular or wavy bedding. The upper and lower boundaries are mostly gradual.

F1.C: Mud-drapes and planar laminations to flaser bedded sandstones.

This sub-facies consists of alternating mud-drapes and sand, sometimes planar laminations. Flaser bedded structures form where the sandy lenses show typical cross-stratified current ripples. The intervals are sparse. Some of these intervals are disturbed by bioturbation.

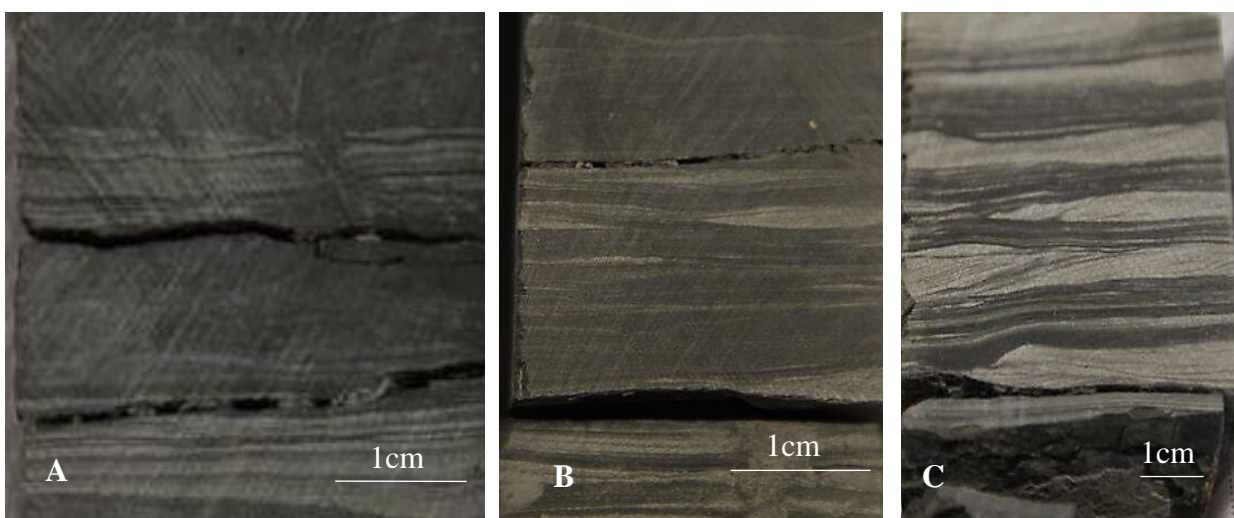
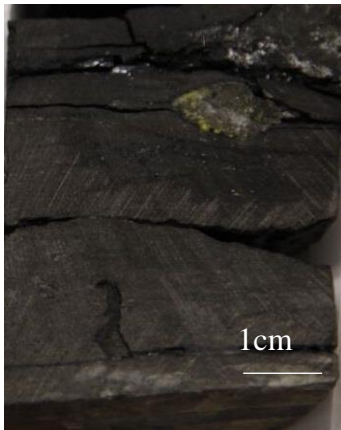


Figure 21: Picture of the sub-facies for the facies F1. A) Facies F1. A; B) Facies F1. B and C) Facies F1. C.

F2: Silty claystone:

This facies (Fig.22) is characterized by dark grey claystone and is usually alternating with facies F1. B. The upper and lower boundaries are gradual. No sign of bioturbation was found. This facies is present only in the well 7122/6-2.

Figure 22: Picture of the facies 2 (F2).

F3: Bioturbated sandstone :

This facies is composed of very fine grained bioturbated sandstones (Fig.23). The grain size of those sandstones increases gradually from very fine to medium sand towards the top of the core 7226/2-1, whereas in the core 7122/6-2 they are present only as mud-rich deposits. Based on the grain size, this facies unit is divided into two sub-facies found in each core.

F3. A: Highly bioturbated sandstone:

This sub-facies consists of highly bioturbated sandstones with minor amounts of mud. Those intervals have gradual upper and lower boundaries. Clear evidence of burrowing activity was observed. This sub-facies is observed in both wells but more extensively in the 7122/6-2.

F3. B: Mud-rich heavily bioturbated sandstone:

This sub-facies is characterized by fine to medium sand mixed with muddy intervals. All structures are destroyed by bioturbation. Clear evidence of burrowing activity is observed. This unit is present only at the base of the core 7226/2-1 and represents 50cm (Fig.20).

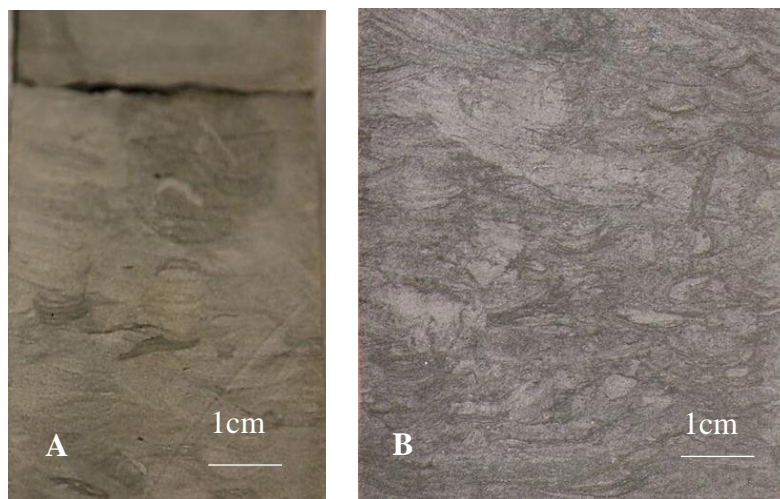


Figure 23: Pictures of the sub-facies of the facies 3 (F3). A) Facies F3. A and B) Facies F3. B.

F4: Structureless massive sandstone :

F4 consists of very fine grained to medium sand, presenting no clear sedimentary structures (Fig.24). The observed diversity in term of color and texture in this sandstone unit makes a subdivision of the unit necessary. In the well 7226/2-1, all sub-units are present whereas only the facies F4. A is present in the well 7122/6-2 (Fig.19).

F4. A: Massive sandstone

This sub-facies is characterized by fine-medium sandstones with localized laminations composed of mud drapes and plant fragments. The laminations are sparse along the core 7226/2-1. This unit comprises the majority of the core 7226/2-1 (Fig.20) but only small intervals of the top-core 7122/6-2 (Fig.19).

F4. B: Red colored sandstones.

This sub-facies consists of red colored sandstones localized as layers of approximately 20cm, occurs sparsely throughout the core 7226/2-1. The lower and upper boundaries are gradual.

F4.C: Cemented sandstone intervals.

The upper and lower boundaries of this sub-facies are gradual. The cement responds to acid treatment indicating carbonate cement. These intervals occur as 50-100cm intervals all throughout the core 7226/2-1 (Fig.20).

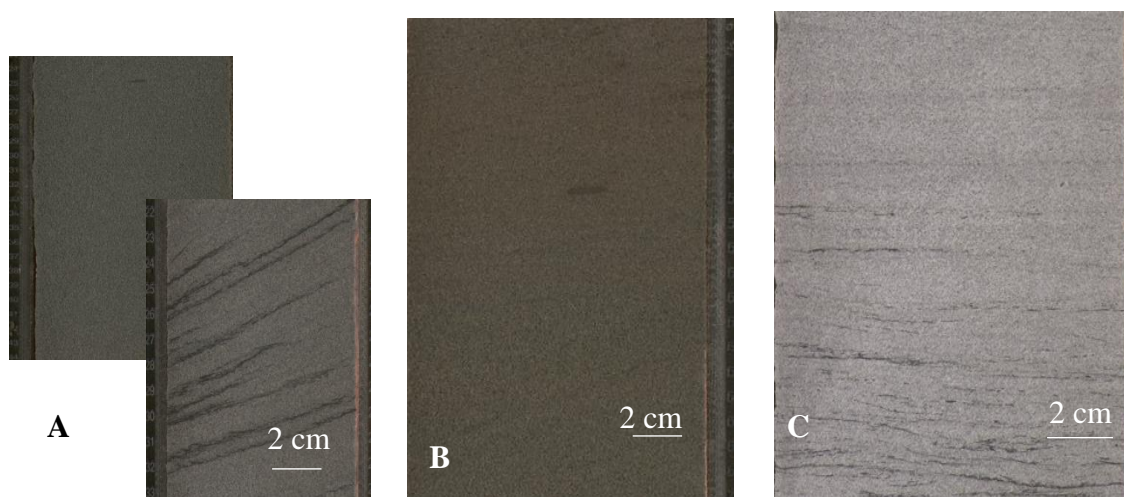
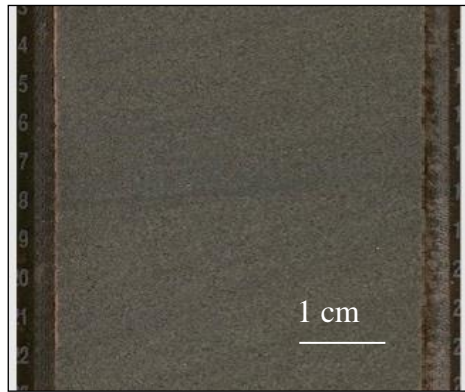


Figure 24: Picture of the sub-facies of the facies 4 (F4). A) Facies F4. A. B) Facies F4. B and C) Facies F4. C.

F5: Cross bedded sandstones:

This facies consists of discrete cross beds of sandstones cutting on one another (Fig. 25), and is only present in the well 7226/2-1. The fine to medium grain size is constant. An increase in mud content in the crossed laminations towards the top of the core is observed.

Figure 25: Picture of the facies F5.

F6 : Conglomerate:***F6. A: Matrix supported conglomerate:***

This sub-facies consists of matrix-supported conglomerate (Fig. 26) with clasts and grains composed of bones/shell fragments, and pebbles. The clasts are poorly sorted and subrounded with a subhorizontal orientation. This layer occurs as a unique layer of 25cm on the top of the core 7122/6-2 (2453m depth, Fig.19). The lower boundary is gradual but the upper boundary is erosive. Bioturbation occurs sparsely.

F6. B: Matrix supported smaller grains conglomerate:

This sub-facies is composed of fine to medium sand matrix conglomerate composed of reddish clasts that do not respond to acid treatment (Fig.26). The clasts are poorly sorted, elongated to rounded. The boundaries are gradual. This facies occurs only once as a 50cm layer in the middle of the core 7226/2-1 (1390m depth, Fig.20).

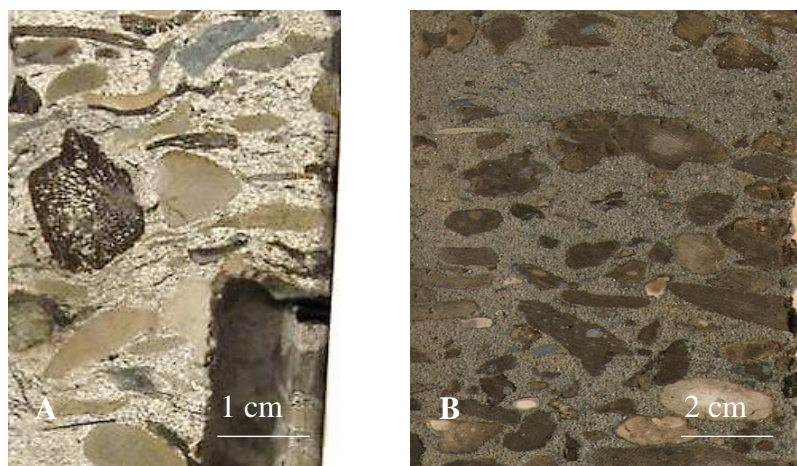


Figure 26: Picture of the sub-facies of the facies 6 (F6). A) Facies F6. A. and B) Facies F6. B.

F7: Dolomite cemented deposits:

Figure 27: *Picture of the facies 7 (F7)*

This facies (Fig.27) is present only in the core 7122/6-2 as cemented intervals with gradual lower and upper boundaries. The cement is reacting to acid treatment indicating a carbonate composition. The intervals show a range of colors from green/blue to brown. No grains are visible. Sand lenses with bioturbation occur sparsely. Nodules of this unit can be found within other units. An interval of 20cm in this unit is showing chicken-wire pattern (2476, 4m depth, Fig.19). This facies comes with cycles of 1,5m thickness every 1,5m of core on the second half of the core (2452-2480m depth, Fig.19).

5.1.2 Facies association :

The sedimentary facies have been grouped in five facies associations called here sub-environments (sub-env) and are presented in the table 6. The sub-environments are described by their sedimentological content such as mud/sand ratio and sedimentary structures: They are referenced here as SE for sub-environment and the number attributed to each of them. Those sub-environments have also been grouped into two main environments representing the facies associations, based on the modern observations of depositional environments.

Table 6: facies associations for the well 7122/6-2 and the well 7226/2-1

FA#	Env	Sub-env	Geological features	Facies
FA1	Tidal influenced delta	SE1 Tidally influenced channel	<ul style="list-style-type: none"> Sandy deposits alternating with muddy intervals. Cross bedding, sign of bidirectional current. Mud clasts and plant fragments from the lower delta plain acting as conglomerate May be overlaid by fluvial channel or intertidal deposits. 	F3 F4 F6
		SE2 Tidal flat	<ul style="list-style-type: none"> Heterolithic deposits Lower sand: mud ratio Sign of bidirectional current Presence of tidal bundles 	F1
		SE3 Intertidal zone: mudflats	<ul style="list-style-type: none"> Lower sand: mud ratio Intense bioturbation Lenticular /flaser beddings Sign of bidirectional currents Coarser sediment in tidal creeks 	F1 F2
		SE4 Peritidal salina pan	<ul style="list-style-type: none"> Chicken wire structure Dolomite. Carbonate deposits Sand lenses High mud content in over/under-lying deposits 	F7
FA2	Coastal plain	SE5 Meandering channel	<ul style="list-style-type: none"> High sand: mud ratio Visible cross beds Massive unit of cross bedded/cross laminated sands. Plant fragments Scour base of channel No sign of reworking Sign of overbank deposits 	F4 F5 F6

5.2 Petrographic analysis :

5.2.1 Well 7122/6-2: Hammerfest Basin:

The well 7122/6-2 presents a highly variable mineral composition. The topmost and lowermost samples are sandstones deposits, while most of the core is composed of dolomite layers and mudstones (Fig.18). The sandstones deposits have a characteristic composition in majority of quartz, rock fragments and feldspars. All the samples present a large amount of infilling clays among which chlorite and illite are the most abundant from the XRD analyses. The grain size is very variable, making difficult the identification of minerals for some samples of the well where the grains were of clay-silt size (Fig.28). The dolomitic deposits are composed of dolomite cubic crystals of size ranging from 1-2,5 μm to 20 μm . In these intervals, clastic deposits such as quartz grains, K-feldspar, and mostly muscovite have been observed in a chaotic mixture with grains ranging from 2 to 60 μm . Quartz is also represented as overgrowths throughout the core.

Mineralogical and textural description:

Grain size and sorting:

The grain size in the well 7122/6-2 is varying between fine sand to clay size grains. Most of sandy intervals are represented by very-fine sand. In the samples represented by clay size deposits, no measurements of grains or point counting could be carried out (Fig 28). Those clay size intervals are often characterized by dolomite crystals or pore-filling clays minerals. The sorting in the sandy intervals is represented by a standard deviation alternating between 0,4 to 0,8 with an average at 0,56. Those standard deviation values are typical for moderately sorted intervals. The majority of the grains are subangular to subrounded.

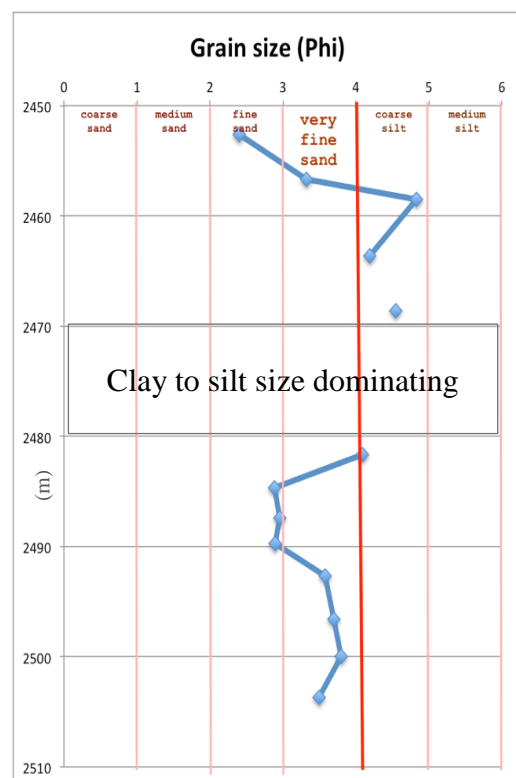


Figure 28: Graph showing the grain size distribution for the well 7122/6-. The red line corresponds to the mean grain size of the core.

Mineralogy:

The mineralogical assembly differs for the dolomitic and sandstones intervals. The sandstones are composed in majority of quartz, feldspars and micas. Clays minerals are present in high amounts (Fig. 29). Due to the small amount of point counted samples, the XRD data are taken as reference for the core 7122/6-2. The dolomitic intervals are composed for the most of 40-70% dolomite, 5-20% quartz, 5% calcite and 5% illite from the XRD data (Fig.29). From the Profex analysis, the composition of the infilling clays can be assessed as being mostly chlorite and smectite. Illite and mica participate with a small amount up to 5%.

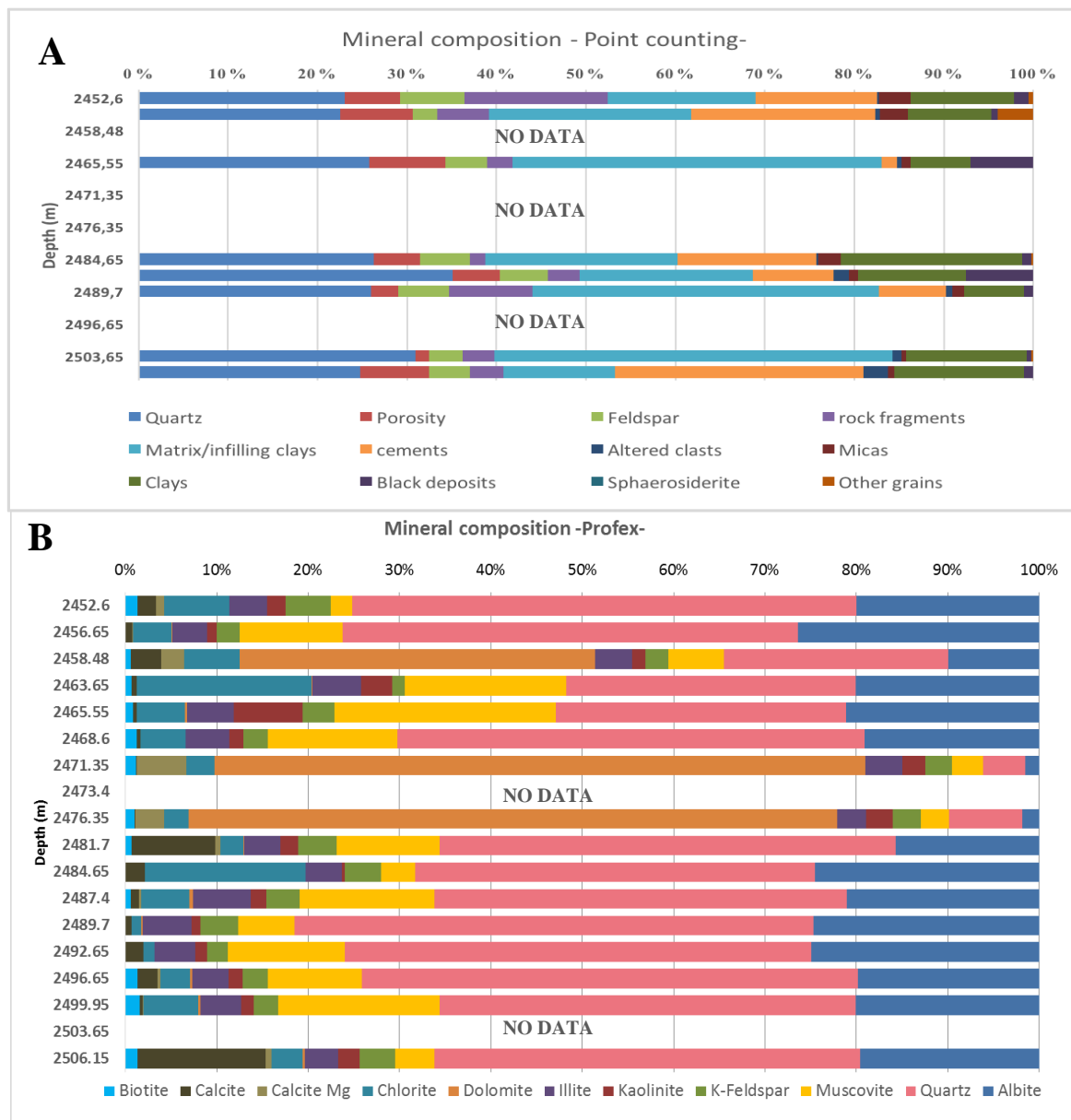


Figure 29: Graphs showing the mineral composition of the collected samples from the well 7122/6-2. A) Mineral composition from the point counting. Some of the intervals couldn't be identified due to the very small grain size. B) Mineralogical composition of selected phases from the Profex software. Some samples where no data appears represent unreadable files from the program.

Heavy minerals such as apatite and rutile are found in all the samples of the core but in negligible amounts. An overestimation of quartz and feldspar grains may exist due to the fact the Profex distinguish each component of the rock fragments.

Detrital minerals:

Quartz:

The quartz content in the samples of the well 7122/6-2 ranges between 4 - 55% and averages at 41% of the rock volume. Quartz is then the most present mineral of the sandstone assemblies and the second one in the dolomitic samples. The quartz is mostly present as monocrystalline quartz, around 80%, while the polycrystalline represents 20% to <10% (Fig.30). The quartz concentration is stable all along the core with a slight decrease on the upper part of the core (2452-2458m) (Fig.30). The quartz also appears under quartz cementation/overgrowth treated in the authigenic minerals part.

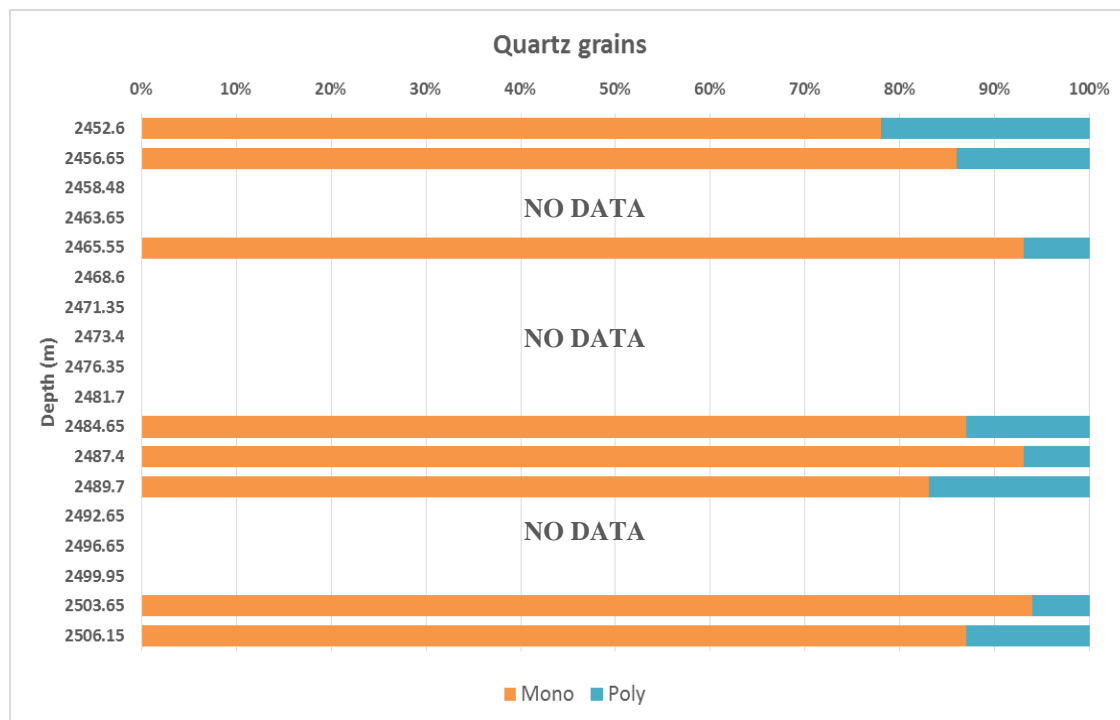


Figure 30: Distribution with depth of the monocrystalline and polycrystalline quartz grains from the point counting. Areas where “NO DATA” appears represent intervals where no point counting could be carried out.

Feldspar:

Albite is the dominant feldspar mineral in the studied samples, and averages to 18% of the rock volume in the sandstone samples from XRD analysis (Fig.29). Albite is almost absent in the dolomitic samples. From the point counting analysis, plagioclases are more present than microcline up to 70% against 30% in average for microcline (Fig.29). A discrete trend to decrease in microcline abundance with depth could be identified. The degree of weathering for the plagioclases is mostly comprised between 4-5° (Fig.31). Microcline represents between 2-5% of the rock volume in all the samples (Fig.29). Microcline grains show degrees of weathering between 3-5° so a lower degree of weathering than the plagioclases (Fig.31). No trend in the distribution of weathering degree could be identified. The degree of weathering is not facies related.

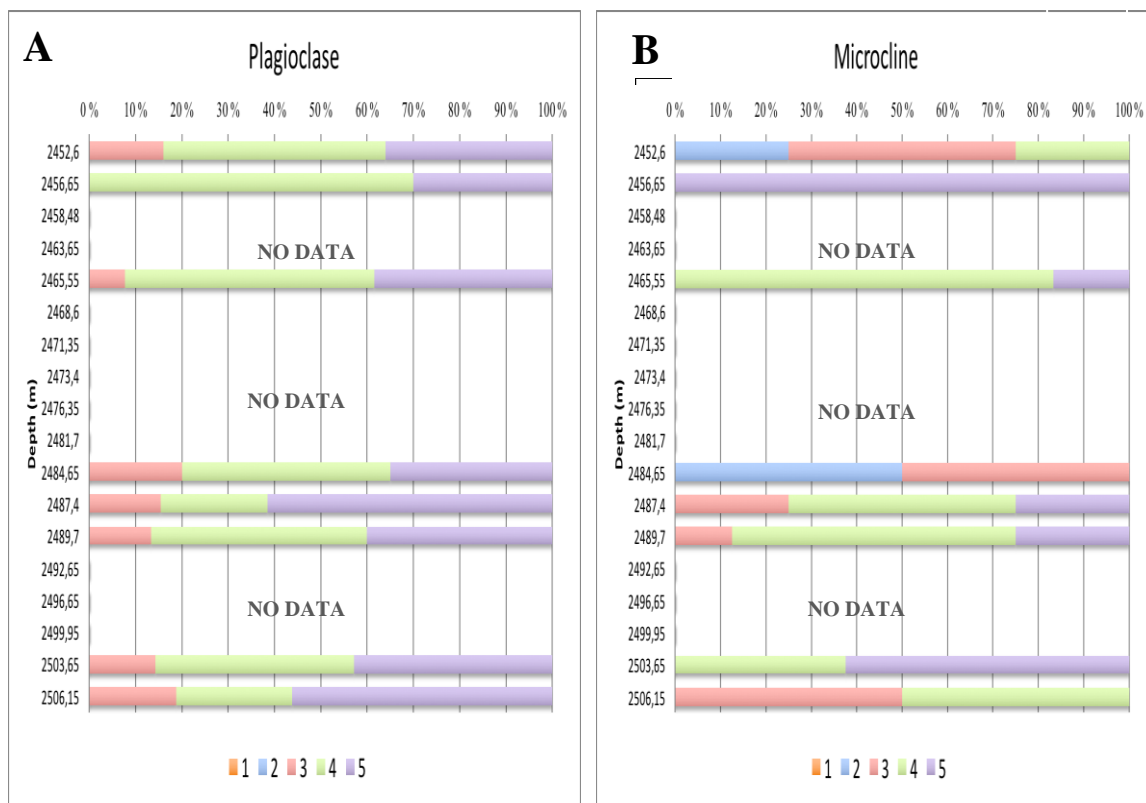


Figure 31: Distribution of the weathering degree of the feldspars with depth in the well 7122/6-2. The areas of no data correspond to intervals where point counting was not carried out. A) Distribution of the weathering degree for the plagioclases, identified with the polysynthetic twinning. B) Weathering degree distribution of the K-feldspar identified thanks to the crosshatched crystal twinning of the microcline.

Rock fragments:

The rock fragments assembly shows a high degree of weathering making the identification of the minerals involved in their composition difficult. Among the fragments the difference was made between chert, lithic fragments, epiclasts, schistose fragments (metamorphic) and shale fragments (Fig.32). The dominant type of rock fragment is chert, generally highly weathered. Chert is present between 5-24% of the rock fragments volume found in the sandstone intervals. Chert is present at its most preserved from to lower to middle core (2487-2506m) whereas the altered chert is found all along the core. The lithic fragments are the second most representative rock fragment associated with altered lithic fragments, found in the sandstone intervals, from 2-20%. Well preserved lithic fragments are found all along the core but with a higher proportion on the upper core (2452-2456m), whereas altered lithic fragments are present also all along the core but in higher concentration down core (2454-2506m) (Fig.32). The schistose fragments are found on the whole section. The shale fragments are present only on the middle to upper parts of the core (2452-2484m). Finally, the epiclasts which are the least represented in the assembly are only present on the lower part core (2487m, 2503m) (Fig.32).

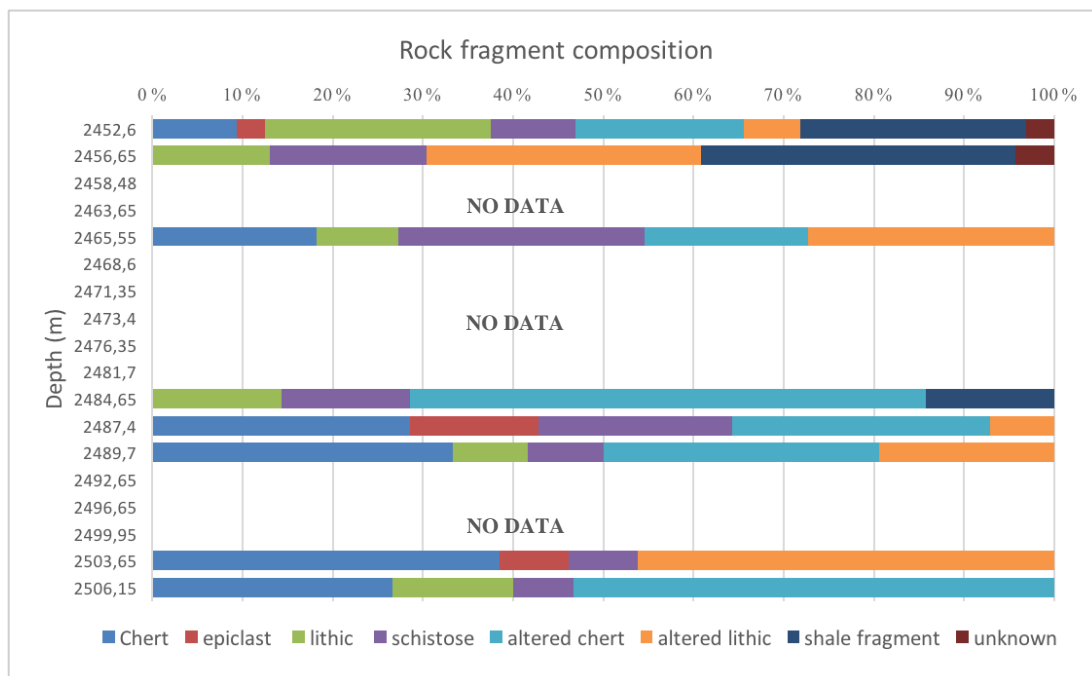


Figure 32: Distribution of the type of rock fragments with depth from the point counting. The identification is difficult due to the high degree of weathering of the fragments. Nevertheless 6 categories could be identified. The unknown class represents highly altered fragment where the origin was impossible to recognize. Areas of no data are represented by very small grain size where no point counting could be carried out.

Authigenic minerals :

Clay minerals:

Chlorite:

Chlorite is the most abundant clay mineral in the core 7122/6-2 ranging from 2-19% of the rock volume and averages at 5% (Fig.29). Clay minerals are present mostly as pore filling deposits but also as replacing grains. Chlorite coating occurs only in two samples in the upper and middle core (Fig.33). In general, the chlorite is more iron rich than magnesium rich, around 15% against 4% of the composition for the Mg. Pseudomorphic chlorite is present as replacement of unstable minerals. This type of chlorite is composed of heterogeneous small chlorite crystals but can also appear as more flaky or bulky crystals. Some of the remnant grain pieces can still be found, mostly when the replaced grains were part of a rock fragment. When replacing mica grains the initial shape is conserved in some cases, with a replacement initiated on the edges.

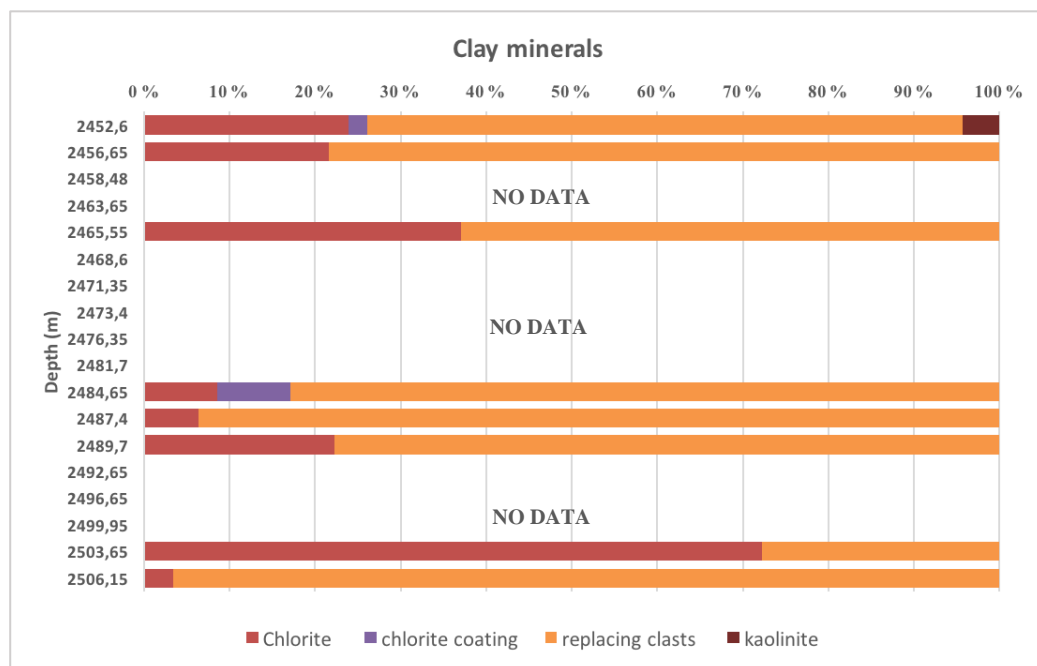


Figure 33: Distribution with depth of the clay minerals from the point counting. The point counting does not allow to give an exact composition of the clays. Only chlorite, chlorite coating and kaolinite due to their characteristic mode of appearance could be identified. The other clays have been identified using the clay fraction XRD and the SEM (Fig.29).

Kaolinite:

Kaolinite occurs in small amounts, with an average of 2% of the rock volume throughout the core, with a maximum of 8% at 2465,55m depth (Fig.29). It occurs as clusters in the intergranular pore space often associated with dissolved grains (Fig.34). The vermiform structure is well preserved even if the grains seem to get bulky indicating a possible transition to dickite.

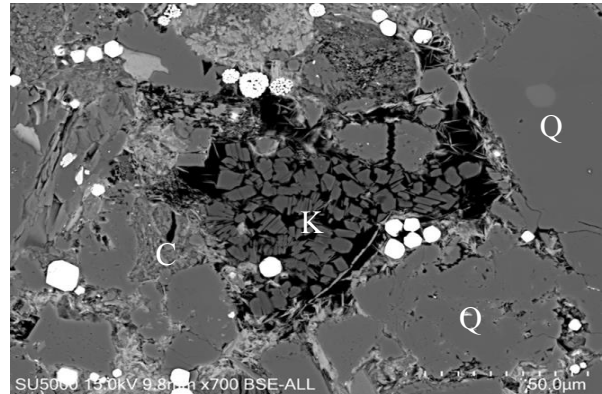


Figure 34: Pore filling kaolinite (K) observed in the well 7122. Grain replacement chlorite © can also be observed. The shiny grains are Rutile and framboid pyrite grains.

Illite:

Illite ranges from 4 - 6% of the rock volume throughout the core (Fig.29). The proportions are based on the bulk XRD data from the Profex software. Extensive areas of hair-needle like crystals have been observed using the SEM and show a tendency to occur as mixed layer with chlorite where they grow over the chlorite (Fig. 35) and quartz overgrowth.

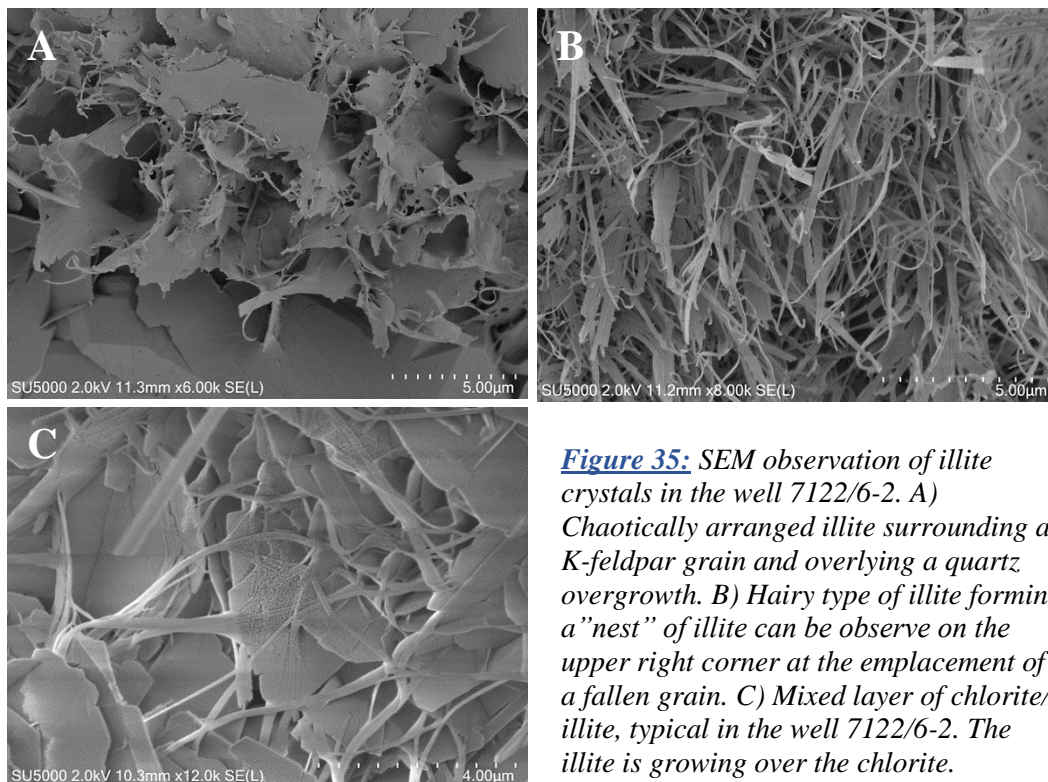


Figure 35: SEM observation of illite crystals in the well 7122/6-2. A) Chaotically arranged illite surrounding a K-feldspar grain and overlying a quartz overgrowth. B) Hairy type of illite forming a "nest" of illite can be observe on the upper right corner at the emplacement of a fallen grain. C) Mixed layer of chlorite/illite, typical in the well 7122/6-2. The illite is growing over the chlorite.

Smectite:

The presence of smectite is assessed only using the bulk and clay fraction XRD analyses and has not been observed directly. Its proportion ranges from 4% to 15% and averages at 8% of the rock volume (Fig.29). Its presence is not related to a particular facies and its distribution seems to be random.

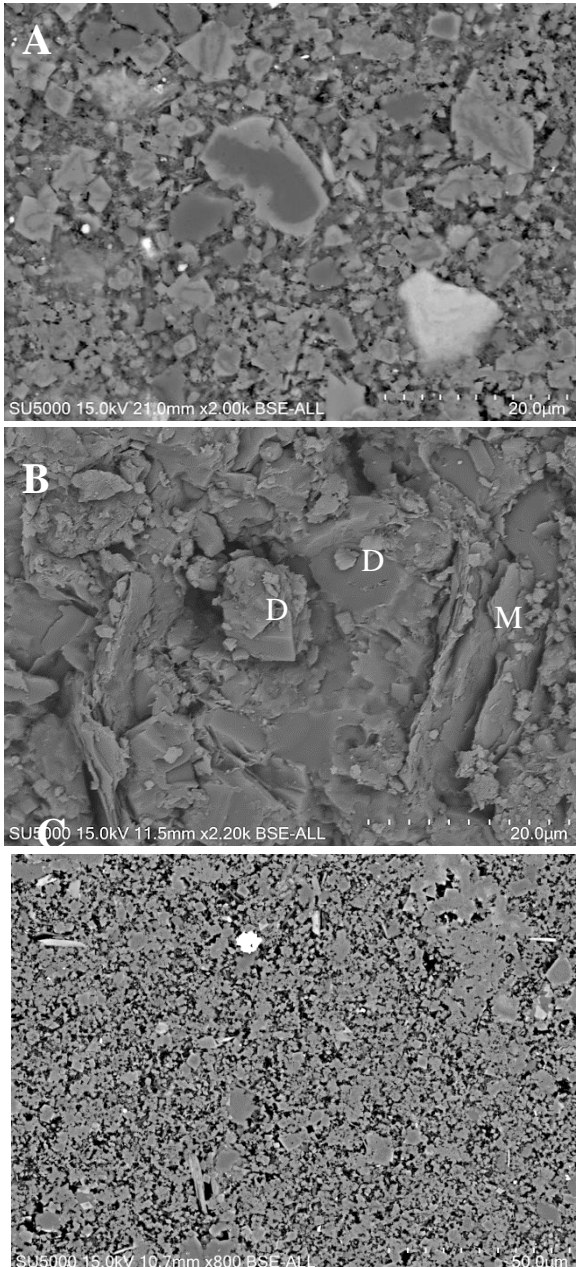


Figure 36: Pictures from the SEM of the dolomitic samples. Among the chaotic appearance, the coarsest dolomite cubic crystals can be observed. The picture A) shows the zonation observed between Ankerite (light grey) and dolomite (dark grey). B) Stub picture of dolomite (D) mixed interval (M=mica). C) Thin section of a dolomite mixed is sample.

Carbonates:

Dolomite:

The dolomite content is based on the XRD analyses in Profex and shows proportions up to 70% in some samples of the middle of the core (2471-2476m depth) (Fig.29). The dolomite is present in a matrix like mixture of dolomite, quartz, muscovite, calcite and clay minerals. During the core logging, the dolomitic layers appeared to be thick with wavy boundaries. Observed at the SEM (Fig.36) those crystals are composed of different sizes from 1-5 μm to 20 μm of poorly to well preserved trigonal-rhombohedral crystals filling the entire pore space (Fig.36).

Calcite:

Calcite in the well 7122/6-2 is present as pure calcite and Mg-rich calcite (Fig.29). The Mg-rich calcite is mostly present on the middle to upper part of the core with a maximum value of 5% of the rock volume. Pure calcite is present all along the core with different proportions going from 1% to 9%, the highest value, occurring only once at 2506,15m depth. The calcite occurs mostly as partial cement even if few calcite grains had been found. It usually shares the pore space with quartz cement.

Quartz cement:

Quartz cement is present in the sandstone intervals up to 20% of the rock volume (Fig 37). When the grains are coated by chlorite, quartz cement grows on the break areas and develops around this coating. The outline of the quartz grains enclosed in quartz cement was difficult to identified leading to a possible underestimation of the quartz cement.

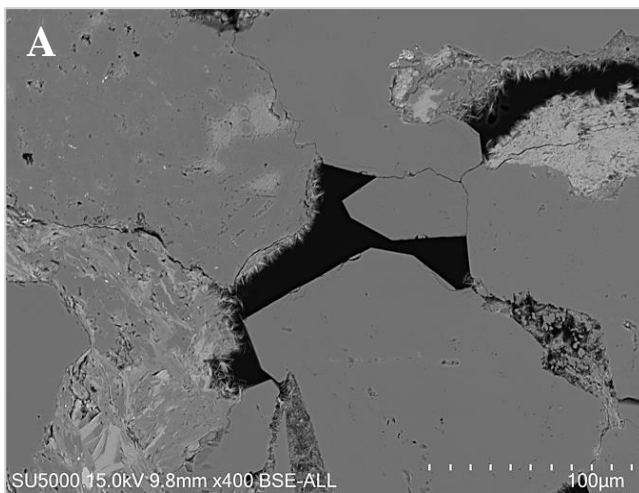
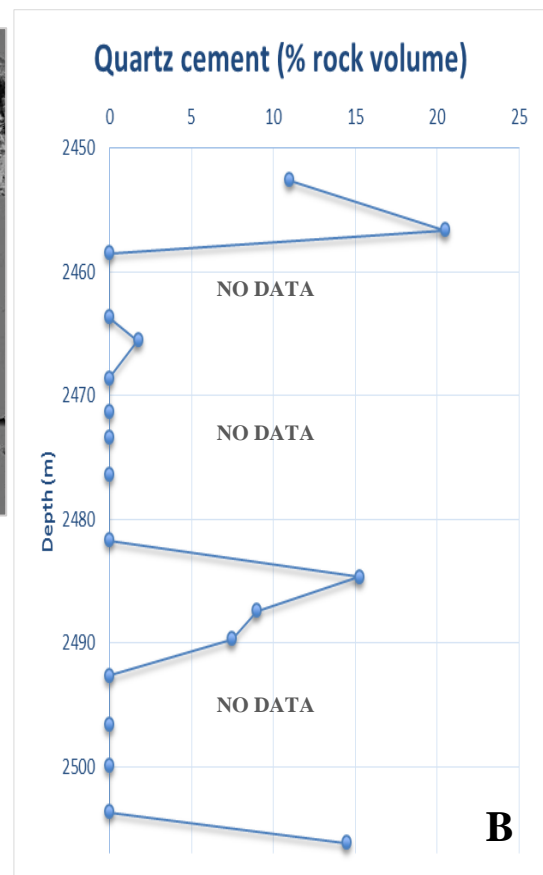


Figure 37: A) Quartz overgrowth observed in the SEM. To see the incomplete chlorite coating allowing more quartz cementation. B) Quartz cement abundance with depth in the well 7122/6-, expressed as % of the total rock volume.



Pyrite:

Pyrite is found in all the samples of the core, the dolomitic ones as well as the sandstones, but in negligible amounts. Pyrite is found under its framboid form but also as more cubic crystals (Fig 38). It appears after and syngenetically with the chlorite platelets of the chlorite coating.

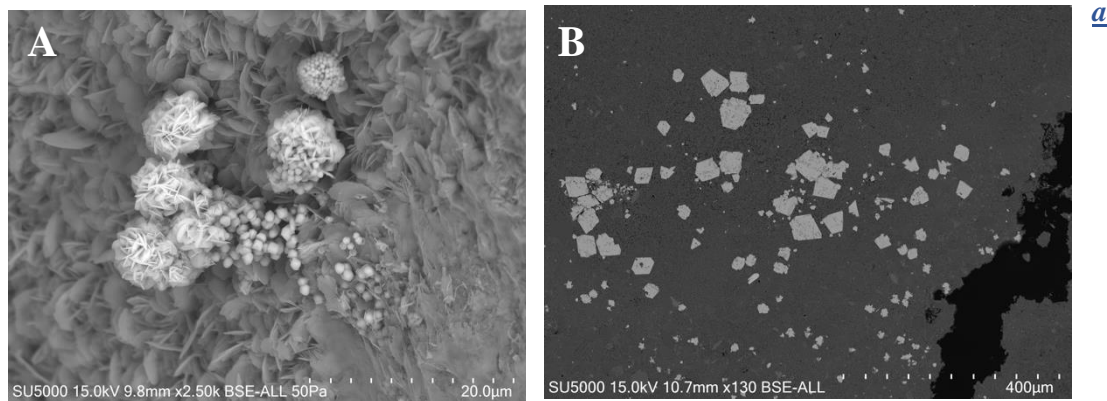


Figure 38: Pattern of occurrence of pyrite grains in the well 7122/6-2 A) The most common framboid shape of pyrite associated with pseudomorphic chlorite filling the pore space observed at the SEM B) Cubic pyrite grains also observed in the well 7122/6-2. The cubic grains are enclosed in the clay matrix, very representative of the well.

Porosity and compaction :

Porosity and permeability:

The porosity in the well 7122/6-2 could be assessed only in the sandstones intervals using the point counting analysis, presented in Figure 39. The porosity in the dolomitic intervals is present as “veins” and combined with the very small grain size of the dolomite cement. For this reason, the porosity couldn't be assessed using traditional methods. Nevertheless, the estimation of the blue epoxy proportion in the thin section using color detection software such as *ImageJ* and neutron porosity can give an estimation of the porosity on those intervals. This estimation is higher than the real porosity since the epoxy can cover partly grains and get into the clay particles. The dolomitic intervals show porosity close to 0% with the highest being at 0, 73%. The sandstones intervals show porosity between 2-9%, with an average being 5%. The porosity is mostly contained in the pore space but also as secondary porosity due to dissolution of grains, especially feldspars. Microporosity is a big part of the overall porosity in this well due to the high amount of mixed layers, chlorite and illite crystals.

The permeability is comprised between 0 and 8, 5 mD and averages around 0, 5mD (Fig.39). The permeability values have been calculated using the water saturation from the neutron porosity log and might not be accurate due to the large amount of clay minerals. Nevertheless, it gives an estimation of its fluctuation throughout the core. Three zones of higher permeability can be observed. They are associated with higher porosity and sand rich intervals.

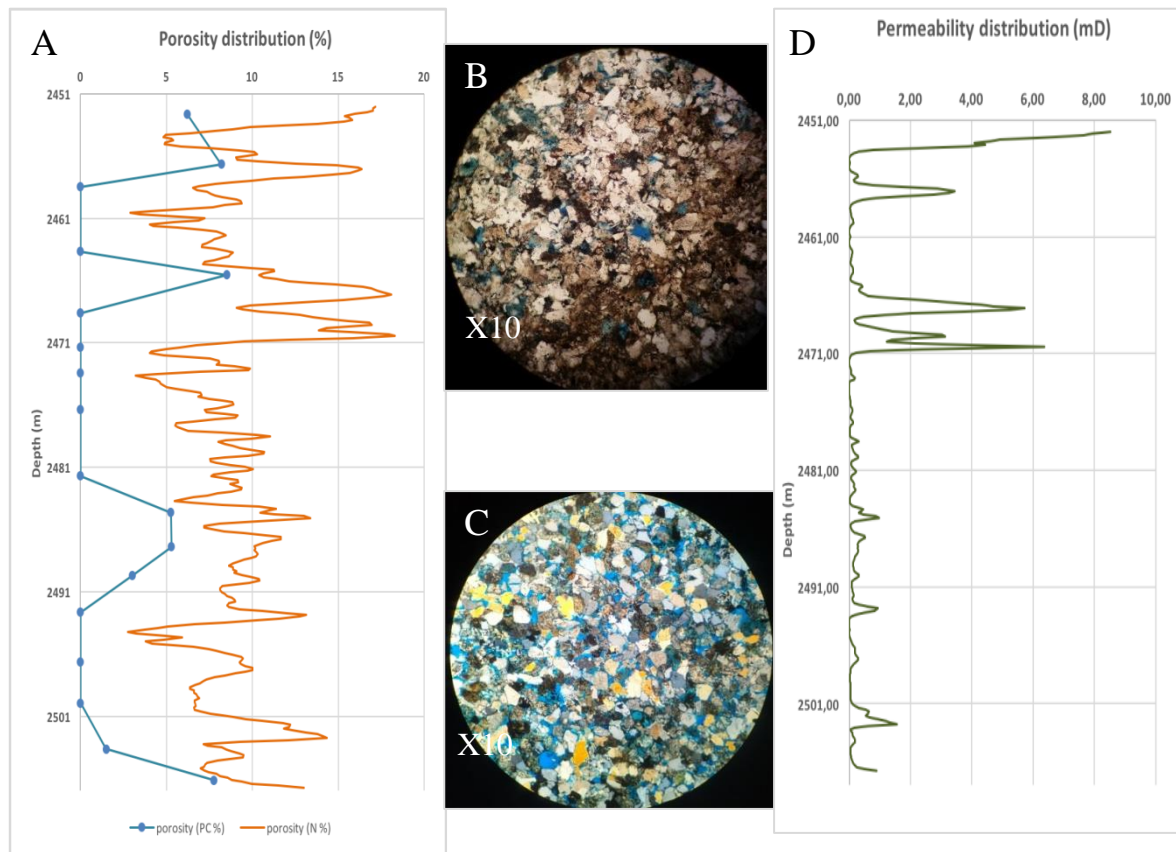


Figure 39: A) Porosity distribution (%) in the well 7122/6-2 from the point counting. The porosity from the neutron porosity log gives overestimated values due to the large amount of clay minerals in the deposits. It is used here as an indication of the trend due to missing data in the point counting. B) C) Typical porosity distribution within the sandstones samples of the well 7122/6-2. D) Permeability distribution curve in the well 7122/6-2, from neutron porosity water saturation.

Grain contact:

The grain contact type was somewhat hard to establish due to the big extent of quartz cement and clay minerals in some intervals of the sandstones. The distribution is presented in Figure 40. The main grain contact type observed in the sandstone intervals was the one called “compacted” meaning that all the sides of the grains were in contact with other grains. In smaller proportion concave-convex contact, as well as long contact and point

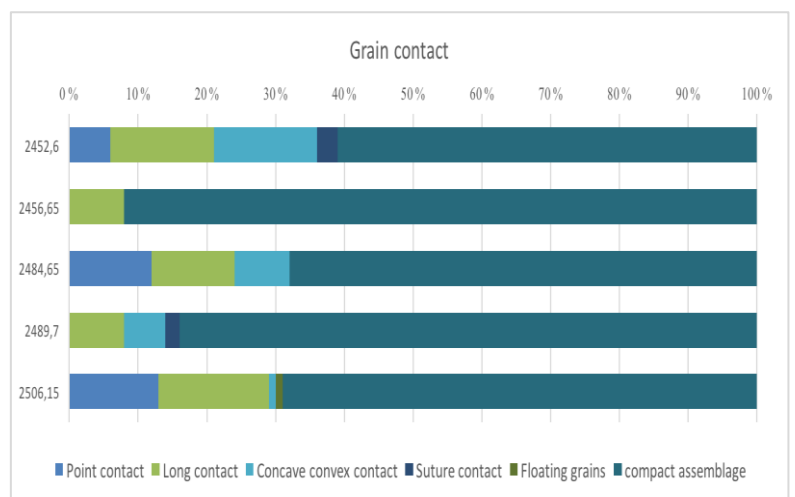


Figure 40: The grain contact type was evaluated only in the sand rich intervals and the distribution was evaluated with depth. The compacted class corresponds to a grain surrounded on every side by other grains.

contact was observed in all the intervals except for the ones between 2492,65m and 2496,62m depth.

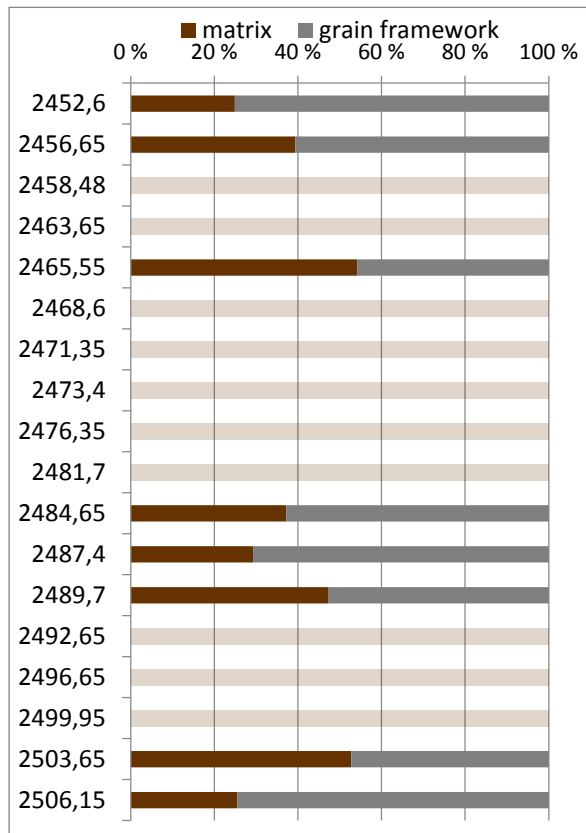


Figure 41: Estimation of the proportion from the point counting of grain framework compared to content for the well 7122/6-2. All the samples with the grain framework proportion on or under the 50% line are considered as matrix-supported. The light brown intervals could not be treated during the point counting process and are observed to be composed mostly of silt/clay size particles.

Intergranular volume:

In the well 7122/6-2 only 6 samples are grain-supported. The IGV can be calculated only in grain-supported deposits and averages at 43.2 % of the rock volume, 2 samples only have IGV under 40% of the rock volume (samples at 2452,6m and 2487,4m depth) (Fig.41). The amount of porosity loss due to mechanical compaction could be estimated only for those two samples and is not representative of the whole well. The sample W1S1 at 2452, 6 m depth and the sample W1S12 at 2487, 4 m depth give a 9.5% of porosity loss due to mechanical compaction. The amount of reduction from chemical compaction is in average 37% of the initial porosity for the grain supported samples. Here, most of the initial porosity is reduced due to the amount of matrix responsible for 59% of the initial porosity reduction in average in the well.

The residual porosity after compaction represents 14% or the original post deposition porosity. All the values are given as an average of the initial porosity loss of the samples in the well defined as 39% (Beard & Weyl, 1973).

5.2.2 Well 7226/2-1: Bjarmeland Platform

The well 7226/2-1 presents a more homogenous mineral composition. The most abundant minerals are quartz, feldspars and rock fragments which are composed in majority of quartz and feldspar as well. The well is also containing, in most of the studied samples, a fair

amount of sphaerosiderites. Clay minerals are present in all the samples. Some of the samples are completely cemented by calcite.

Mineralogical description :

Grain size and sorting:

The grain size in the well 7226/2-1 is mostly fine-grained size except for one sample at 1394,60m depth which is in the medium-grained size fraction (Fig.42). The sorting is represented by well sorted assemblages with standard deviation values comprised between 0, 4 and 0, 6. The grains are subangular to subrounded.

Mineralogy:

The mineralogy was assessed using the point counting and the Profex program reflecting similar proportions in mineral phases (Fig.43). The point counting data are

used as reference for the well 7226/2-1. The most abundant mineral in the core is quartz. It ranges from 30 to 50% and shows an increasing trend upwards; its average proportion is 40% of the rock volume (Fig.43). The second most abundant mineral phase is the rock fragments assemblies, often composed of quartz and feldspar grains, ranging from 5 to 16% with an average value of 11% of the rock volume (Fig.43). Following the rock fragments are the feldspars and more precisely albite with an average of 13% of the rock volume (Fig.43). Clay minerals as grains or matrix occupy on average 17% of the assembly and are mostly composed from allogenic pore filling clays recrystallized as chlorite coating.

Cement is composed mostly of calcite and is present in 4 intervals throughout the core. It can represent up to 25% of the rock volume (Fig.43). Another attention was taken on ooidal shape concretions called sphaerosiderites in this study and are present mostly in the lowest half of the core (1390-1418m depth); these deposits can represent 18-22% of the rock volume when including associated rhombohedral siderite grains (Fig.43).

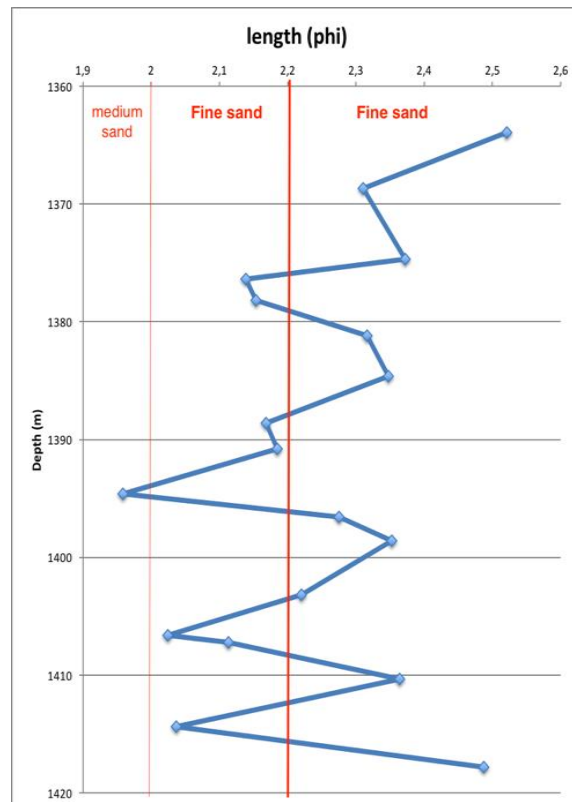


Figure 42: Graph showing the grain size distribution for the well 7226/2-1. The red line corresponds to the mean grain size.

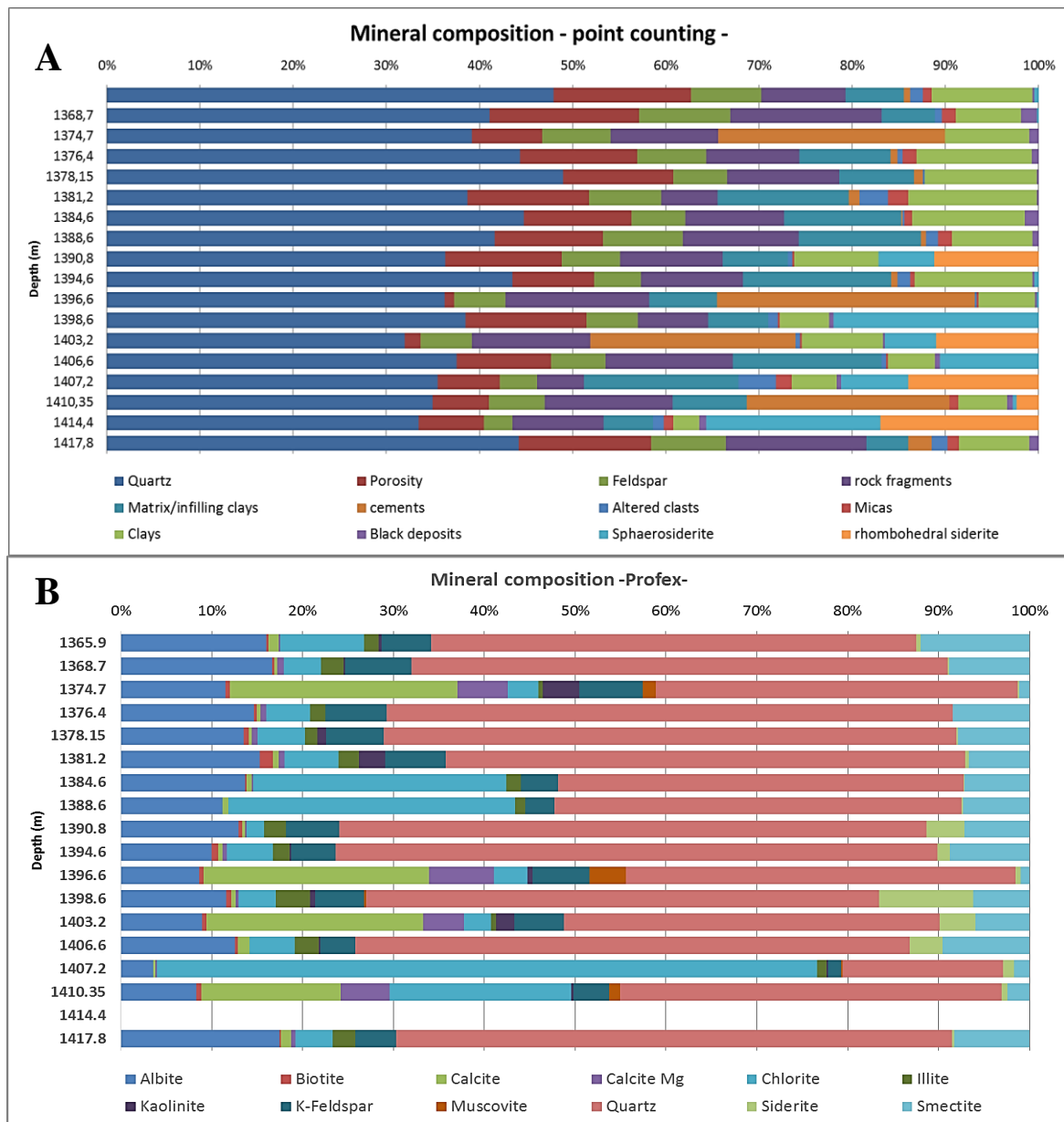


Figure 43: Graphs showing the mineral composition of the samples collected from the well 7226/2-I. A) Mineral composition from the point counting. B) Mineralogical composition of selected phases from the Profex software. One sample, where no data appears, represents unreadable file from the program.

Detrital minerals :

Quartz:

Quartz is the most present mineral in the core and almost reaches 50% of the mineralogical composition. Nevertheless, except for the very last sample the trend decreases in its proportion with depth with a lowest value of 32% at 1403,20m depth (Fig.43). The quartz grains are mostly represented by monocrystalline form even if the polycrystalline grains can reach proportions from 9 to 23% with an average of 15% of the quartz content (Fig 44).

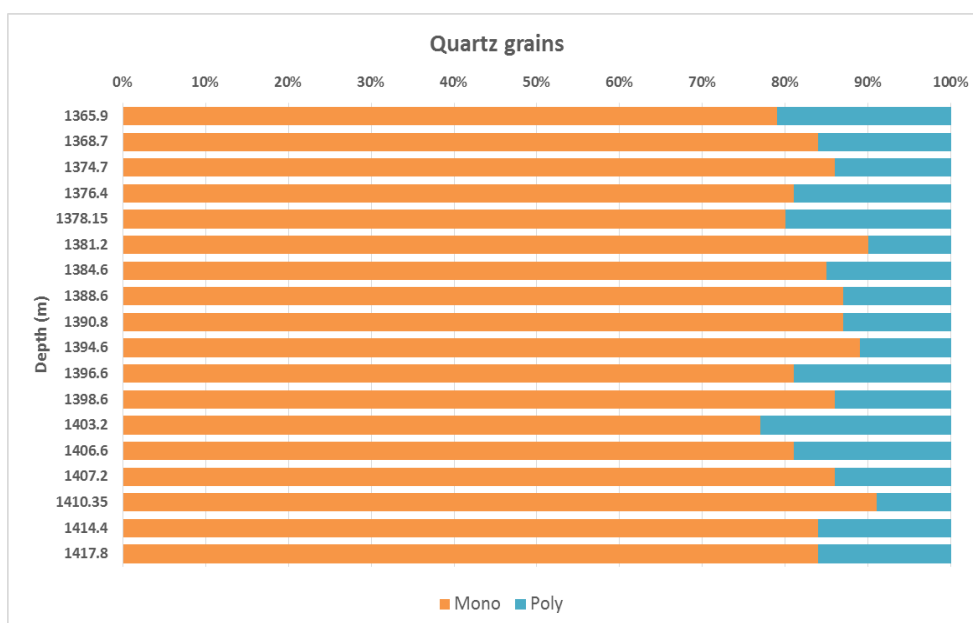


Figure 44: Distribution with depth of the monocrystalline and polycrystalline quartz grains from the point counting.

Feldspar:

The two types of feldspar, potassic and plagioclase feldspars were observed in all the samples of the core 7226/2-1. The proportion of plagioclases is higher with an average value of 64% of the feldspar content, with the lowest value being 41% and the highest 84% (Fig.43). The potassic feldspars, represented by microcline, are then in minority and present all the degrees of dissolution from 1 (very onset of dissolution) to 5 (dissolution almost total). The most present degree is the 3rd followed by the 4th closely (Fig.45). The first degree of dissolution is the least represented. For the plagioclase feldspar, the first degree of dissolution was not observed and the grains were mostly represented by 4-5 degree of dissolution (Fig. 45). In term of mineralogy, all the potassic feldspars were microclines whereas the plagioclases show more variability with a majority of albite but also some orthoclase and anorthite. Some advanced sign of albitization were observed associated with the presence of perthite. An interval of more altered feldspars is present between the samples 1384,6 m and 1394,6m depth (included) (Fig.45).

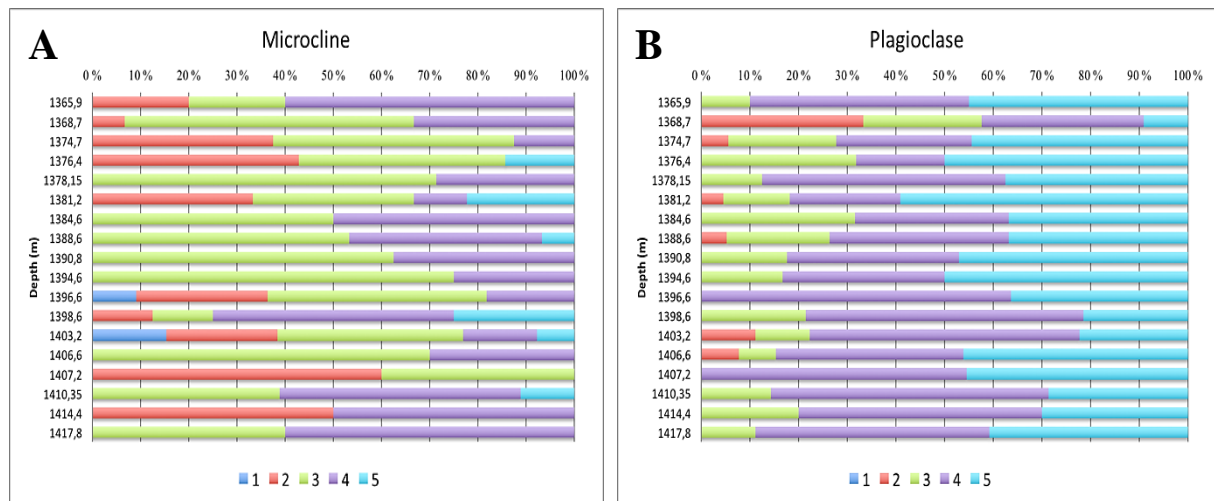


Figure 45: Distribution of the weathering degree of the feldspars with depth in the well 7226/2-1. A) Weathering degree distribution of the K-feldspar identified thanks to the crosshatched crystal twinning of the microcline. B) Distribution of the weathering degree for the plagioclases, identified with the polysynthetic twinning.

Rock fragments:

In the well 7226/2-1 rock fragments are the second largest component of the framework. The proportions of each category are presented in Figure 46. They display a high proportion of altered grains ranging from 3 to 60 % of the total amount of rock fragments, with an average of 31% (Fig.46). Most the fragments are chert fragments with an average of 47% composed of 28% of “fresh ones” and 19% of altered ones. The second type of rock fragments present is the lithic fragments, where the assemblage is composed of different minerals. This type is severely touched by dissolution with a percentage of altered clasts up to 12% in average for a total of 32, 2% of the rock fragment content. Some of those fragments got separated after dissolution and compaction making them counted as single grains affecting the IGV calculations and estimation of the sorting. This contributes to lower the percentage of lithic fragments in the core. Schistose fragments are the third most present type of rock fragments but are not observed in all the samples. Indeed, in six on the eighteen studied samples no schistose fragments were observed (Fig.46). Shale fragments have also been observed with a proportion in average of 8% but, as schistose fragments, they were not observed in all the samples (Fig.46). Their recognition can be difficult due to the presence of infilling clays and replacing grain clays in some layers.

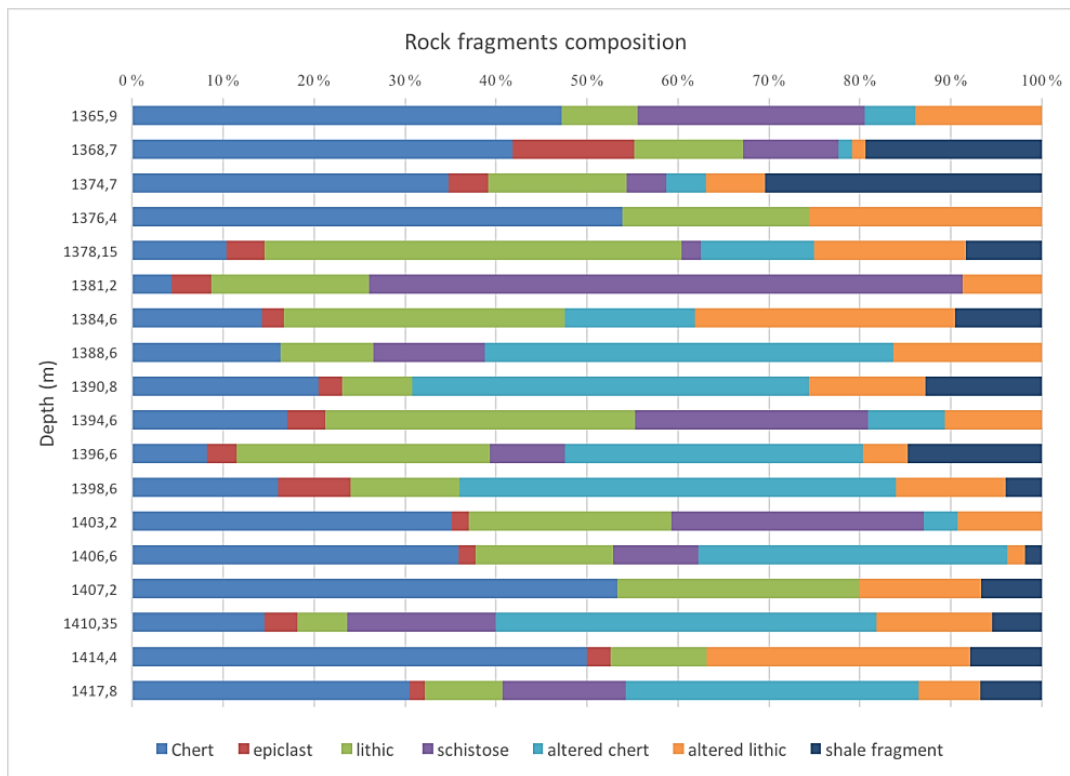


Figure 46: Distribution of the type of rock fragments with depth from the point counting. The identification is difficult due to the high degree of weathering of the fragments. Nevertheless 7 categories could be identified; among them 2 are altered classes.

Authigenic minerals :

Sphaerosiderites:

Siderite concretion or sphaerosiderites are present in the core from 1390m depth to 1418m depth (Fig.43). Their size increase down core and ranges from 60 μ m to 300 μ m. The biggest ones cover more area due to the apparent detachment of their external concentric layer. Their shape is more or less round even if some of them show a more wavy layering (Fig.47). These sphaerosiderites often appear as clusters and seem to have an etched outer surface (Fig. 47.D). The mineralogy shows a duality from the center to the outer layer (Fig.47). The center is enriched in Fe and Mn while the outer part is Mg rich. The transition between the two mineralogies is gradual with a decrease in Fe towards the external layer associated with an increase in Mg (Fig 47.A.B). They are associated with smaller, in average 5-10 μ m, rhombohedral siderite grains that seem to grow attached to the chlorite coating or on the outer layer of the sphaerosiderites (Fig. 47.C).

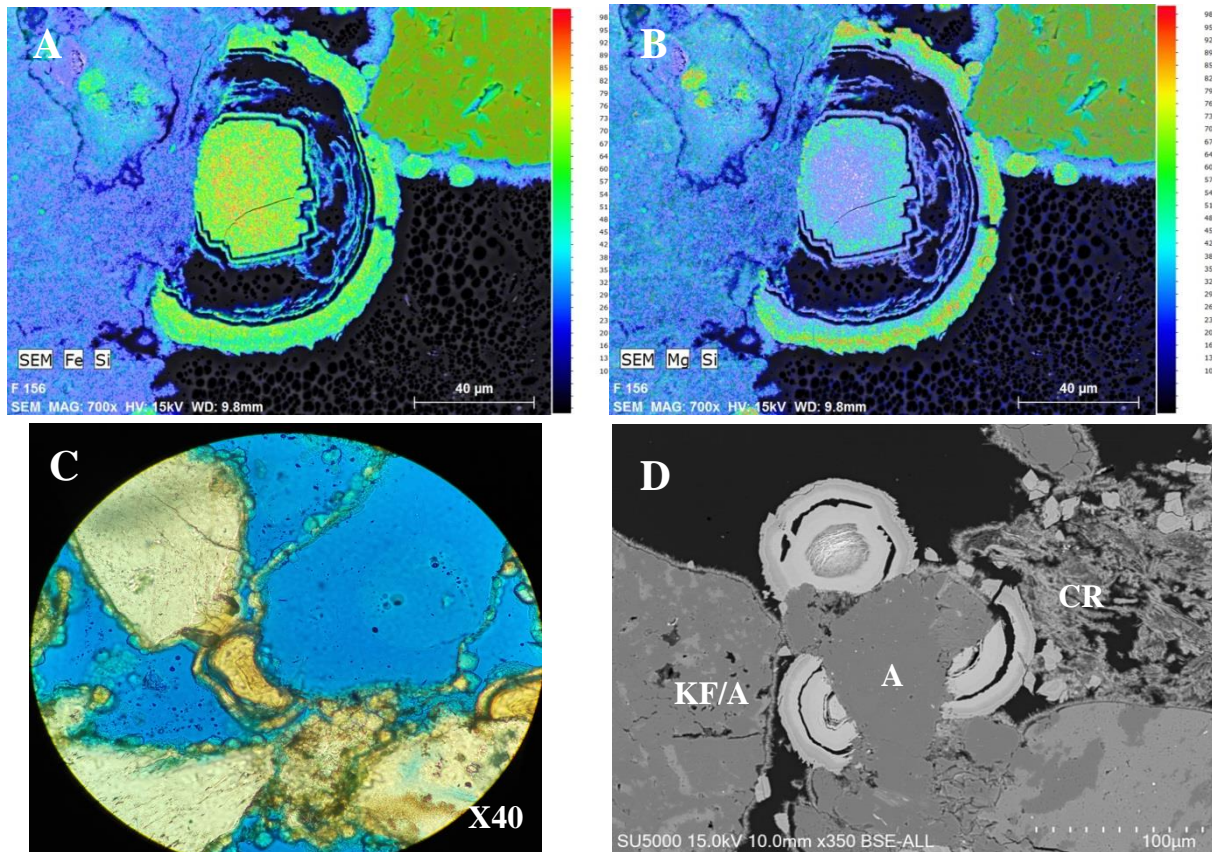


Figure 47: A) B) Fe and Mg distribution in the sphaerosiderites, the blue color corresponds to the lowest abundance and the red through the green represents higher abundances. A) Fe distribution and B) Mg distribution. C) Sphaerosiderites attached to the first layer of chlorite coating. D) Evidences of recrystallization of the sphaerosiderites in the sample 1414,40m depth of the well 7226/2-1 where **KF/A** is mixed K-feldspar and albite, **A** is albite and **CR** is chlorite rims.

Clay minerals:

Chlorite:

Chlorite is the most abundant clay mineral in the well 7226/2-1 (Fig.48). The most abundant is as pore filling and grain coatings. The pore filling chlorite can look like platelets of chlorite, as well as isopachous double chlorite rims but also as a mesh of chlorite or thick furry deposits (Fig.49). Chlorite is also present as pseudomorphic replacement of unstable grains that is visible as veins in the grains, as part on the side of the grain but also as the full grain (Fig.49). Chlorite coatings are present in large amount on the well 7226/2-1. The coating is fairly thick with a minimum of 3µm and a maximum measured at 10µm and an average at 8µm. The chlorite coating is composed of two types of chlorite. The underlying coat is made of small heterogeneous chlorite crystals of a more diffuse appearance and orientated tangentially to the grains. Above this layer, another layer is made of more

homogenous thin and elongated spiky crystals, called here pore filling platelets orientated perpendicular to the grain surfaces. Those crystals observed in the SEM how a higher content in Fe. The second layer is absent at the grain to grain contact where only the remnant lower coat is observed. The chlorite coating is usually thick and continuous.

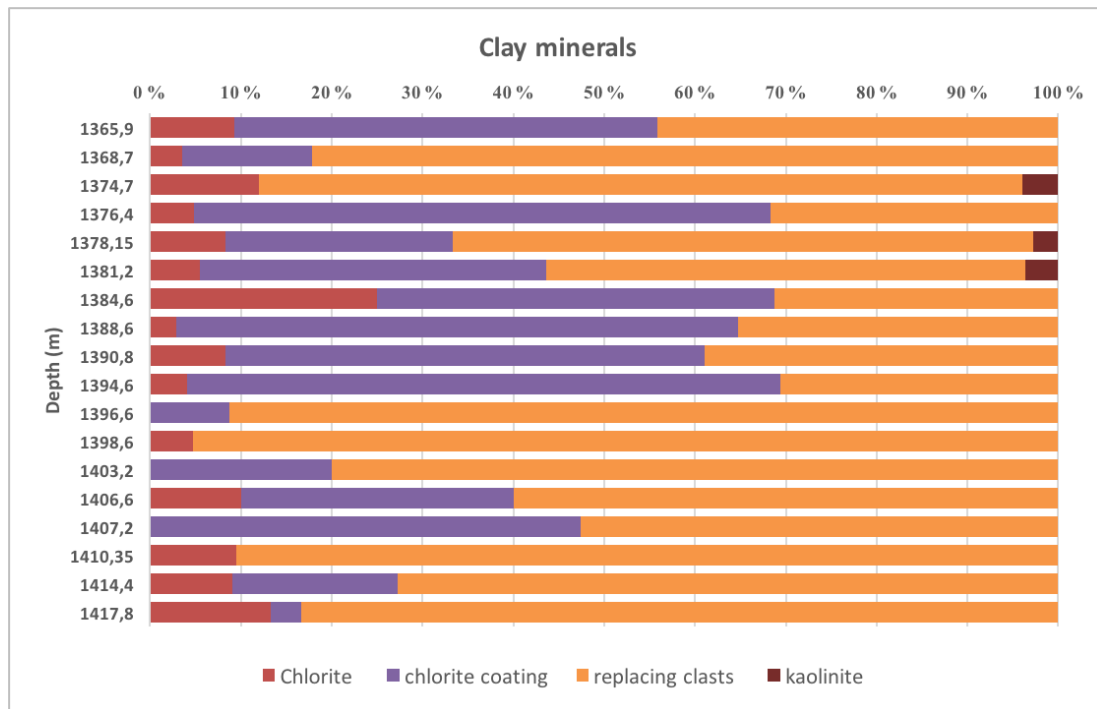


Figure 48: Distribution with depth of the clay minerals from the point counting in the well 7226/2-1. The point counting does not allow to give an exact composition of the clay minerals. Only chlorite, chlorite coating and kaolinite due to their characteristic mode of appearance could be identified. The other clay minerals have been identified using the clay fraction XRD and the SEM.

Kaolinite:

Kaolinite is the second most abundant clay mineral and occurs as clusters (Fig.50). Kaolinite is present in small proportion throughout the core but mostly on the top of the core where it reached up to 4% of the rock volume (Fig.43). Kaolinite occurs as clusters with its traditional vermiform structure (Fig.50). The grains tend to be bulkier in some samples showing a possible transition to dickite. Kaolinite is then occurring mostly in the pore space near dissolved minerals but has also been observed behind the chlorite coating as grain replacement where the crystals tend to be smaller than the ones in the pore space (Fig.50).

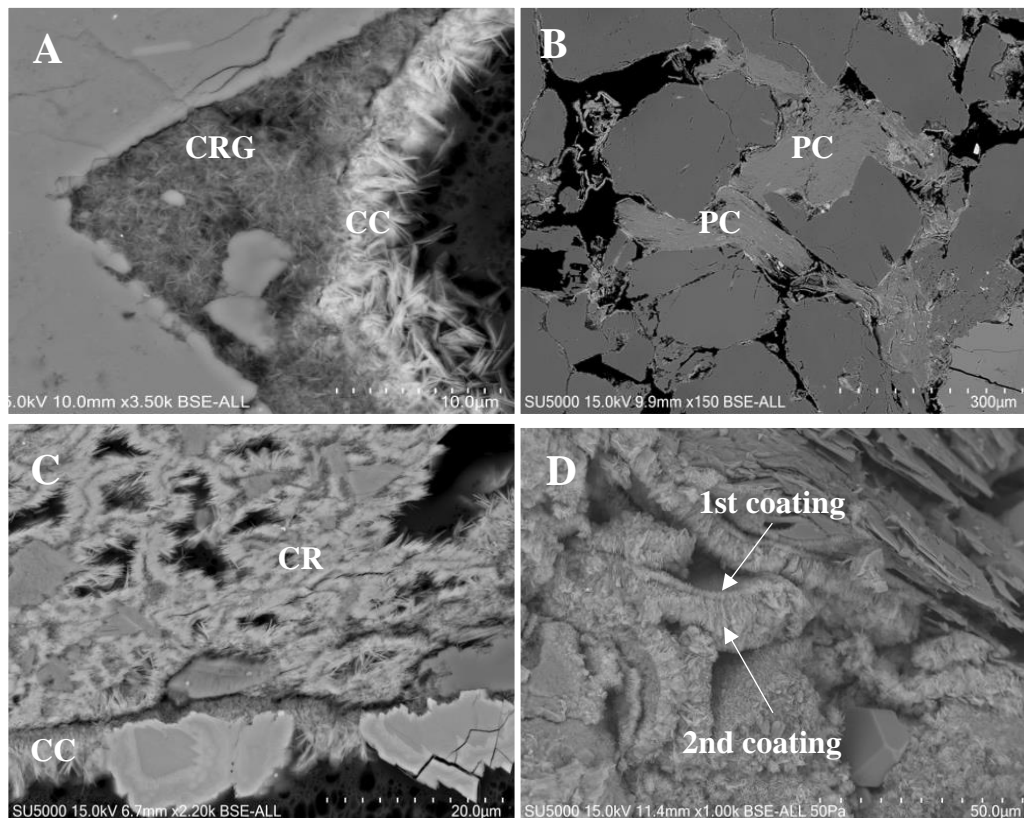


Figure 49: Mode of occurrences of chlorite in the well 7226/2-1 observed with the SEM. A) Replacing chlorite on a K feldspar grain and chlorite coating. B) Pseudomorphous chlorite filling the pore space. C) Rims of chlorite filling the pore space. To notice the rhombohedral siderite cement nuclei attached to the chlorite. D) chlorite coating and chlorite platelets observed with the SEM. With **CRG** for chlorite replacing grain, **CC** for chlorite coating, **PC** for pseudomatrix chlorite and **CR** for chlorite rims.

Illite

Illite is present throughout the core ranging from 0,9 to 3,3% of the rock volume with an average at 1,9%, except at 1390m depth where no illite was found (Fig.43). These proportions are calculated using the bulk XRD data. No illite crystals were observed using neither the polarized microscopy nor the SEM under its needle form but were observed as chaotic and crumbly assemblages.

Calcite:

Calcite is present as cement in four samples in the well (Fig.43). Small portion of this cement is composed by magnesium rich calcite for a maximum of 5,4% found at 1396, 60 m depth (Fig.43). Calcite is also present as grains in three other samples located in the upper part of the core where they often occur within spread mica grains surrounded by pseudomorphous chlorite.

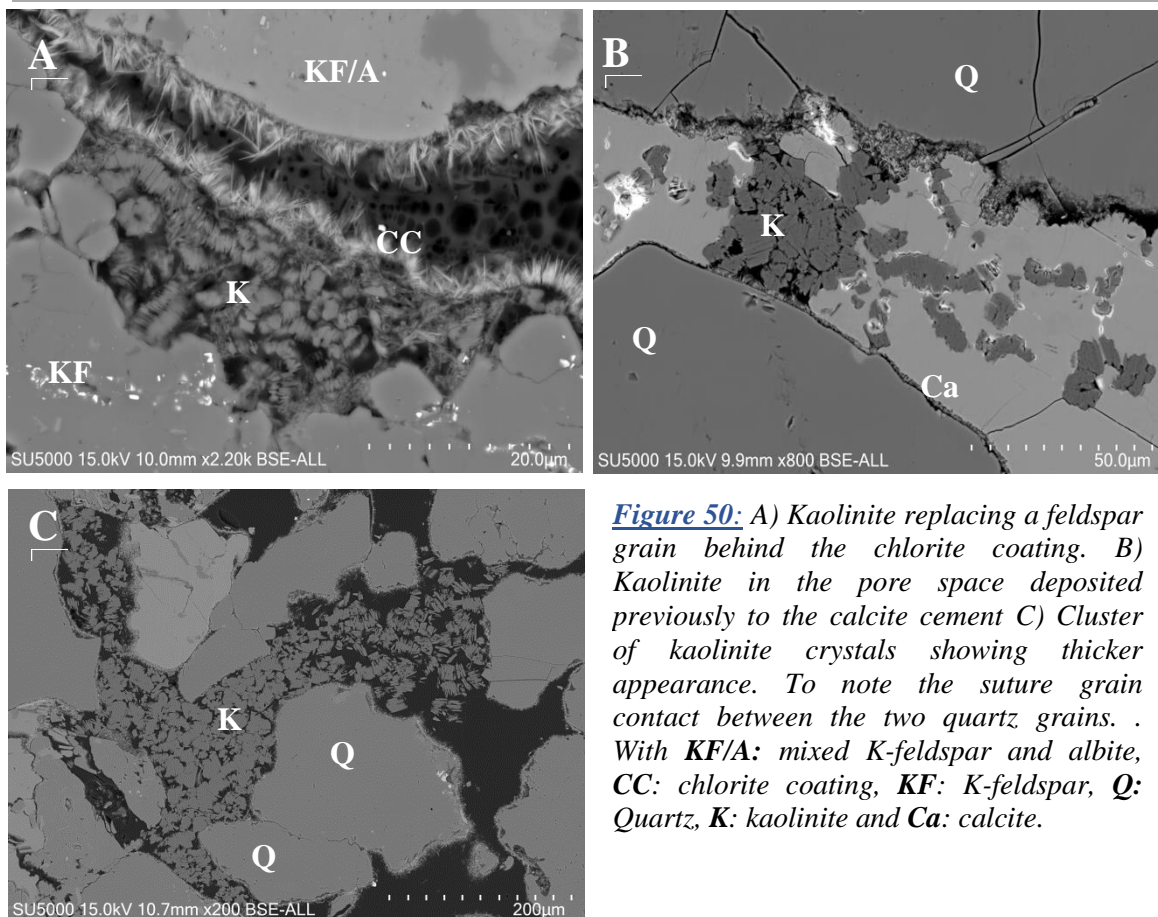


Figure 50: A) Kaolinite replacing a feldspar grain behind the chlorite coating. B) Kaolinite in the pore space deposited previously to the calcite cement C) Cluster of kaolinite crystals showing thicker appearance. To note the suture grain contact between the two quartz grains. . With **KF/A**: mixed K-feldspar and albite, **CC**: chlorite coating, **KF**: K-feldspar, **Q**: Quartz, **K**: kaolinite and **Ca**: calcite.

Quartz cement:

Quartz cement is only present in small amount in the well 7226/2-1 averaging at 0,43% of the total rock volume (maximum 2,5 %). A clear zone of greater quartz cementation is visible between 1376,40m and 1396,60m depth (Fig 51). When the grains are coated by chlorite, quartz cement onsets develop around this coating when this one is incomplete (Fig.51). No quartz cement was observed from 1396 to 1414m depth where most of sphaerosiderites were found.

Porosity and compaction :

Porosity and permeability:

The porosity trend in the core 7226/2-1 can be divided into two zones (Fig 52). In the upper part of the core (1365-1390m depth) the porosity is fairly constant around 12% in average. A transition can be observed at 1390m depth, after this point the porosity becomes irregular and drops under 2% due to the present of heavily calcite cemented samples. Despite those cemented layers; the porosity is still reduced down core to an average of 6% (Fig.52). This reduction is linked with the presence of siderite.

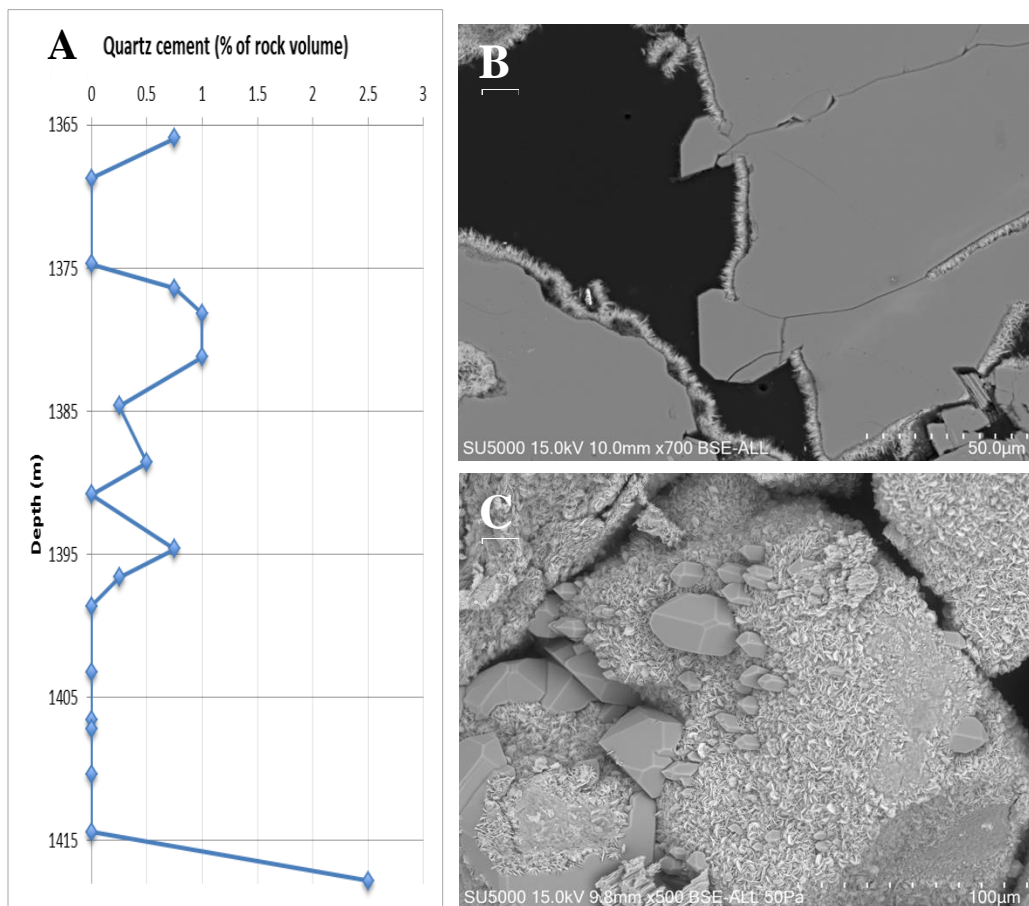


Figure 51: A) quartz cement abundance with depth in the well 7226/2-1, expressed as percentage of the rock volume. The intervals of values zero correspond to calcite or siderite cemented intervals. B) C) Quartz overgrowth observed in the SEM. To see the incomplete chlorite coating allowing more quartz cementation. CC: chlorite coating, Q: Quartz.

The largest part of the porosity is contained in the pore space but a small amount is also contained as secondary porosity in dissolved grains. The location of some of the dissolved grains is still visible thanks to the left-over chlorite coating. The permeability is comprised between 0,02 and 43,2mD and averages around 17mD (Fig 52). The permeability values have been calculated using the water saturation from the neutron porosity log and might be not accurate. Nevertheless, it gives an estimation of its fluctuation throughout the core. Two zones in the permeability distribution can be observed separated by a sharp peak at 1392-1393m depth. This peak can't be related to any sedimentary features due to the lack of sample in this interval. The upper part of the core until 1394m depth shows a fairly constant permeability averaging at 24mD it is cut by a decrease at 1374,7m depth by a cemented interval reducing the permeability close to zero. The second zone is the lower part of the core between 1394 and 1418m depth. The permeability averages at 22% (Fig. 52). This interval is corresponding to sphaerosiderites rich interval. This section is also cut by low permeability calcite cemented intervals.

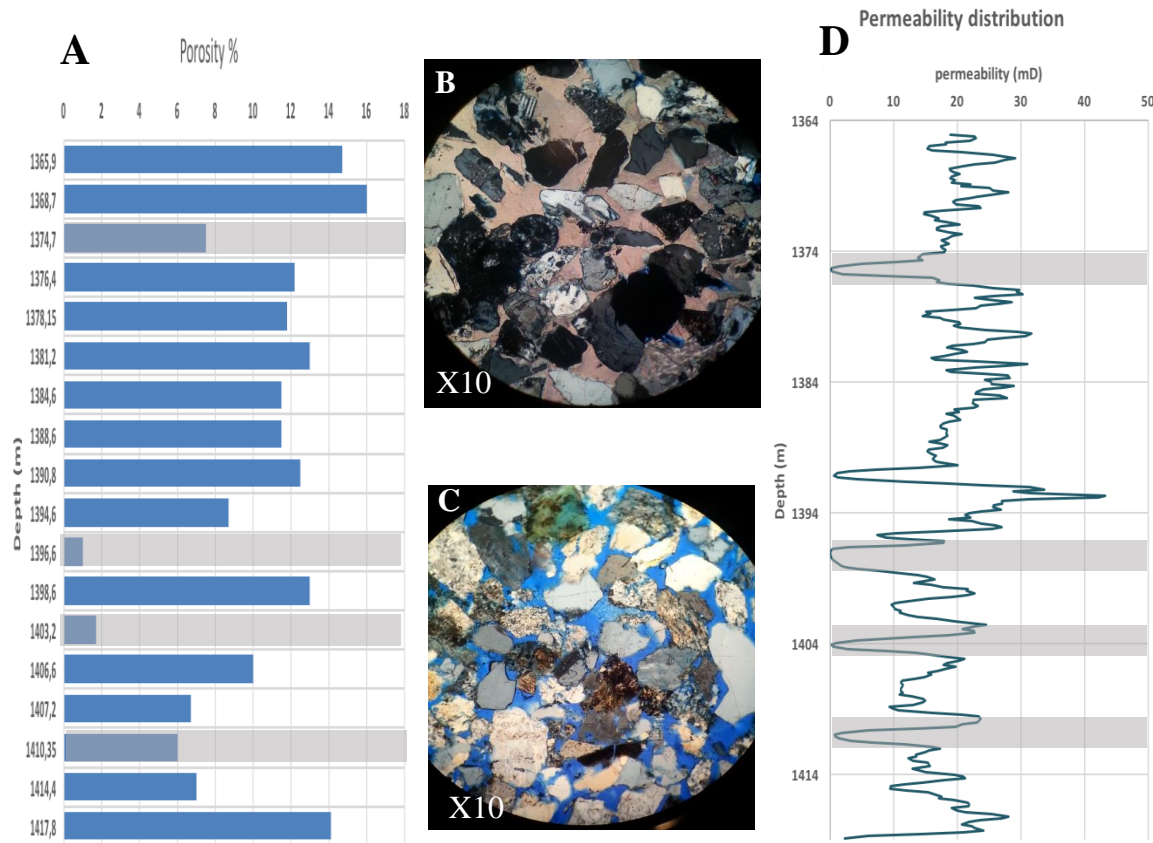


Figure 52: A) Porosity (%) distribution in the well 7226/2-1 from the point counting. The grey intervals on the graphs represent cemented interval of calcite. B) Typical cemented interval for the well 7226/2-1. C) Typical non-cemented interval for the well 7226/2-1. D) Permeability distribution in the well 7226/2-1.

Grain contact:

Most of the grain contact type is point contact followed closely by long contact (Fig 53). Some of the layers, mostly down core show a greatest proportion of compacted grains up to 60% of the contacts for the sample 1414,40m due to their large sizes (Fig.53). This value must be taken as estimation because of the great dissolution of grains associated with the matrix grains which makes the grain contact hard to establish.

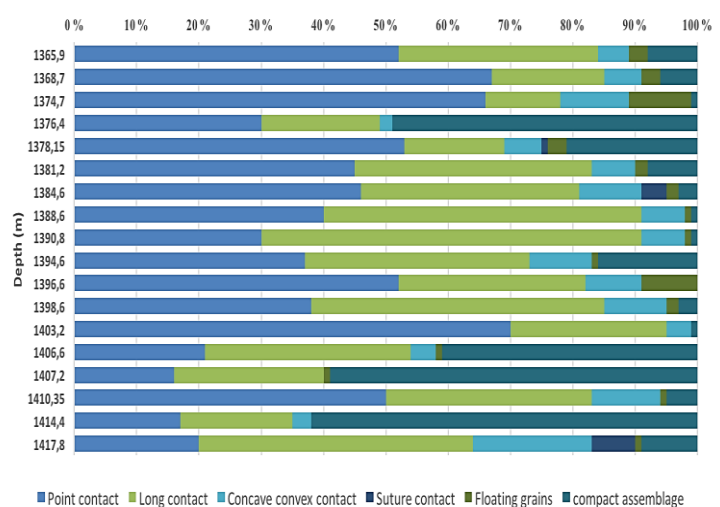


Figure 53: The grain contact distribution was evaluated trough depth. The compacted class corresponds to a grain surrounded on every side by other grains.

Intergranular volume:

The IGV is ranging from 21% to 47% and averages at 33% (Fig.55). The highest values are found in the cemented intervals. To calculate the IGV, all cements are taken in account. In this study the cement content is represented by calcite, quartz and siderite cement (both sphaerosiderites and rhombohedral) but also by the products of the diagenetic reactions filling the pore space such as kaolinite and chlorite coating. This large range of IGV values makes it necessary to treat the samples by categories to estimate the loss due to compactional regime. The studied samples have been divided into 3 categories (Fig.54): pure sandstones (A), calcite cemented samples (B) and siderite cemented samples (C).

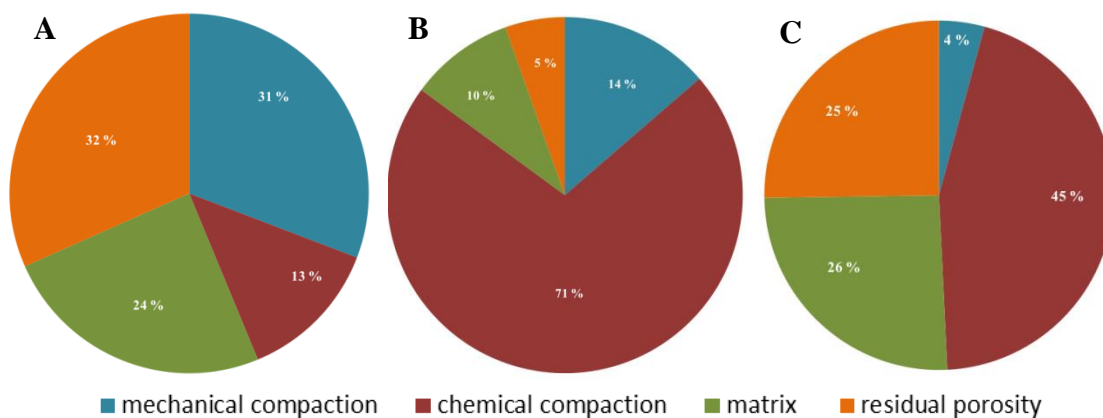


Figure 54: Percentages of the compaction regimes and depositional matrix in the porosity loss of the original porosity. The original porosity is defined as 40% for well-sorted fine grained sandstones (Beard & Weyl, 1973). The percentages are displayed for the 3 categories of deposits observed in the well 7226/2-1. A) Pure sandstones or non-cemented deposits. B) Calcite cemented deposits. C) Siderite-cemented deposits. The siderite cement is composed of the sphaerosiderites as well as the rhombohedral cement.

The IGV in the pure sandstones interval is averaging at 27% (Fig.55). The porosity loss due to mechanical compaction is averaging at 31% whereas the chemical compaction (cement) is responsible for the loss of only 13% of the initial pore space. The loss due to matrix content is averaging at 24 %, and the residual porosity is estimated at 32% of the initial pore space in average (Fig.54). The initial porosity was defined as 40%, value given by Beard & Weyl (1973) for fine grained- well sorted sandstones.

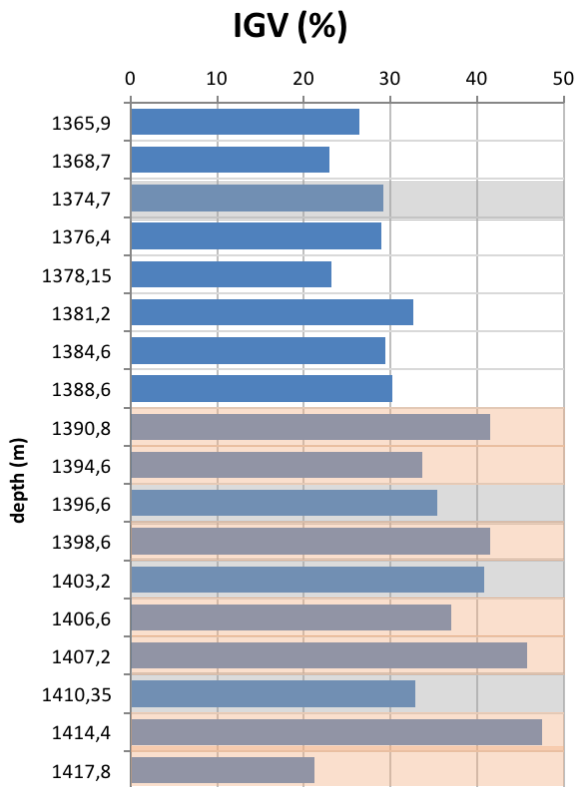


Figure 55: Reconstructed Intergranular Volume from the point counting analysis for the well 7226/2-1. The grey intervals are the calcite cemented ones. The orange intervals indicate the intervals of siderite cementation.

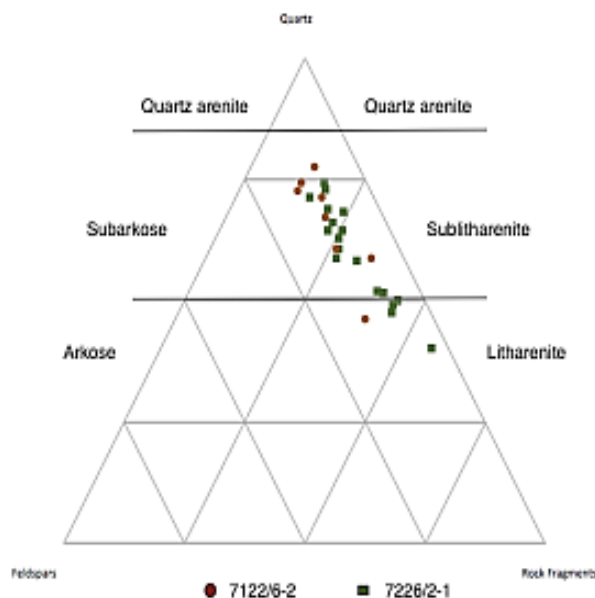


Figure 56: Plot of the point counting analyzed samples for both wells following the classification of sandstones from Folks (1974).

The IGV of the calcite cemented intervals is higher and averages at 35% (Fig.55). The porosity loss is mainly due to chemical compaction and is averaging at 71% of the original pore space (Fig.54). The mechanical compaction takes the second place as porosity reduction process with an average loss of 14% of the initial porosity (Fig.54). The matrix content is lower than in the previous intervals and its role in porosity reduction is estimated as 10% of the initial pore space in average. The residual porosity is much lower than in the pure sandstones intervals and averages at 5% of the original porosity (Fig.54).

The siderite cemented intervals are the middle position of the other categories and their IGV averages at 38% (Fig.55). The porosity loss due to mechanical compaction is averaging at 4,2% whereas the chemical compaction is responsible for the loss of 45 % of the initial pore space (Fig.54). The highest matrix content is found in those intervals and is responsible for 26% of the initial porosity loss. The residual porosity is estimated at 25% of the initial porosity (Fig.54).

Sandstones classification:

When plotted in the Folk's sandstones classification both samples are in the same categories: sublitharenites (Fig.56)

with the well 7122/6-2 reaching the limit to litharenite class. The classification of the samples for the well 7122/6-2 are not representative of the whole section since only few samples could be analysed during the point counting. Most of the samples of the well 7122/6-2 are considered as lithic greywackes (>15% matrix).

5.3 Petrophysical analysis :

5.3.1 Compaction trend:

The aim when studying the well logs was to understand the compactional regimes and the burial- temperature history of the cored section. The temperature and degree of compaction are important factors for the reservoir quality assessment since they have control on the diagenetic processes affecting the porosity and permeability.

The increase in compaction trough depth is registered in the sonic and bulk density log. The transition zone between the two compaction regimes is well visible expressed by a kick in velocity and density.

5.3.2 Gamma log and formations:

Most of the groups (Fig.57) are present in the two wells starting by the Sassendalen Group from the Early to Middle Triassic dominated by shales and siltstones. This group is followed by the Kapp Toscana Group, Late Triassic to Early Jurassic, composed by shales, siltstones and sandstones. Shales and sandstones are the dominating lithologies. After the Kapp Toscana Group, the Late Jurassic- Early Cretaceous Adventdalen Group is reached composed by dominating marine mudstones and shelf sandstones showing important hydrocarbon sources.

The well 7122/6-2 differs from the well 7226/2-1 by having two extra groups (Fig.57), the Nygrunnen Group and Sotbakken Group. The next common group reached is the Norland group from Middle-Late Pleistocene to recent composed mostly by marine claystone. The gamma logs are gathered by formations from the Early to Middle Triassic to recent and presented in Figure 58.

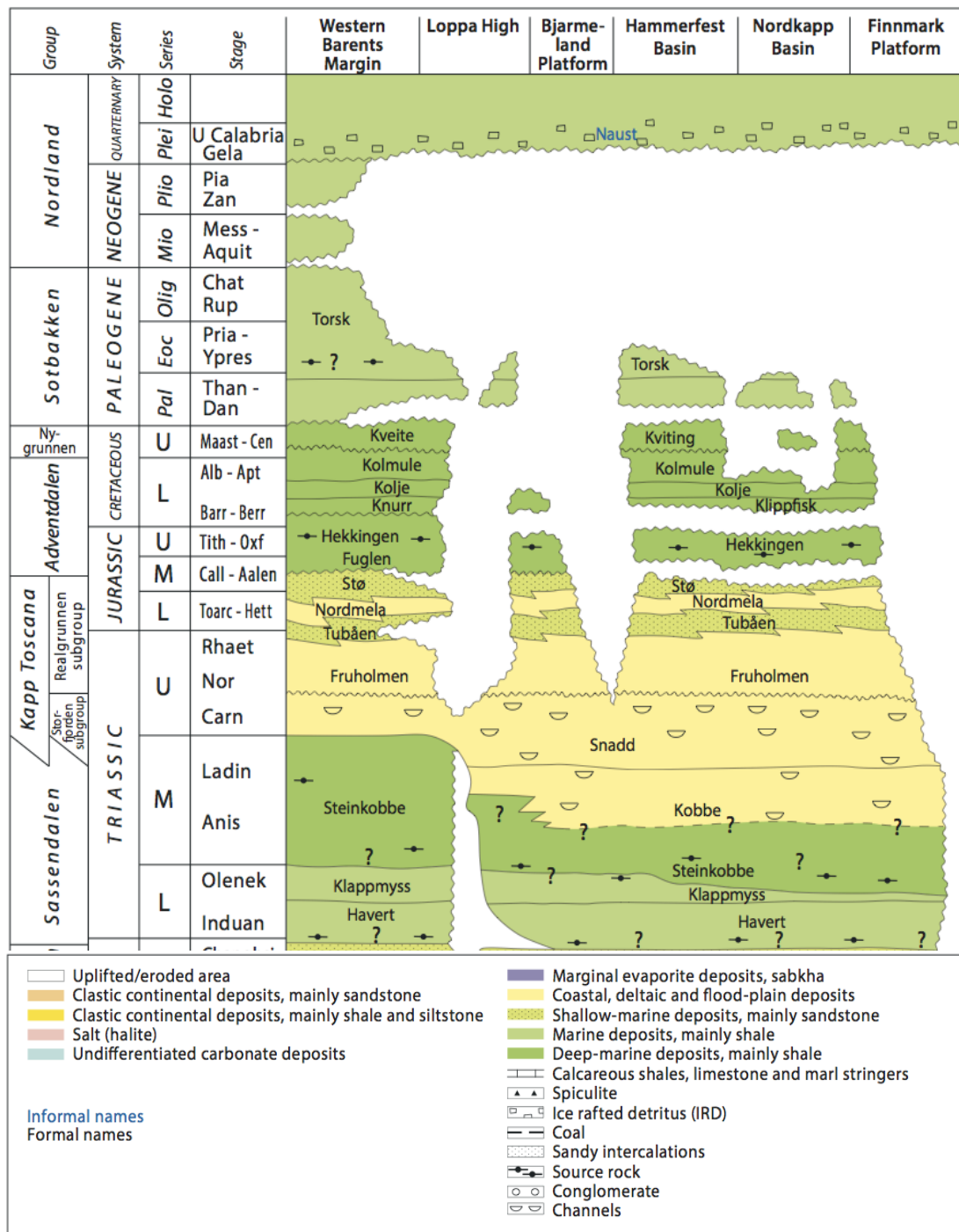


Figure 57: Chronostratigraphic chart of the groups and formations in the Barents Sea for its different structural elements from npd.no. To note that for the Bjarmeland platform and Hammerfest basin the development is constant and equilibrated until the Snadd Formation but get differentiated during the Upper Triassic.

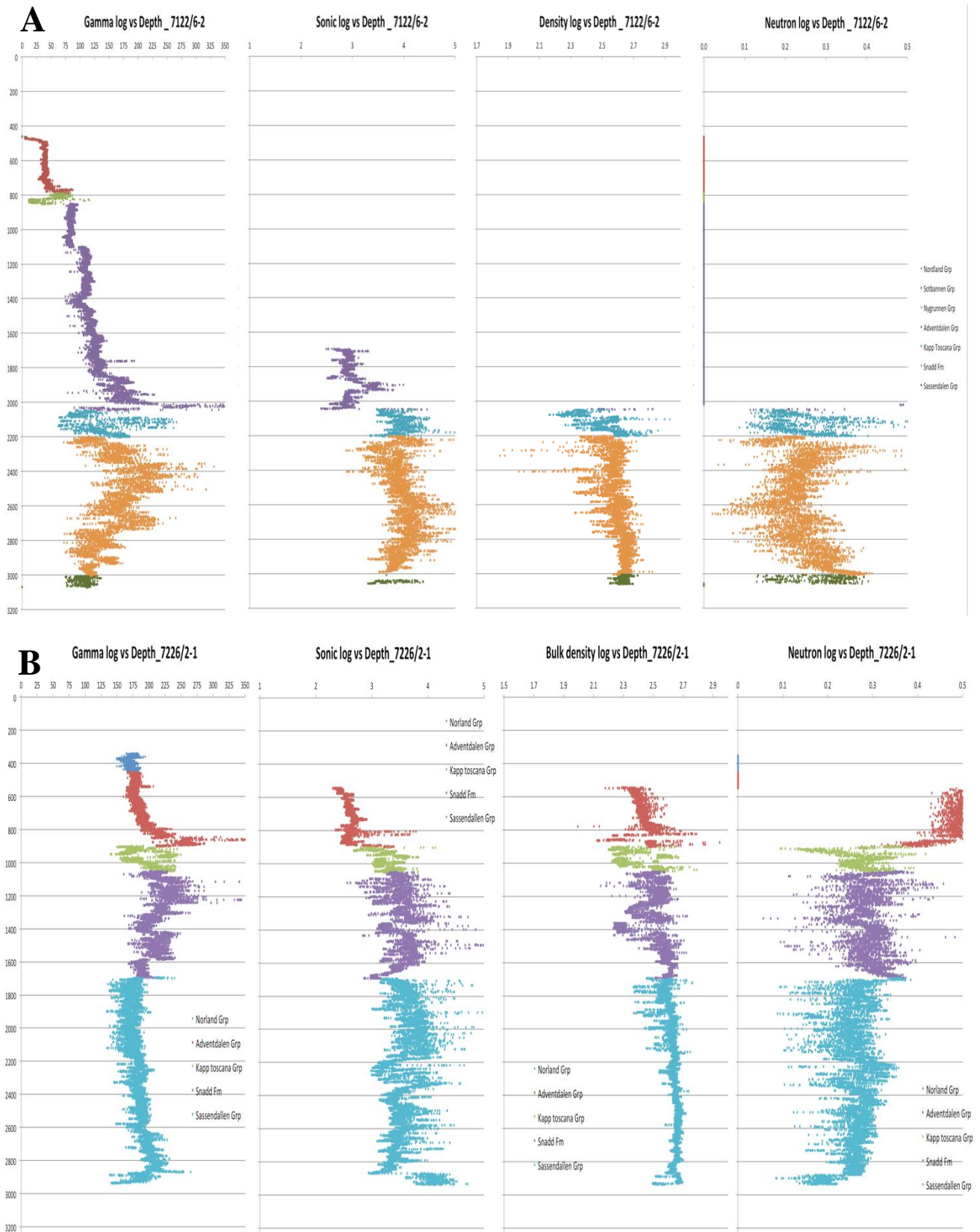


Figure 58: Combined well logs data for the well 7122/6-2 presented in A) and 7226/2-1 presented in B). The gamma log is in the first of each row followed by the sonic log, bulk density log and neutron porosity log. Each log is separated by groups or Formation which owns different colors.

The gamma log response shows values located between 130 and 250 API for the well 7122/6-2 (Fig 59). Those values place the section in the pure shale interval, above 125 API. Nevertheless, the sedimentological analysis reveals that the section owns many sand packages. An explanation for this is the amount of organic matter and potassium rich deposits that could lead the higher values. The gamma values show an up and down type of sequence showing the heterogeneity of the deposits and the presence of carbonate layers. These large heterogeneities make the identification of possible trend difficult. The lower core (2452-2506 m) shows a different trend upwards of lower values, showing a shallowing in the section, also observed in the sedimentological analysis. The middle part of the core (2570-2482 m) shows the greatest heterogeneity without any specific trend. The upper part of the core (2452-2470 m) presents a slight decrease upwards in the gamma ray values indicating once again a shallowing in the conditions, also observed in the sedimentological analysis.

The gamma log response for the well 7226/2-1 shows similar values as in the well 7122/6-2, 190-210 API, but with fewer variations (Fig 59). The first zone is the lower part of the core (1395-1415 m) with stable gamma log values averaging around 180 API. The second zone located above (1376-1395 m) has a decrease in gamma values indicating an increase in sand content. The third zone (1370-1376 m) is an increase in gamma values indicating an increase in mud content. The last zone located at the top of the core (1365-1370 m) is very similar to the first one with stable gamma values but those ones are higher than the first ones indicating a general increase of the mud content through the core. This trend was observed also in the sedimentological analysis. The observation of the studied section within the evolution of the Snadd Formation from the gamma ray curve, a clear bell shape can be identified (Fig.60). This bell shape or dirtying-up trend is underlain and overlain by higher gamma ray values deposits. Inside this fining-dirtying upwards unit two smaller bell shapes in the gamma ray curve could be observed (Fig.60). The first bell shape (1380-1418m depth) may be composed of two bell shapes with one from 1380-1395m depth and another one from 1395-1418m depth (Fig.60). The presence of a carbonate layer at 1495m depth makes this observation difficult to make.

5.3.3 Sonic log:

The sonic log was mostly used to identify the compactional regimes in the two wells (Fig.58). The sonic log was also used to estimate the uplift that occurred in both wells,

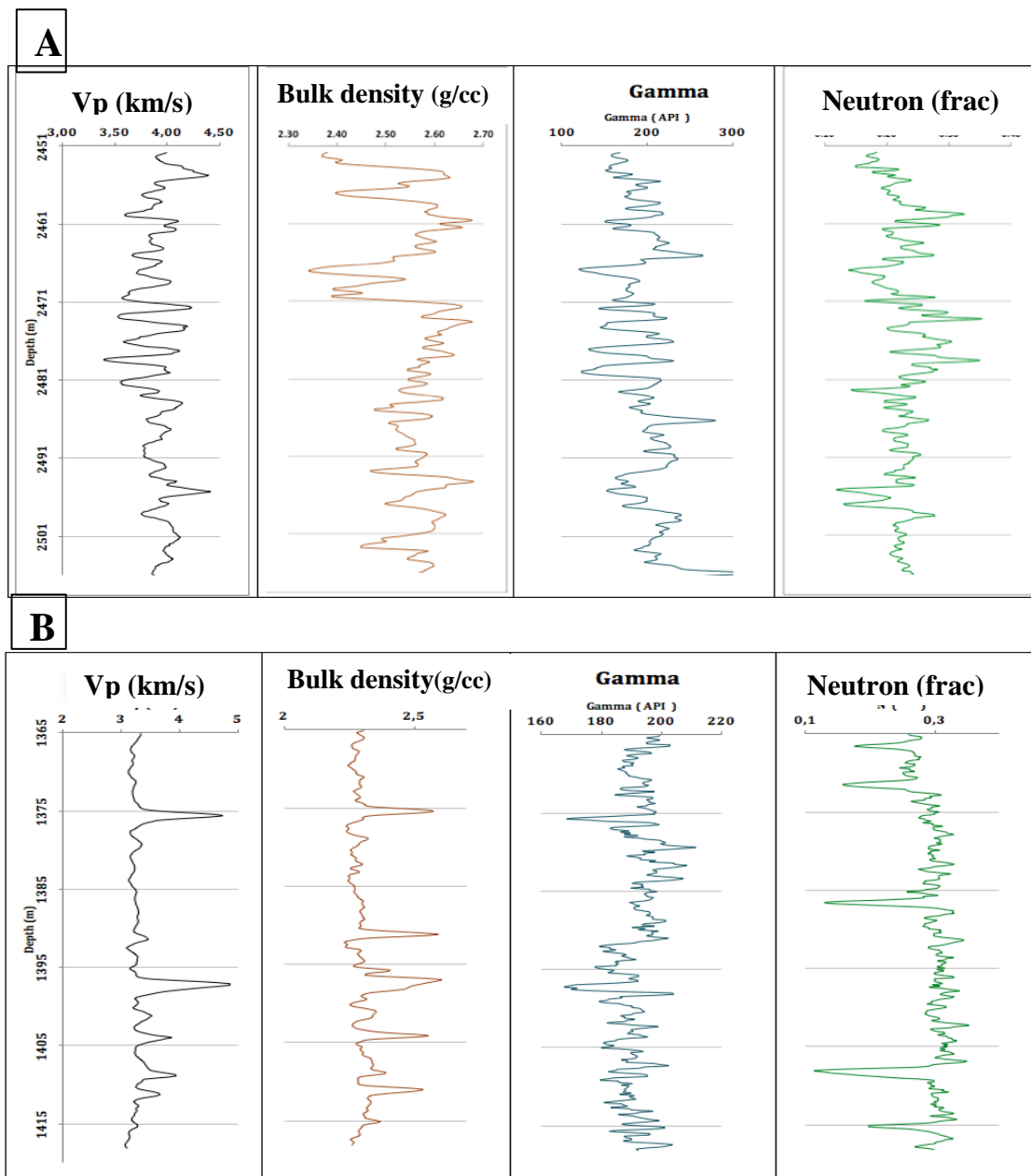


Figure 59: Combined well logs for the Snadd Formation in each well. The well 7122/6-2 is presented in A) and the well 7226/2-1 is presented in B). To note that the scale is different for both wells.

described in details further below. On the close up on the logged sections in Figure 59, the most chaotic zone observed between 2471 and 2481m depth is the zone of most abundance of dolomite. The dolomitic and cemented layers are much spread and will show a higher velocity than the shale or sandstones. The rise in the Vp values observed in the lower part of the core (2481-2506 m) corresponds to an increase in quartz cement strengthening the rock.

The close-up sonic log of the logged intervals of the well 7226/2-1 reveals very stable values corresponding to the regular deposits of sandstones. Some kicks in the Vp can be observed and corresponds to the cemented intervals (Fig.59).

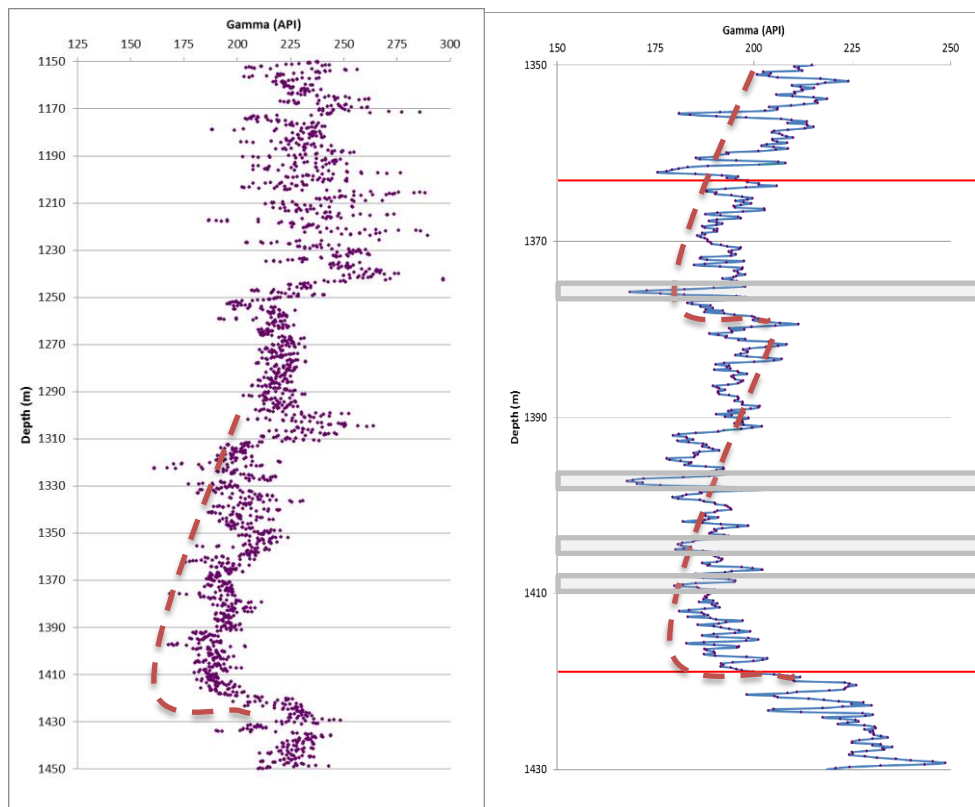


Figure 60: A) Bell shape (red dotted line) of the gamma ray values for the studied interval (1365-1418m). B) Smaller bell shapes observed within the studied sequences. The grey intervals represent calcite cemented intervals. The red lines define the studied interval. The first bell shape (1380-1418m depth) may be composed of 2 bell shapes with one from 1380-1395m depth and another one from 1395-1418m depth. The presence of a carbonate layer at 1495m depth makes this interpretation difficult to make. The red lines limit the studied section.

5.3.4 Density log:

As with the gamma log, the density log can help to discriminate different lithologies, as well as some diagenetic products such as quartz cement. The logged section of the well 7122/6-2 in Figure 59 shows great heterogeneities but as in the sonic log the dolomitic intervals can be identified by the highest density values. An abnormally low values interval can be observed between 2467m and 2471m depth corresponding to a sand rich interval.

The logged section of the well 7226/2-1 shows very stable values around $2,3 \text{ g/cm}^3$. This stability is broken at some places by peaks up to $2,55 \text{ g/cm}^3$ corresponding to the calcite cemented intervals.

5.3.5 Neutron log:

The neutron log is used as a porosity indicator (Fig 59). The neutron tool is sensitive to the amount of hydrogen in the formations and this way to the fluid content. In rocks, hydrogen can be present in the matrix as well as in the pore fluid. Due to this, the values had been corrected. Nevertheless, the neutron log will show higher porosity in shale layers since those ones contain water and hydrogen ions in their structures leading to overestimation of the hydrogen ions.

The association between the Neutron and the density log, the gas filled intervals can be identified clearly by a very distinct and large negative separation (Mondol, in Bjørlykke, 2015). In the well 7122/6-2 one negative separation was observed from 2960m to 3000m depth at the boundary between the Snadd and Kobbe formation, the latest one is known to contain gas.

In the well 7226/2-1 one negative separation was also observed at 1650-1750 m depth, in the very last meters of the Kobbe Formation close to the boundary with the Snadd. The neutron-density logs are displayed in the in appendix 3.

5.3.6 Porosity estimation :

To estimate the porosity, three different methods were used. The Figure 61 presents the results of the 3 methods in the well 7226/2-1. The first method used is the direct reading of the neutron porosity log curve. For the well 7226/2-1, the section presents a very high porosity in majority above 25%. The porosity from the Neutron log drops to 15% in the cemented intervals along the core. For the well 7122/6-2 the neutron log shows constant value alternating between 15-25% porosity, the maximum is reached in 3 intervals around 35% porosity (Fig.61).

The second method used is the estimation of the porosity based on thin sections analysis and the blue epoxy. This method gives lower porosity estimations than from the neutron log (Fig.61). For the well 7226/2-1 the trend is a constant porosity around 22% throughout the core. This trend is broken in 4 intervals where the porosity drops to 5%. Those intervals correspond to cemented intervals from the thin section analysis. The same trend is observed using the third method (Fig.61), the value found in the point counting, but the porosity is then reduced to 12% average and less than 3% minimum in the cemented intervals. For the

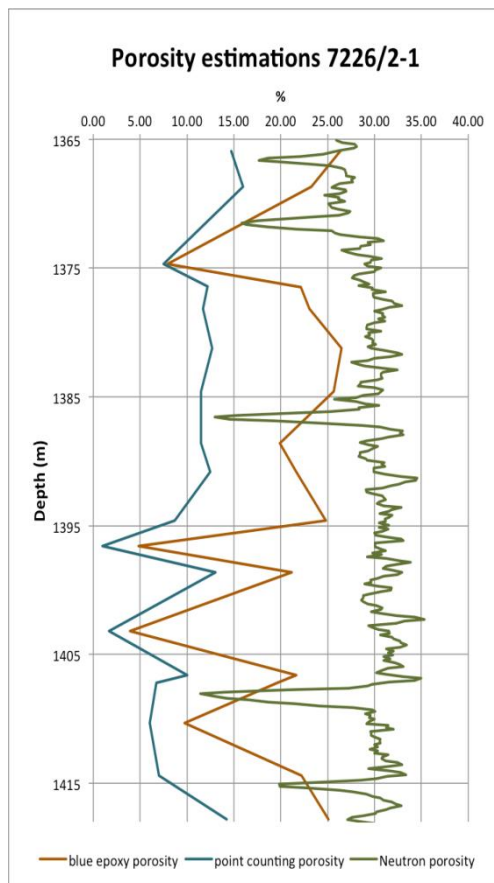


Figure 61: Curves of the three methods used to calculate the porosity of the samples for the well 7226/2-1. The blue one is the from the point counting and give the most realistic values. The green one from the neutron porosity gives very overestimated values.

well 7122/6-2, the trend for the second and third method is to increase at the very top and middle of the core (Fig.61). The blue epoxy reading gives higher porosity estimation than the point counting, respectively an average of 12% and 4% for the best intervals, and <1% and 1% for the worst intervals (Fig.61).

The porosity value chosen as the most accurate is the one given by the point counting. The neutron porosity being too affected by the hydrogen bounded in the mineral structures and the blue epoxy can cover some grains and pore filling minerals.

5.3.7 Uplift estimation:

The present day temperatures in the wells are not able to explain the presence and amount of authigenic minerals such as quartz cement observed in the petrographic study. This anomaly between what is expected at these temperatures and the observation made requires investigating on the total exhumation for each well.

The total exhumation is calculated based on the mechanical compaction observed in the sonic log compares to three experimental compaction curves: the 50:50 silt-kaolinite compaction curve from Mondol et al (2009), the compaction curve from the etive sand of Marcussen et al (2010), the mixed sand-mud compaction curve from Storvol et al (2006). To choose to which curve compare each well, a study of the gamma log was carried out in view to identify the mineral composition of the mechanical regime of the core.

The Figure 62 presents the sand/shale distribution for each well. For the uplift calculation, the well 7122/6-2 was compared to the interval between the mud and sand curves whereas the well 7226/2-1 was compared to the sand curve.

The calculated uplift values are presented in Figure 62, and is estimated as 1470m for the well 7122/6-2 and 1500m for the well 7226/2-1. The uplift estimation is used to calculate the maximum burial depth and this way get an estimation of the maximum burial temperature (table 7).

This temperature must have been higher than the calculated one because at the time of the burial, rifting events happened and resulted in a higher geothermal gradient compared to the actual. The highest temperature range is found in the well 7122/6-12 located in the Hammerfest basin with a temperature range for the Snadd Formation about **141°C to 143°C** whereas the Snadd Formation in the well 7226/2-1 on the Bjarmeland platform reached temperatures ranging between **99°C to 101°C**.

***Table 7:** Table gathering the uplift estimation values and associated burial temperatures based on the calculated geothermal gradient for each well.*

	7122/6-2	7226/2-1
Uplift estimation	1470m	1500m
Maximum burial depth pre-uplift Snadd Fm.	3976m	2918m
Calculated geothermal gradient	36°C/km	34°C/km
Actual temperature range	88 °C – 90 °C	46°C – 48°C
Pre-uplift temperature range	141°C – 143°C	99 °C – 101°C

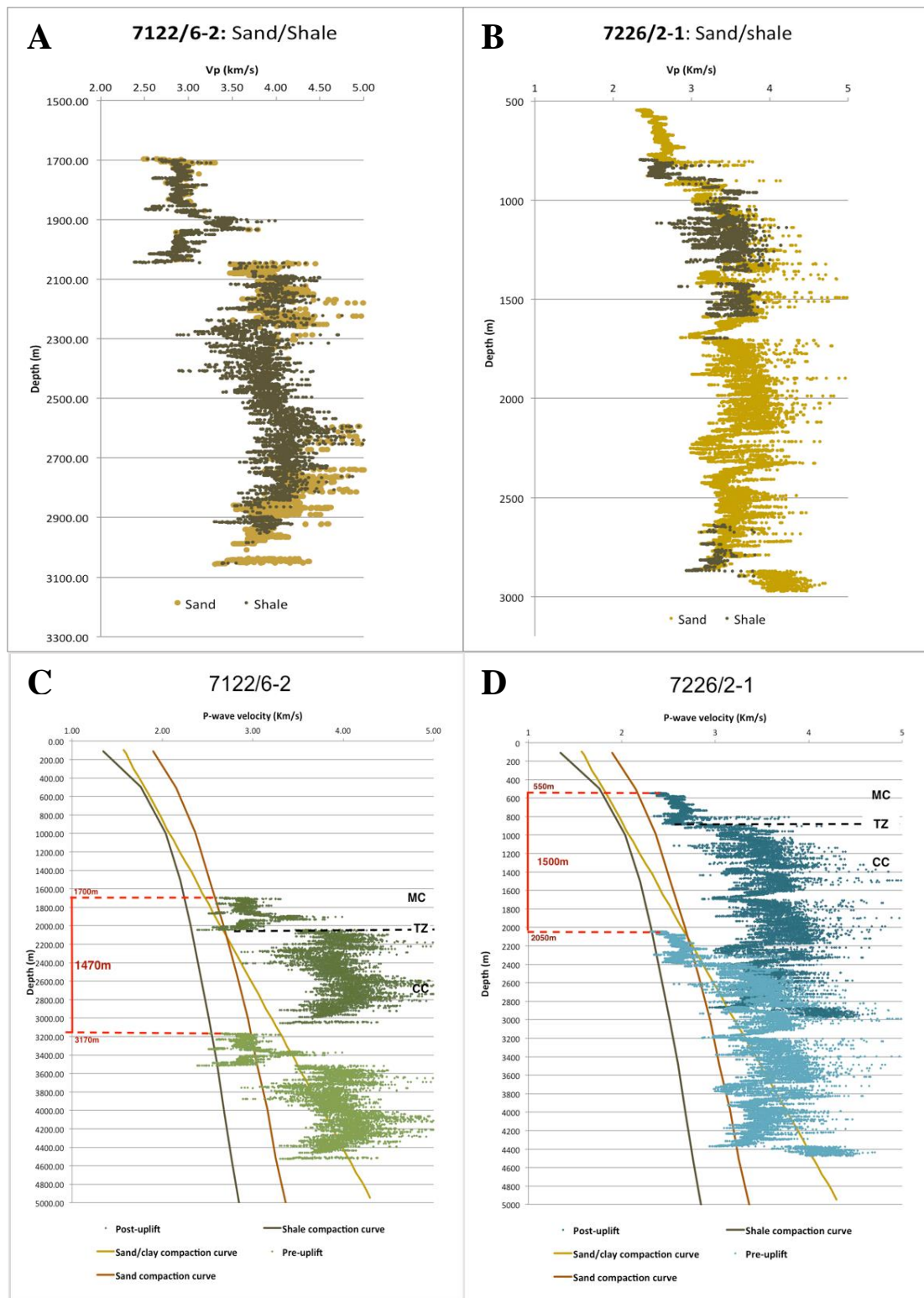


Figure 62: A) The sand (yellow) and shale (brown) proportion from the gamma log values for the well 7122/6-2. The main lithology is chosen for the reference curve for the uplift estimation in function of the proportion in the mechanical compaction zone (MC). B) Sand/ shale proportion from the gamma log values for the well 7226/2-1. C) D) Uplift estimation from the Vp values for the well 7122/6-2 in C) and the well 7226/2-1 in D). The compared curves are sand/clay from Storvol et al 2006. The shale curve is based on the 50:50 kaolinite/ silt from Mondol et al 2009 and the sand curve from Marcussen et al 2010. The red values represent the uplift estimation and the black the compaction zone : **MC** : mechanical compaction , **TZ**: transition zone and **CC**: chemical compaction.

VI. Discussion :

6.1 Provenance and depositional environments:

6.1.1 Provenance and transport:

The present mineralogical study gives a high abundance of quartz and feldspar for both wells. This abundance suggests an andesitic source rock. The well 7226/2-1 is believed to have received sediments mainly from the Paleozoic rocks and Precambrian rocks from the eastern Uralian orogeny with a possible contribution from the Tamanides and/or Baltica (Bue & Andresen, 2014). Evidences from Mørk (1999) reveal an additional local source existing in the Bjarmeland Platform during the Triassic (Fig. 63).

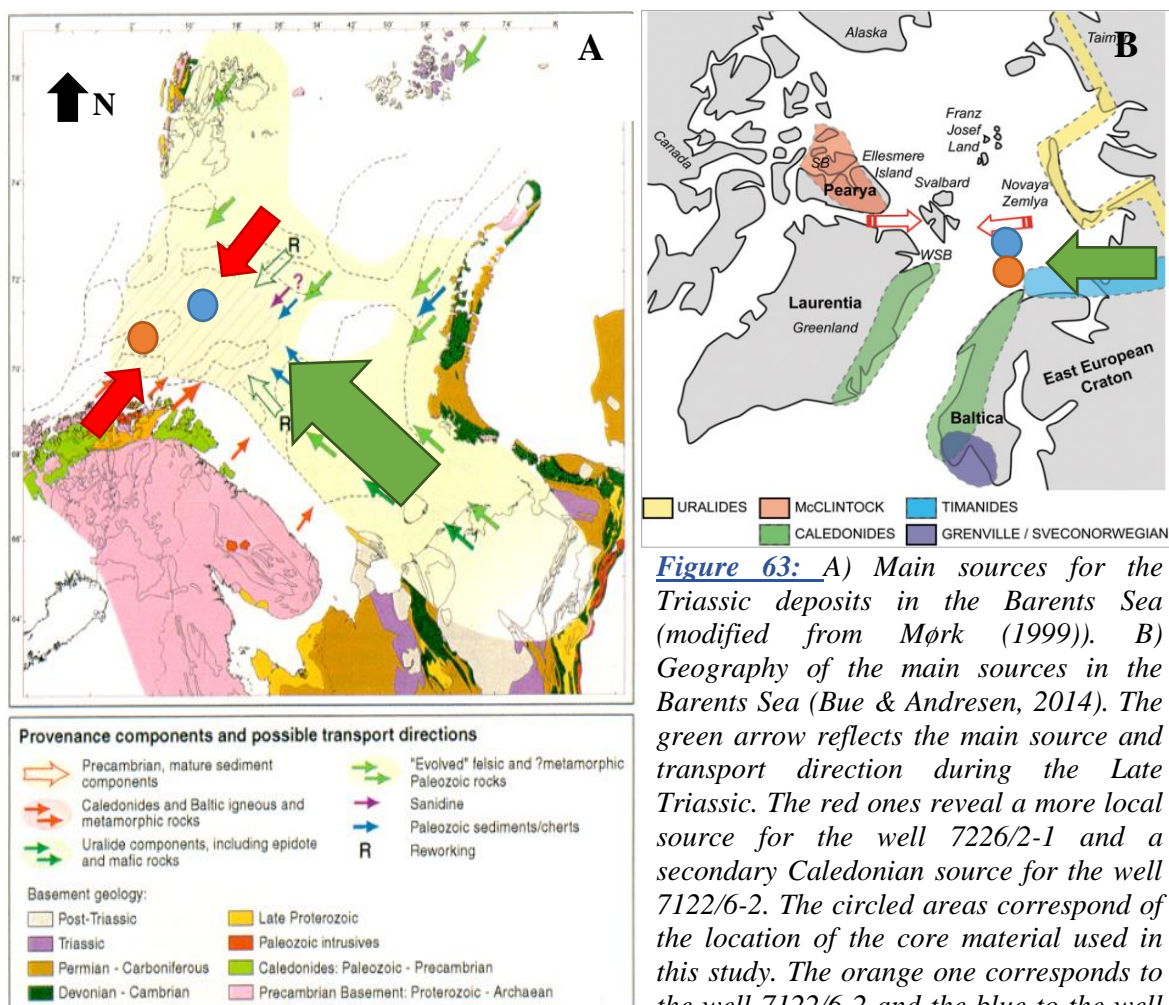


Figure 63: A) Main sources for the Triassic deposits in the Barents Sea (modified from Mørk (1999)). B) Geography of the main sources in the Barents Sea (Bue & Andresen, 2014). The green arrow reflects the main source and transport direction during the Late Triassic. The red ones reveal a more local source for the well 7226/2-1 and a secondary Caledonian source for the well 7122/6-2. The circled areas correspond of the location of the core material used in this study. The orange one corresponds to the well 7122/6-2 and the blue to the well 7226/2-1.

Indeed, the high abundance of chert fragments in the well 7226/2-1 has also been observed by Mørk (1999) in the Bjarmeland Platform and Nordkapp Basin and suggests a more local source from uplifted Paleozoic rocks in the central Barents Sea.

The deposits of the well 7122/6-2, located in the Hammerfest Basin, are also believed to be sourced from the Uralian orogeny since it was the main sediment source in the Late Triassic over the whole Barents Sea (Bue & Andresen, 2014) (Fig. 63). An additional Caledonian sediment source has been proposed by Mørk (1999) based on the observations of medium-high grade metamorphic gneisses, schists and plutonic rock fragments. These types of rock fragments are also observed in the well 7122/6-2 confirming the possible Caledonides as secondary source area for the Hammerfest Basin.

6.1.2 Depositional environment: Well 7122/6-2

The sedimentary facies found in the well 7122/6-2 show high variety (Fig.19). Nevertheless, the association of these makes a clear indication to a tidal influenced environment. The first 5m of the core from 2506m to 2501m depth shows a series of coarsening and fining upwards units composed of both mud and silt to very-fine sandstones. This interval displays heavy bioturbation associated with heterolithic bedding. This interval is believed to be representative of the mixed flats/sand flats area of the intertidal zone in a tide-dominated delta environment (SE2 in Fig.63) (Dalrymple & James, 2010).

A general fining upwards is observed from very-fine sand dominating to mud dominating within the first 15m of the well. The upper part of this interval (2500 to 2489m depth) is composed mostly of mud with thin beds to lenses of sand associated with current sedimentary structures and bioturbation. This interval is believed to be representative of mixed/mud flats of the intertidal area so the upper intertidal zone (SE3 in Fig 64). This zone is still influenced by the tides but doesn't receive as much sediments reworked from the tidal channel as the sand flat (Dalrymple & James, 2010). On the top of this mud dominated interval a 5m thick sand package is observed, containing lenticular and wavy bedding as well as minor bioturbation. This sand package has been interpreted to be part of a small distributary channel or a tidal creek cutting into the upper intertidal zone. An erosive boundary between the sand packages and underlying units would confirm the channel interpretation, unfortunately due to cuts in the core, no boundary could be observed.

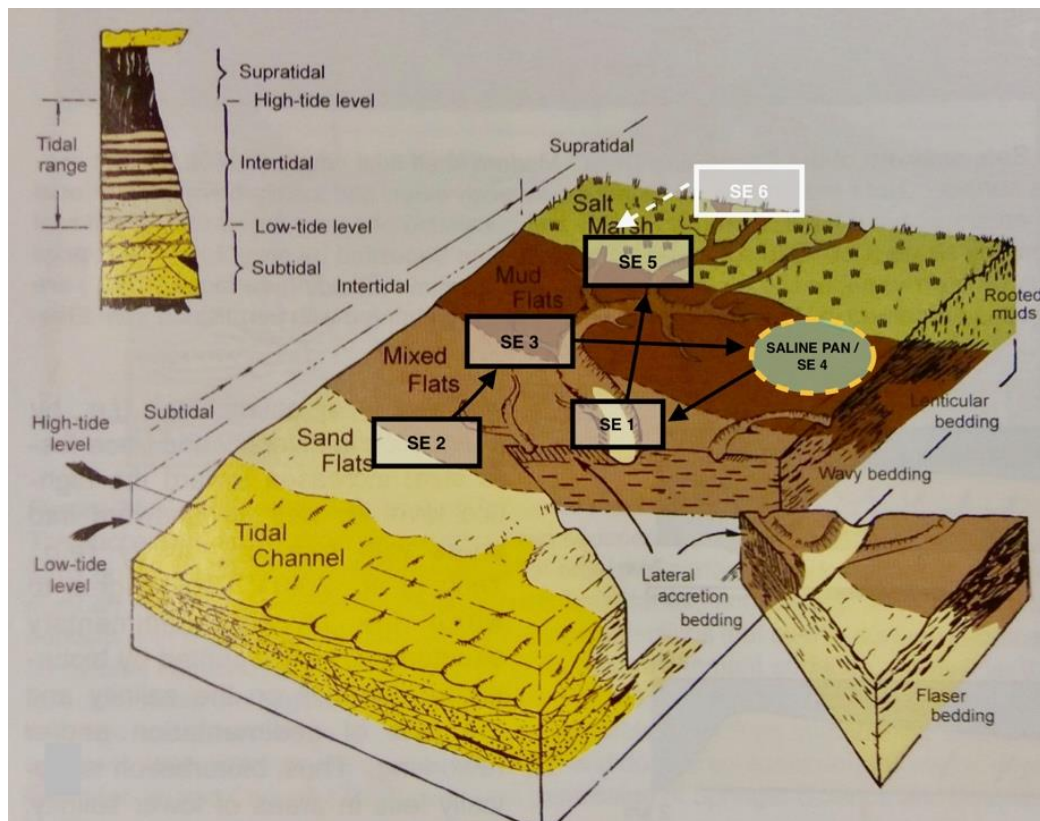


Figure 64: Illustration modified from Dalrymple & James (2010) of the transition from sand flats to salt marsh through mudflats. Those environments are believed to be found overlying each other in the well 7122/6-2 as a progradational sequence. The evolution of the deposits of the well 7122/6-2 start with the sub-environment 2 (SE 2) and follows the path traced by the arrows in a regressive pattern until reaching the sub-environment 5 (SE5). The white box and arrow show the path followed by the deposits of the well 7226/2-1 in transgressive settings.

The next 13m are dominated by dolomite/mud alternations and sand lenses displaying heterolithic bedding. The dolomite observed in the well 7122/6-2 is believed to be from a secondary origin suggested by the chicken wire structure observed at depth 2476,20m, as well as the boundaries of mud layers which show wavy patterns, evocating post-deposition movement likely due to the change in mineral phase. The enrichment in Mg is generally due to the influence of sea water. The formation of dolomite in the well 7122/6-2 can be explained by high evaporation in coastal flooded areas probably linked to an unequal topography. The unequal topography isolates “pools” or “pans” of stagnating marine water subjected to evaporation. This alternation between mud and carbonate appear to be cyclic, 1,5m of dolomitic interval repeating every 1,5m over 24m, half of the studied section. This could represent flooding and evaporation periods in the salina pans (SE4 in Fig.64) (Nichols, 2009; Dalrymple & James, 2010). This carbonate rich interval is directly overlaid by a sandstone interval. This interval is heavily bioturbated with few tidal structures interpreted as a tidal influenced distributary channel or tidal creek (SE1 in Fig.64) due to the thickness

and sedimentary structures found in this interval (Fig.19).

Above this channel the system returns into the mud dominated environment but with a higher sand content. The tidal influence is fading meaning that the location of the system is getting further away from the tidal action (SE5 in Fig 64). This new environment has been interpreted as a marsh setting with some crevasse splay deposits forming sand sheets explaining the amount of clastic deposits (Dalrymple & James, 2010). This marsh environment is cut by a clear channel lag composed of mud clasts, rock fragments and bone fragments observed at depth 2453,5m. This lag is directly overlaid by massive sandstones composing the main channel body.

The whole logged section reflects a prograding tidal flat cut by distributary channels (Fig.64). The observed prograding trend in the log fits with the regressive pattern observed in the Carnian. Indeed, the Late Carnian, age of the studied deposits for the well 7122/6-2, is marked by a regression (Klausen et al, 2015; Skjold et al, 1998). Furthermore, the whole south-western Barents Sea was affected by prograding deltas from the East during the whole Triassic period (Worsley, 2008).

6.1.3 Depositional environment: Well 7226/2-1

The facies found in the well 7226/2-1 are few (Fig.20). The whole core is composed in majority of well-sorted fine-medium grained sand. The lower part of the core, from 1418-1485m depth, is mostly massive with some discrete cross stratifications, while the upper part from 1385-1365m depth, displays heavy cross stratifications and higher mud content (Fig.20). The base of this sandy interval is sharp (Fig.20) with a bioturbated muddy interval at the bottom of the core. This erosional feature indicates the presence of a channel. The cross stratifications are usually directed in one specific direction associated with fine to medium grain size and possibly represent point bar deposits of a meandering system (Fig.65). The study of seismic lines over the well 7226/2-1 made by Klausen et al (2015) also reveals the meandering character of the channel (Fig.66). The bidirectional small cross stratifications towards the upper part of the core may indicate that the system is gradually entering a more marine and tidally influenced environment (Fig.65), meaning a location close to the river mouth. The bell shape observed from the gamma ray log corresponds to a fining upwards sequence (Fig.60-66). The system is then also retrograding. This fining upwards indicates that the energy of the system, i.e. flow, is reducing. This reduction in

energy is probably due to the counteraction of the tidal influence.

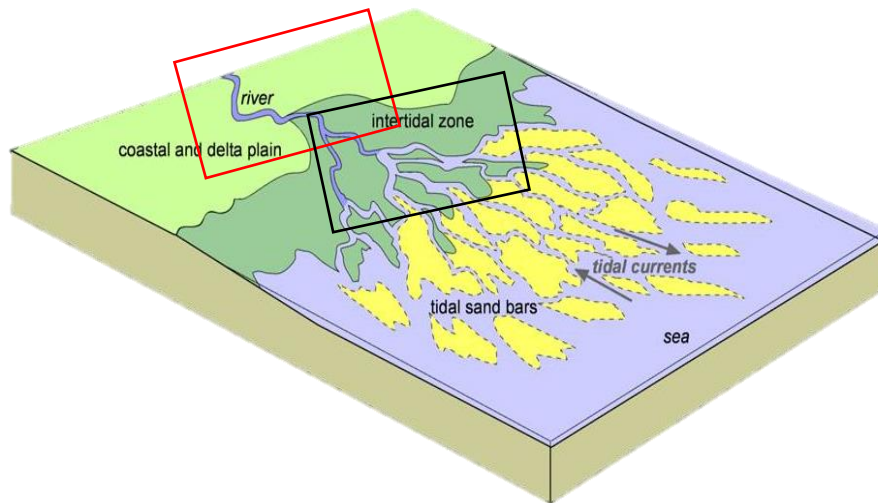


Figure 65: Possible depositional environment for the well 7226/2-1 is marked by the red box. The black box represents the depositional environment for the well 7122/6-2. (Modified from Nichols, 2009)

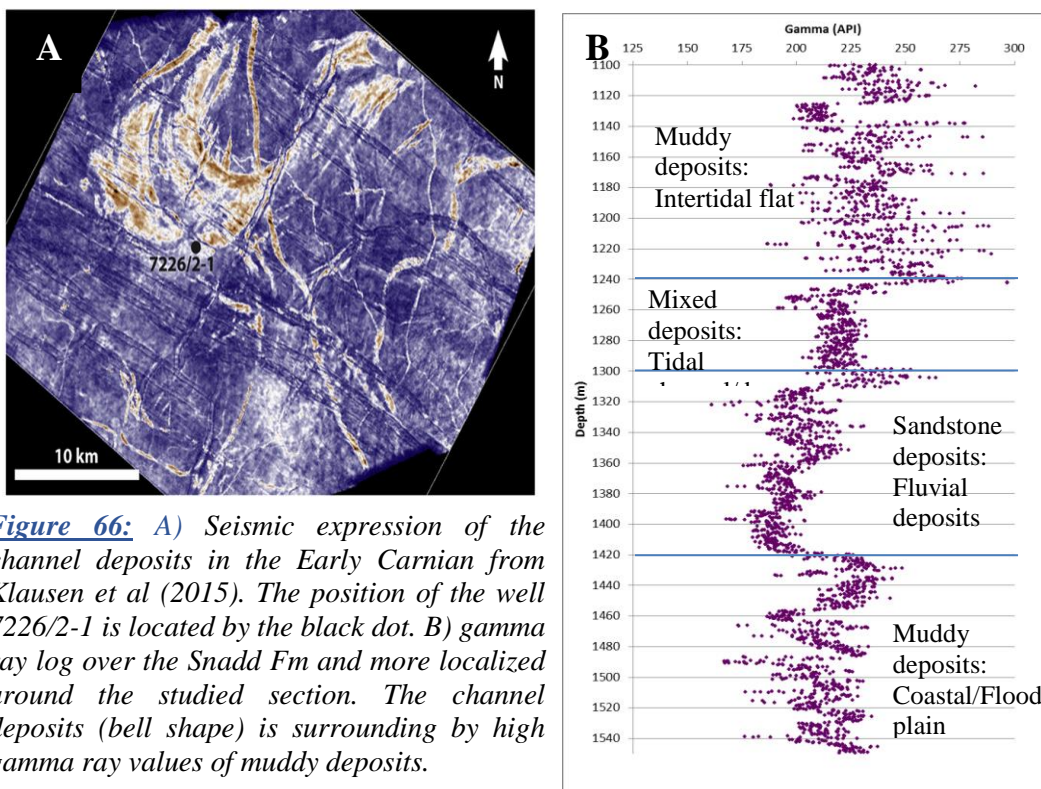


Figure 66: A) Seismic expression of the channel deposits in the Early Carnian from Klausen et al (2015). The position of the well 7226/2-1 is located by the black dot. B) gamma ray log over the Snadd Fm and more localized around the studied section. The channel deposits (bell shape) is surrounded by high gamma ray values of muddy deposits.

The channel deposits present a possible vertical stacking pattern of at least two and possibly three sandstone point bar sub-units identified in the gamma ray curve (Fig.60). The main sandstone body, located in-between mud-rich units, can be identified from the gamma ray log (Fig.66).

At 1390m depth an interval close to a meter in thickness is composed of big mud clasts of a reddish color. Those clasts may have been oxidized on a subaerial exposure (Fig.20). This interval has been interpreted as a collapse of the channel side or levees due to their sparse distribution in the sandy matrix. The channel is then cutting into a muddy plain interpreted as being a marsh/floodplain environment close to the shore explaining the presence of plant fragments and mud clasts. This reinforces the location close to the shore.

In the lower to middle part of the core, from 1390-1418m depth, grains similar to "ooid" in shape have been observed. These deposits are composed of Mg/Mn rich siderite, ranging from 60 μ m to 300 μ m, with a decrease in size from the base towards the middle of the core. The first suggestion from the literature of such deposits is given by Ehrenberg (1993) of ooidal berthierine grains recrystallized by siderite. The berthierine, even if it is mostly formed in marine to brackish waters, can also occur in lateritic environments (Rude et al, 1989; Gehring, 1990), and could have been deposited in the channel by erosion. Nevertheless, the described size of these ooids is usually greater than 250 μ m which is very rare in the studied deposits (Dalrymple & James, 2010; Nichols, 2009). Furthermore, the deposits found in this study seem to be coating the clasts and are formed of concentric layers of radial growth suggesting a more diagenetic origin. They are believed to be sphaerosiderites growing as concentric cement from bacterial mediation. They are associated with the formation of rhombohedral siderite cement nucleation.

6.2 Intergranular volume evolution and compactional regimes:

6.2.1 Well 7226/2-1: Bjarmeland Platform

The intergranular volume, IGV, represents the volume of the pore space after mechanical compaction in grain-supported deposits. The calculated IGV for the well 7226/2-1 is 33% in average, but is separated between the cemented samples (calcite-siderite) with 37% IGV and the non-cemented (pure sandstones) samples with 27% IGV. The loss of porosity due to mechanical compaction is calculated compared to the original porosity (just after deposition), defined at 40% for fine-grained well sorted sandstones (Beard & Weyl, 1973). Figure 67 represents the role of the mechanical and chemical compaction (cements) in the porosity evolution with depth of the samples from the well 7226/2-1.

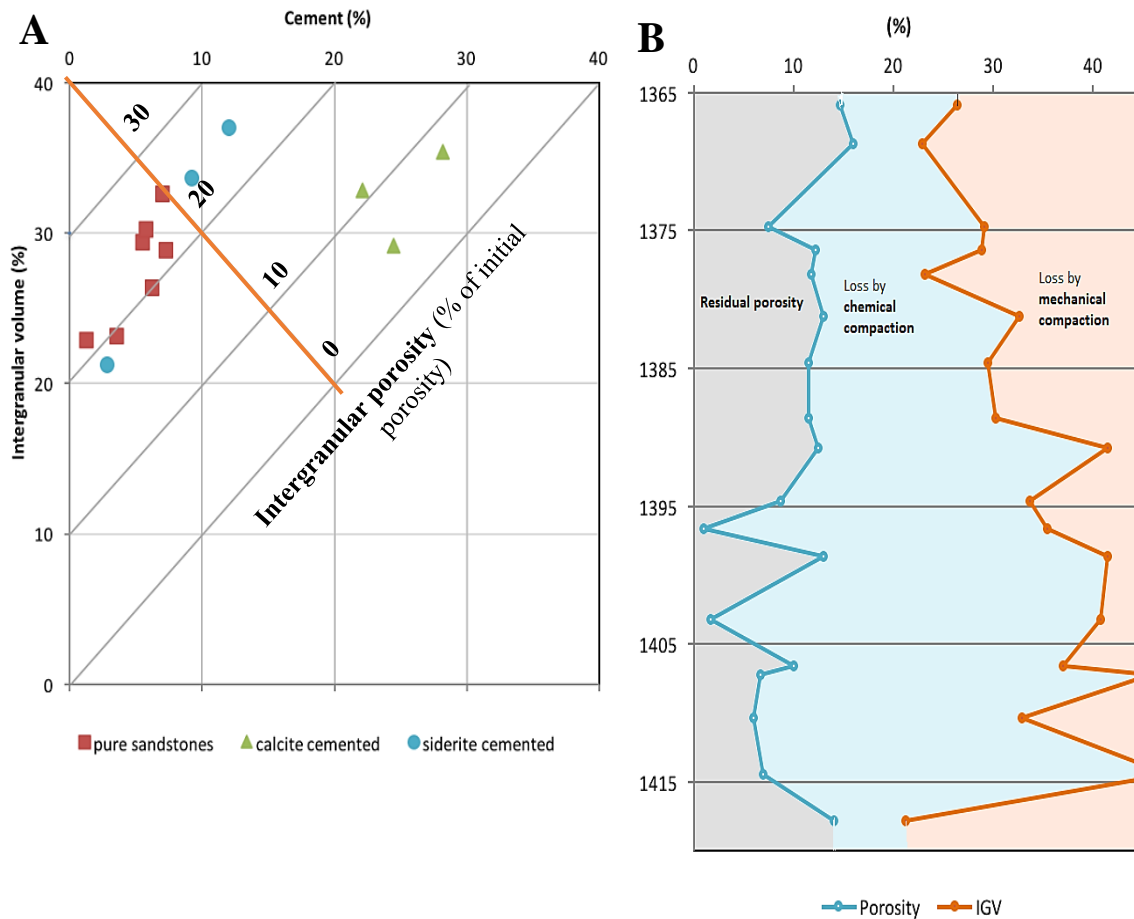


Figure 67: A) diagram showing the relative influence of the chemical compaction for the 3 sample categories: pure sandstones (non-cemented), calcite cemented and siderite cemented intervals. The orange line separates the samples in which the compaction has been more important than the cementation (lower left) from the ones in which the cementation has been more important (upper right). The diagram also assesses the cementation to porosity evolution. The calcite deposits are plotted clearly into the chemical influence and reflect an early diagenesis from the IGW values. The pure sandstones and siderite cemented are mixed and display similar settings and reflect an even earlier diagenesis. B) Evolution of the influence of the compaction regimes through depth. The initial porosity defined at 40% for the samples of the well 7226/2-1. A clear decrease in the chemical compaction influence is observed towards the upper part of the core.

The porosity loss due to mechanical compaction is greater for non-cemented samples, with 31% loss of the initial porosity. The effect of the chemical compaction is less and represents 13% of the porosity loss. This low effect is believed to be due to the thick and continuous chlorite coating found in those intervals (Fig. 68). The chlorite coating inhibits the quartz cementation by reducing the surface area available for its nucleation.

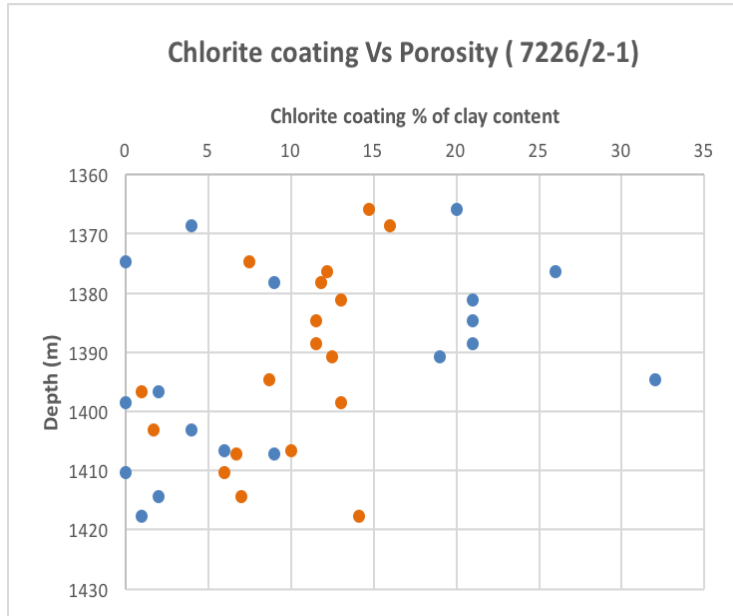


Figure 68: Graph showing the influence of the chlorite coating on the porosity for the samples of the well 7226/2-1. A trend to better porosity with greater extension of chlorite coating can be observed. The red dots represent the porosity with depth and the blue ones the chlorite coating content in percent of the clay content through depth.

The calcite cemented samples are usually fully cemented and display porosity close to zero. The porosity loss due to mechanical compaction in these deposits is 14% in average and reveals their early diagenesis origin. The mechanical compaction effect is even more reduced (4%) in the samples containing sphaerosiderites and rhombohedral siderite cement. This very small effect can be explained by their very early diagenesis (near surface) and the fact that they counteract the compaction by strengthening the grain-framework (Fig.69). Their soft deformation will keep the grains from entering in contact and avoid grain fracturing (Fig.69). Consequently, they also participate in reducing the pressure-dissolution of grains and may have been, along with chlorite coating, preventing quartz cementation in the well 7226/2-1 since almost no quartz cement is found in the siderite cemented interval.

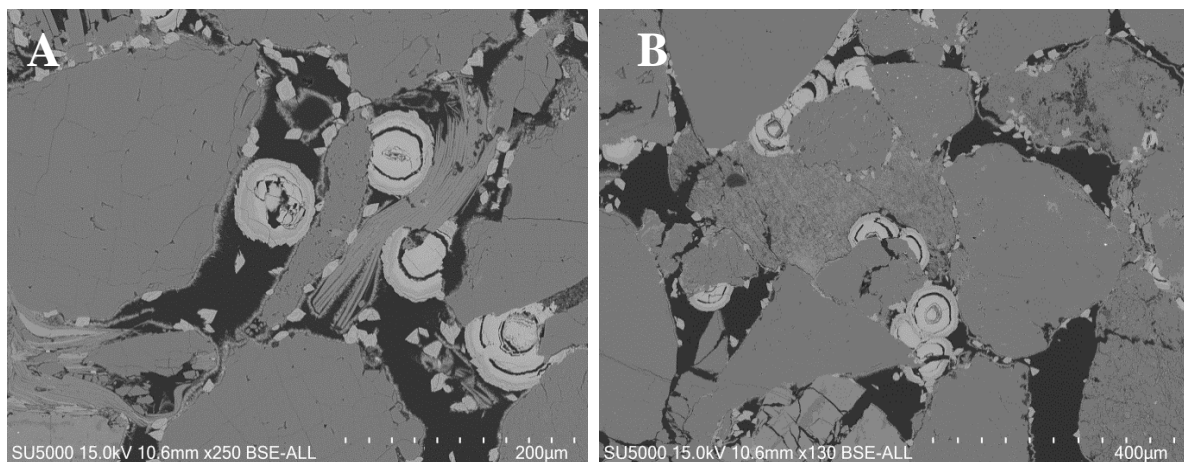


Figure 69: SEM pictures of sphaerosiderites counteracting the compaction. On the image A) sphaerosiderites are involved in the deformation of muscovite grain. B) Sphaerosiderites act against the compaction.

The high IGV observed in the studied samples is also the result of clay matrix deposited with or infiltrated in between the grains due to the mud-rich waters in the depositional environments. This matrix will reduce the porosity greatly and has been calculated to be responsible for 10 to 26% of the initial porosity loss in the studied samples. The matrix content is similar for the siderite rich and pure sandstones but much reduced in the calcite cemented ones. This means that most of the clay mineral infiltration must have happened after the cementation. This is another indication of the early cementation of those intervals, and reinforces the fact that the clay minerals are mostly infiltrated and not deposited.

6.2.2 Well 7122/6-2: Hammerfest Basin

In the well 7122/6-2, only the grain supported samples could be evaluated. The matrix, deposited with the clasts or infiltrated, is the most porosity reducing process (69% of initial porosity loss in average) and is believed to reflect the mud-rich intertidal depositional environment of those deposits.

The effect of the mechanical compaction on the porosity could be assessed only on two samples and represents 10% of the initial porosity loss. This value seems very small for non-calcite cemented intervals. Even if the quartz cementation is extensive in this well, it is not considered as an early mechanism counteracting the mechanical compaction as its formation required higher temperatures. The samples are rich in ductile grains such as mica and mud aggregates. The ductile grains may lead to this apparent reduced mechanical compaction as they deform and create an apparent loose packing (Fig.70). These grains are part of the framework but may act similarly to the matrix.

Therefore, the matrix content is given only as estimation due to the difficulty to make the difference between the depositional matrix and recrystallized pseudomatrix from

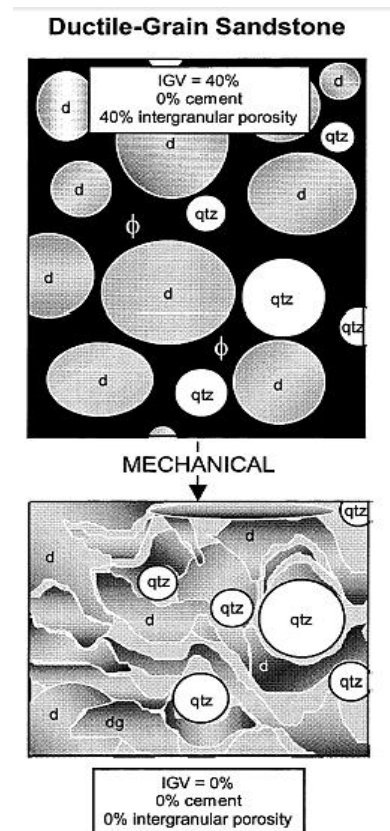


Figure 70: Influence of the ductile grains on mechanical compaction from Paxton et al (2002). The amount of ductile grains in the samples of the well 7122/6-2 is not as high as on this sketch but the apparent reduced mechanical compaction comes from the same process illustrated on this sketch.

altered ductile grains during diagenesis. This content is believed to have been overestimated in this study. Similar difficulties were encountered when differentiating quartz grains from quartz cement, leading to a possible overestimation of the chemical compaction influence in the well 7122/6-2, even if this one is still considered extensive. The chemical compaction influence is believed to have been at 37% of initial porosity loss in average and occurred mostly through quartz cementation.

The influence of the mechanical compaction on the porosity loss can't be clearly quantified from the IGV. But from the observation of thin sections, it seems to have been greater than in the well 7226/2-1 due to the higher amount of compacted grain contact type. Point counting using the SEM or the catholuminescence may give more accurate IGV calculations and enable to make a clearer estimation if the influence of mechanical and chemical compaction in the well.

Most of the studied samples within the well 7122/6-2 are matrix-supported and do not represent any potential in term of reservoir and the amount of matrix is linked to their intertidal depositional environment. The carbonate-rich intervals of this well are composed of a mix of clay-size dolomite and clastic material and are also considered as matrix supported. The existing porosity in those intervals is close to zero.

6.2.3 Mechanical compaction:

The mechanical compaction of the well 7122/6-2 can be assessed only from theoretical data and few observations. It is believed to have been more important than calculated from the IGV. From the study of the grain contact type the well 7122/6-2 is believed to have a greater porosity loss compared to the well 7226/2-1 from the mechanical compaction. This is explained by the moderate sorting which leads to initial worst porosity as well as worst burial porosity (Nagtegaal, 1973). An additional explanation is the large amount of mud aggregates and ductile grains, e.g. micas, which allows more compaction than quartz grains (Bjørlykke, 2015; Luo et al., 2009, Salem et al, 2000).

The calculated uplifts for the wells 7122/6-2 and 7226/2-1 are respectively, 1470m and 1500m, and are fitting with the results of uplift reconstruction in the Barents Sea from Baig et al (2016). They are used as a reference in this thesis. Considering the maximum burial depth for the wells, 2918m depth for the well 7226/2-1 and 3976 m for the well 7122/6-2,

the theoretical reduction of porosity due to compaction is greater for mud-rich sandstones compared to sandstones with a small amount of clay (Fig.71) (Worden & Burley, 2003). The compaction is believed to be syngenetic with the infiltration of precursors for the grain coatings since some of these coatings are found in the intergranular contacts. The observed parallel orientation of the mica and quartz grains in the studied samples of the well 7122/6-2 reveals a high degree of mechanical compaction from grain rearrangement.

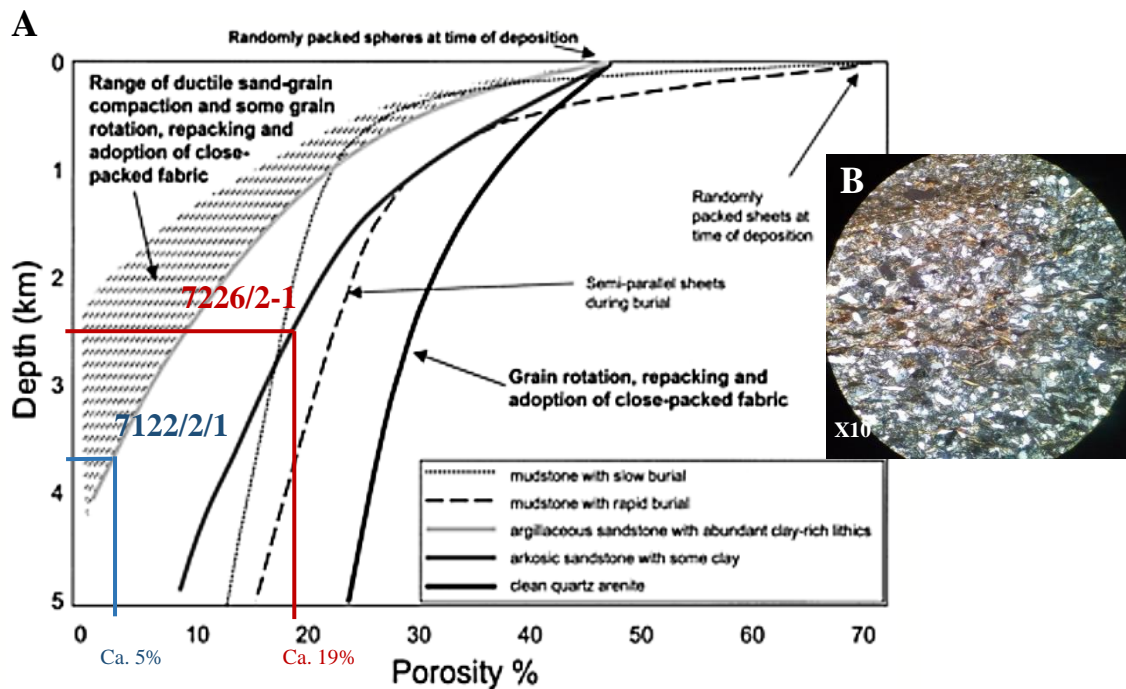


Figure 71: A) Compaction curve for sandstones of different lithologies and for comparison mudstone compaction curves for slow and rapid sedimentation rates modified from Worden & Burley (2003). The full black curve is believed to represent the possible compaction for the well 7226/2-1 due to the lower abundance of clay minerals and the full light grey is believed to represent the well 7122/6-2. The compaction regime is part of the explanation for the difference in porosity and reservoir quality between the two wells. B) Parallel orientation of mica grains in the sample 2463,65m of the well 7122/6-2.

6.2.4 Origin of the matrix:

Several processes can be responsible for the large amount of clay minerals found in the pore space mainly in the well 7122/6-2. The most likely scenario is clay minerals and silt size clasts were deposited conjointly with the clastic material. Some of the matrix may also come from the infiltration of water, enriched with suspended clays, percolating through the sediments (Bjørlykke & Jahren, 2010). This mechanism is believed to be responsible for the presence of clay minerals in the well 7226/2-1. The clay minerals will be then filtered out the water as coating on the grains or as residue in the pore space forming the matrix. This

filtration is preferential in unconfined aquifers with big vadose zones such as in semi-arid climate and/or very thick sand sequences (Worden & Morad, 2003). Both criteria are met for the well 7226/2-1 and the well 7122/6-2, which are located in a semi-arid environment during their deposition (Glørstad et al, 2010). The higher abundance of clay minerals in the well 7122/6-2 is linked to the intertidal depositional environment with low clastic sedimentation (Dunn, 1992).

Smectite filtration in river beds as coating around the grains and recrystallization to chlorite during deep burial is the most probable precursor for the chlorite coating found in the well 7226/2-1. In the absence of evaporation in the river deposits, no concentration of clays minerals will happen around the grain without a concentrating mechanism. The fine-grained size of the deposits might give an explanation to this. In fine grained deposits, the filtration of water will be slower due to smaller pore throats. This slow process will result in a more continuous and thicker grain coating such as the one observe in the samples of the well 7226/2-1 (Matlack et al, 1989).

The volcanic origin of some grains from the Uralian orogeny rich in biotite may reinforce the presence of smectite. The presence of rutile in both wells is a good indicator of biotite weathering. The mixed layers of chlorite-illite observed in the well 7122/6-2 also suggests a precursor smectite coating for the grains in this well recrystallized as cement from about 70 to 80°C (Bjørlykke & Jahren, 2010). The formation of well-developed authigenic chlorite platelets, like the ones observed in the well 7226/2-1 is believed to be a secondary process occurring during deep burial. This statement is supported by the absence of platelets along the intergranular contacts (Bloch et al., 2002).

Berthierine or other green marine clays might also be precursors for the grain coating in the well 7122/6-2 and in the upper more marine part of the core 7226/2-1. Berthierine is formed from a precursor in suboxic iron reducing marine to brackish water, such as the one encountered in this study. Berthierine is an iron rich clay mineral and could be a good precursor for the chlorite coating and platelets (Bjørlykke, 2015).

During the Carnian, the Barents Sea was located in a semi-arid environment with increasing humidity towards the Late Carnian (Ziegler et al, 1994), which led to slightly acidic, dominated by Ca^{2+} and HCO_3^- , pore waters. At shallow depths, this environment will have a large amount of organic matter and undergo bacterially mediated decay (Berner, 1981). Fe-

bearing minerals in the sediments will be reduced to Fe^{2+} by redox processes, which will be available for berthierine formation in the methanogenic zone (Pye et al. 1990).

6.2.5 Chemical compaction: formation of cements

In this study, cement defines every authigenic minerals precipitating in the pore space. These minerals are the products of chemical reactions taking place with increasing burial and temperature. The distribution of those cements in average per well is presented on the figure 72.

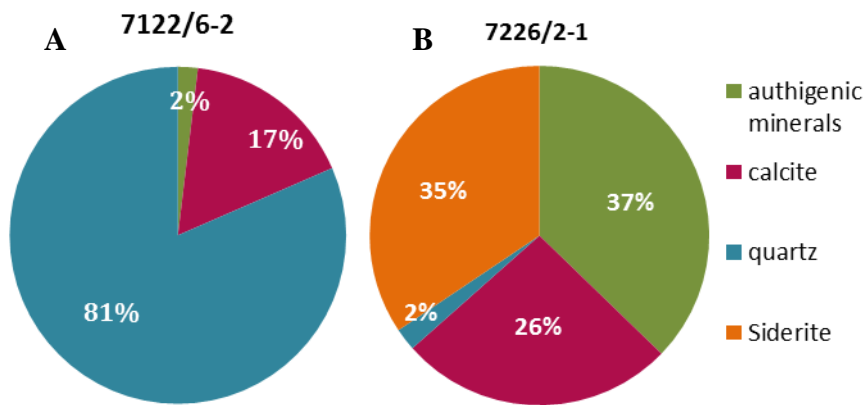


Figure 72: Distribution of type of cement in both wells. The percentages are expressed as % of the cement content. A) Well 7122/6-2 and B) Well 7226/2-1.

Near –Surface processes:

Kaolinitisation:

Kaolinite is observed principally in the well 7226/2-1 up to 5% of the rock volume (Fig.43). In such proximal fluvial sediments, an active percolation of undersaturated meteoric water causes the dissolution of detrital silicates such as lithic grains, feldspar and micas associated with the precipitation of kaolinite at very shallow depths (Bjørlykke & Jahren, 2010). Meteoric water will first dissolve the carbonates and then slowly dissolve the unstable minerals such as feldspar and mica. The decay of organic matter in the ground will produce CO_2 which is added to the ground water making it more acidic hastening the weathering reactions. The acidity will be quickly neutralised by the weathering reactions with silicate minerals and dissolution of carbonate consuming H^+ . The low ratio K^+/H^+ is determining for the precipitation of kaolinite, and the dissolution of silicates such as feldspar or mica will consume H^+ and release K^+ as below:



The dissolution of the grains and flow of water is most prevalent in permeable sediments such as channel deposits (Worden & Morad, 2003). This can explain why more kaolinite has been observed in the well 7226/2-1 than in the well 7122/6-2. Moreover, the intense illitisation of kaolinite in late burial in the well 7122/6-2 may have led to underestimation during the point counting and the XRD analyses.

The precipitation of kaolinite requires that the produced potassium or sodium and silica are removed and the supply of new freshwater effective, for this to happen, a flow of water is necessary (Bjørlykke & Jahren, 2010). In an intertidal zone, such as in the well 7122/6-2, the pumping of water is very effective and often those environments show gentle dipping which will allow the flow of fluid to percolate.

Dolomitization:

Dolomite is found only in the well 7122/6-2. Evaporation concentrates the sea water beyond the point of gypsum saturation which removes Ca ions from the water. The remaining Mg-rich brine is heavier than the sea water filling the pore spaces in the underlying sediment and seeps downwards. Large volumes of water may also pass through previously deposited carbonates causing dolomitization (Longman, 1982). The tidal environment of the deposits of the well 7122/6-2 may also be the reason of the presence of dolomite. During the rise and fall of sea water due to the tides, the seawater is forced through the sediments and each pore volume of water is constantly renewed. Thus, the Mg^{2+} is constantly being supplied while Ca^{2+} , which might “poison” the dolomite crystal structure, is removed. Under this condition, dolomite may form even with less evaporation. The mechanism of dolomitization in the well 7122/6-2 is then believed to be an association of tidal-pumping and seepage refluxion.

Sulphate concentration has a major control on the formation of dolomite (Baker & Kastner, 1981), where dolomitization generally takes place in areas of low sulphate concentration. The sulphate contained in the marine water will become sulphides by bacterial reduction and will be integrated into the formation of pyrite, observed in almost every sample of the well 7122/6-2 (Fig 38). The formation of dolomite is then restricted to the sulphate reducing and methanogenesis zones. The crystal shape of pyrite is different in the sandstone and dolomitic intervals. In the sandstones intervals, the pyrite is found forming framboid aggregates, whereas it is found as single crystals in the dolomitic intervals. The single crystal shape is parented with a formation of dolomite on the top of the reduction zone so at very shallow depth where more of the reactants are present. This is an indication of the very shallow depth

of the dolomitization in the well 7122/6-2. The various crystal sizes observed in the dolomitic intervals of the well 7122/6-2 can be explained by neomorphism occurring with increasing burial depth where none of the precursor structures are conserved (Lee & Friedman, 1987). This neomorphism or recrystallization could explain the chaotic aspect of these intervals. The observed zoned nature of the dolomite reveals a change to ankerite on its outer layer (Fig.36). This zonation suggests that their formation is characterized by changing content of Ca, Mg, Fe and Mn in the pore fluids (Krajewski & Wozny, 2009). The increasing concentration in Fe^{2+} and Mn^{2+} can be due to the transformation of clay minerals such as chlorite and illite, found extensively in the well 7122/6-2 but also due to the dissolution of iron oxides during progressive compaction of shales (Krajewski & Wozny, 2009).

Siderite cement: Sphaerosiderites and rhombohedral cement

The concentric growth and zonation of these grains make them remarkable in the deposits of the well 7226/2-1 (Fig.73). Similar grains have been observed by Weibel et al. (2016) from a Late Triassic study in Southern Sweden. The grains are described as zoned sphaerosiderites.

They are commonly diagenetic induced structure of growth around an organic core element such as pollen grains or leaf cuticles. The typical radiating growth patterns of the grains observed in the well 7226/2-1 are also observed in southern Sweden by Weibel et al. (2016) (Fig.73. A. D). The bacterial activity is considered as growth related process. These nucleations and sphaerosiderites observed in the well 7226/2-1 seem to be initiated on the first chlorite coating (recrystallized precursor) (Fig.73).

Even if the theory of growth from an organic core can't be refuted here, it appears that most of the sphaerosiderites and all the rhombohedral cement originated their growth from the coating (Fig.73). The formation of siderite cement and sphaerosiderites may have used the Fe^{3+} available in the precursor coating by bacterial activity, causing depletion for the formation of chlorite platelets in late burial. However, this depletion is very local and does not prohibit the formation of platelets around the grains since the thickness of the chlorite coating is not reduced and stays constant averaging $8\mu m$ throughout the core. Figure 74 presents the total percentage of chlorite coating and sphaerosiderites through the core. The amount of chlorite coating seems to be reduced in the samples containing a high amount of sphaerosiderites. This can be explained by the fact that the growth on the precursor chlorite coating reduced the available place for the crystallisation of the platelets in late burial.

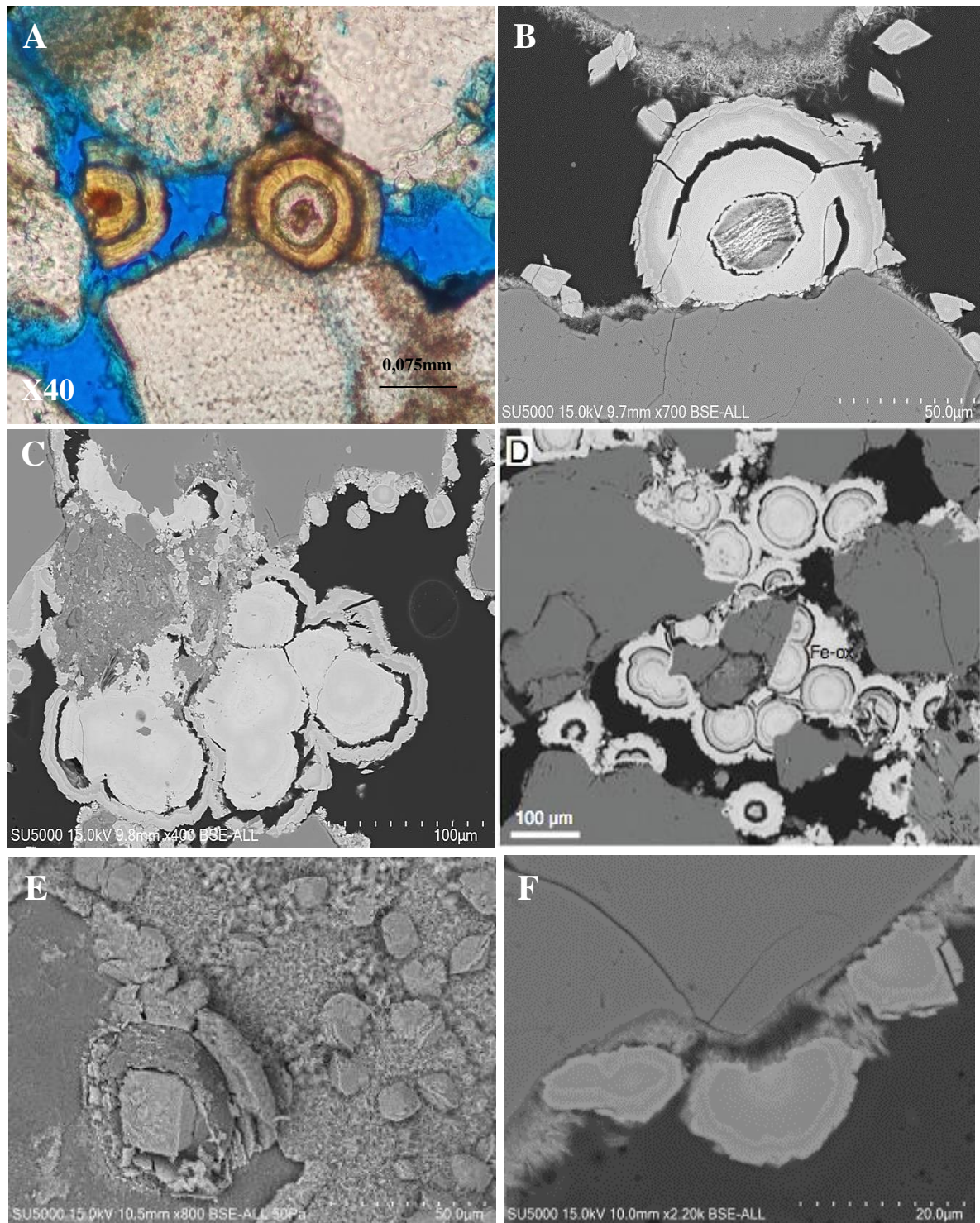


Figure 73: A) Example of sphaerosiderites taken from the well 7226/2-1and observed in thin section. The growth of the sphaerosiderites is controlled by the emplacement of the surrounding grains. To note the radial crystals in the middle layer of the sphaerosiderites. B) Siderite cement growing on the sphaerosiderites observed with the SEM. C) Clusters of sphaerosiderites observed also at the SEM. D) Sphaerosiderites observed in the study of Weibel et al (2016). E) SEM picture from a stub showing the 3D spatial arrangement of the siderite compounds on the chlorite coating. F) Growth of a siderite cement linked to the chlorite coating.

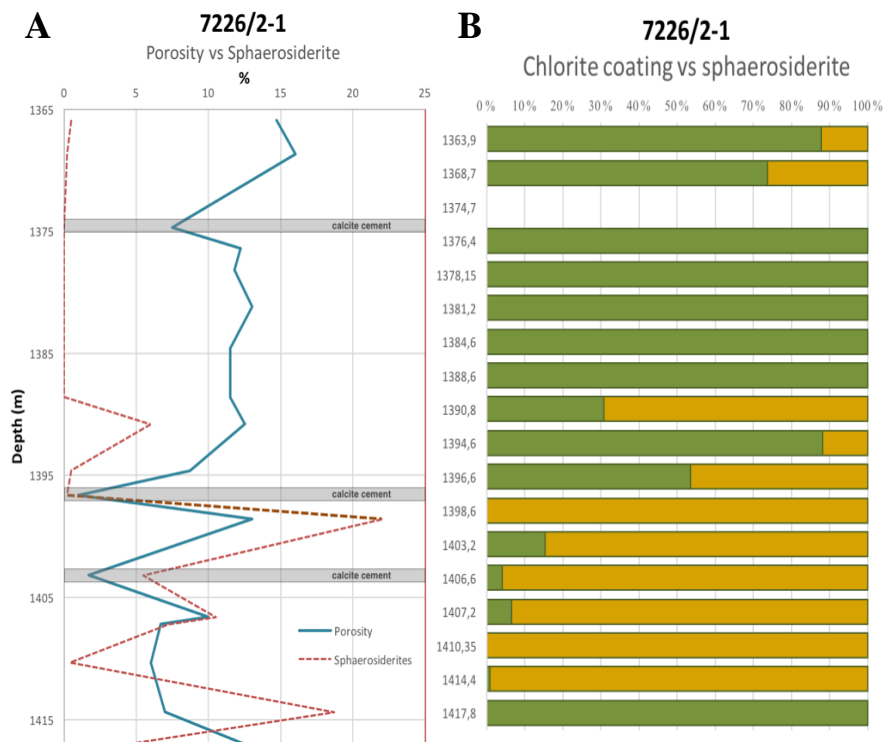


Figure 74: A) Reconstructed porosity curve of the well 7226/2-1 associated with the abundance of the sphaerosiderites from the point counting. The grey intervals represent calcite cemented intervals corresponding to reduced porosity. B) Abundance of chlorite coating among the clay fraction from the point counting against the abundance of sphaerosiderites also from the point counting. A clear relationship can be established in the lower core where the chlorite coating abundance is very reduced compared to the one of sphaerosiderites.

The chemical composition of the Sphaerosiderites is not pure, containing up to 3-5% of Mg and Ca. Even if freshwater siderite tends to be pure, low percentages in Mg and Ca still suggest a meteoric water composition (Mozley, 1989; Morad et al, 2000; Weibel et al, 2016). Similar sphaerosiderites have been observed previously in the Barents Sea, more precisely in the Nordkapp basin in the study of Auset (2012). Similar chemical composition to the ones present in this study suggests similar conditions of formation. The comparison with the work of Mozley (1989), with regards to the chemical composition of siderite gives a freshwater origin to the siderite in the well 7226/2-1. The results of this comparison are presented in Figure 75. In the studied samples, the iron content reaches 91% in the middle layer and averages in all layers at 80%. The high amount of Fe is indicating a fresh water origin, since there are no documented cases of marine siderite approaching end-member composition (Mozley, 1989).

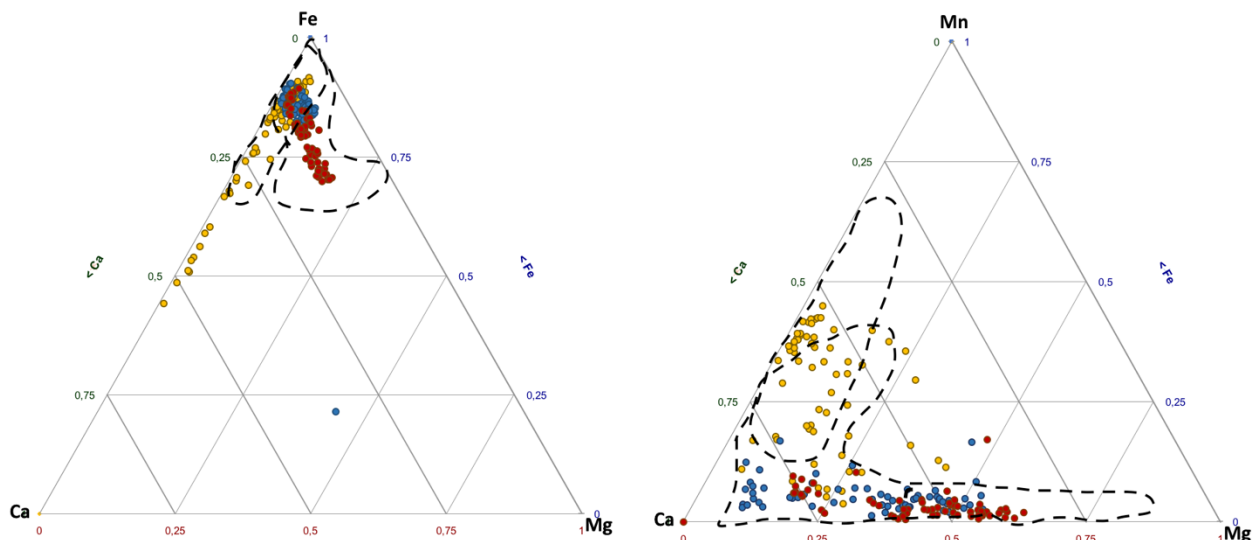


Figure 75: Chemical composition of the sphaerosiderites in the well 7226/2-1 from several samples. The red points represent the outer layer of the concretionary grain, the blue points represent an intermediate layer of the concretion and the yellow represent the inner layer of the concretions. The dots areas correspond to the chemical composition of fresh water siderite from Mozley (1989). The increase in Mg in the outer layer suggests a recrystallization due to marine influenced pore waters.

The growth continues as spherical zones around the core as the bacterial colony carries on its reduction of Fe and Mn. Those elements react with HCO_3^- , liberated during the degradation of organic matter, and lead to the precipitation of siderite. The rate of bacterial reduction is determined based on the availability of Fe^{2+} and is the limiting factor for the precipitation of siderite. The sphaerosiderites occur as clusters which have been interpreted by Weibel et al (2016) as a probable mark of the outline of the microbial communities (Fig. 73).

The outermost part of the sphaerosiderites seemingly has a different cementation pattern, forming etched surfaces similar to the ones of the rhombohedral cement (Fig.73). The chemistry of the outer layer of the sphaerosiderites (Fig.47,75) is also similar to the one of the rhombohedral siderite cement. This indicates that the outer layer and the cement may have crystallised from the same pore water. The difference in chemistry observed in the rhombohedral grains and outer layers is believed to be due to a change in pore water composition (Rodrigues et al, 2015). This change in pore water composition and the enrichment in Mg is believed to be due to a mixing of the pore water with marine water increasing the Mg/Fe ratio. The enrichment in Mg of the pore water will tend to form Mg-rich siderites and is believed to be responsible process in the change in cementation pattern observed in the samples.

The siderite cementation occurs before or during most of the compaction since they have been observed between two grain contacts. This suggests a very shallow, near surface, formation. This observation is confirmed with the very low reduction of porosity from mechanical compaction estimated at 4% of loss of initial porosity.

Pyrite was observed in almost every sample of the well in small amounts. Pyrite, FeS_2 and siderite Fe_2CO_3 are also observed together in some samples (Fig.76). Their combined appearance is unusual since, even if they share the necessity of anoxic conditions and reduced iron to form, pyrite requires additional sulphate, which is an inhibitor for siderite formation. They are believed to reflect different stages in the diagenetic bacterial activity in the well 7226/2-1.

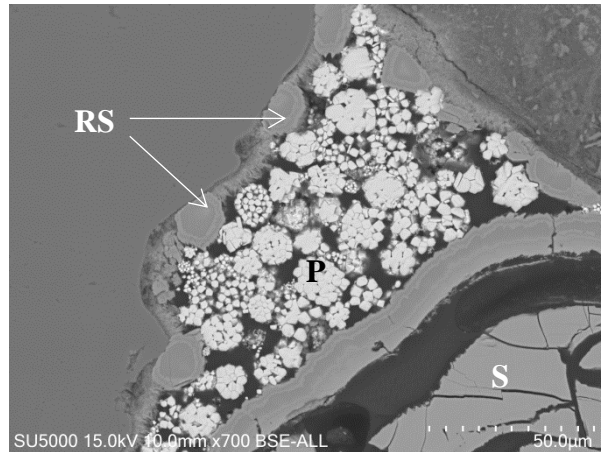


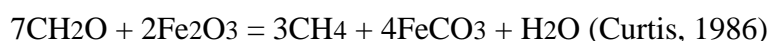
Figure 76: Framboid pyrite grains (P) with sphaerosiderites (S) and rhombohedral siderite cement (RS) in the well 7226/2-1. SEM.

The iron may come from the reduction of fine grained detrital iron oxide minerals by organic matter in sediments (Berner, 1981), or from iron-rich grain coating, pore filling chlorite or iron-rich rock-fragments in the well 7226/2-1. O_2 is quickly depleted in organic rich sediments by aerobic decay and anoxic conditions occur very fast after deposition. The precipitation of pyrite or siderite depends on the presence of sulphide H_2S or HS^- . The overall equation for the formation of pyrite is shown below:



Sulphides are produced from sulfate during bacterial decomposition of organic matter. Marine water is more enriched in sulphate compared to freshwater by a factor 100 (Berner, 1981). Pyrite is then a probable indicator of marine influence on the deposits in early diagenesis for the well 7226/2-1.

Siderite forms by the combined effect of iron reduction and bacterial methanogenesis of organic carbon compounds following the equation below:



If sulphate is present, Fe^{2+} will be preferentially integrated into the formation of pyrite instead of siderite by its reaction with sulphides. Pyrite formation is two times more energetic than siderite formation and bacteria will prefer the more efficient way to get energy.

The disappearance of the sphaerosiderites and rhombohedral siderite cement in the upper part of the core 7226/2-1 (1365-1390m depth) may suggest an entry into more sulphidic environment such as the marine realm. This is also reflected by the decrease in size of the sphaerosiderites towards the top of the core. The smaller size might represent an environment richer in sulphate, such as mixed-water, slowing down their growth. When the amount of sea water increases the sulphate content increases as well, and the pyrite will use the Fe^{3+} to formed leading to a reduced growth of the siderite. This geochemical observation together with the different cementation pattern of the outer layers fits with the sedimentological observations also suggesting an increase in marine influence towards the upper core. Moreover, the transition between the Early Carnian and Middle Carnian is marked by a flooding surface putting the Early Carnian, and the studied section of the well 7226/2-1 into a transgressive period (Klausen et al, 2015).

Shallow to intermediate burial diagenesis :

Clay mineral diagenesis:

Authigenic chlorite is observed in both wells and typically has a small effect on the porosity. It occurs as grain replacement and chlorite platelets on the chlorite coating. This replacement by chlorite comes after the grain coating in both wells. Transformation of the chlorite precursor as grain coating occurs at burial depths greater than 2000-3000m and temperatures greater than 60-100°C (Bjørlykke, 1998; Worden & Morad, 2003).

With burial, the smectite deposited in the wells transformed progressively first into poorly ordered then well-ordered mixed layers chlorite/smectite or illite/smectite (Morad et al, 2000)

Calcite cement:

Diagenetic calcite cement is observed in both, but only in the well 7226/2-1 as complete layers. The high IGV found in the cemented intervals of the well 7226/2-1 (>40%) associated with the presence of undeformed ductile grains and floating grains within the cement suggests a shallow burial origin. The calcite is believed to have formed in shallow

burial diagenesis because it postdates some of the compaction (14% average in the well 7226/2-1) and the first layer of chlorite coating. Minor calcite can come from the alteration of Ca and Mg bearing minerals such as plagioclases and biotite during the weathering of the source rock (Salem et al, 2000). These minerals are found in both wells.

Nevertheless, most of the calcite cement originates from biogenic carbonate by direct deposition such as by the deposition of shell debris or by weathering of previously deposited carbonates. Only the calcite cement of the well 7122/6-2 is believed to be derived from direct transformation of biogenic carbonate materials consisting of high Mg calcite transforming into low Mg calcite during shallow burial (Saigal & Bjørlykke, 1987).

In the continental environment of the well 7226/2-1, calcite is formed by the concentration of ions in the groundwater due to weathering reactions and net evaporation. This is

highlighted by the fact that the calcite cemented interval occurs associated with red colored beds and the presence of hematite maybe due to a subaerial exposure of the deposits and evaporation.

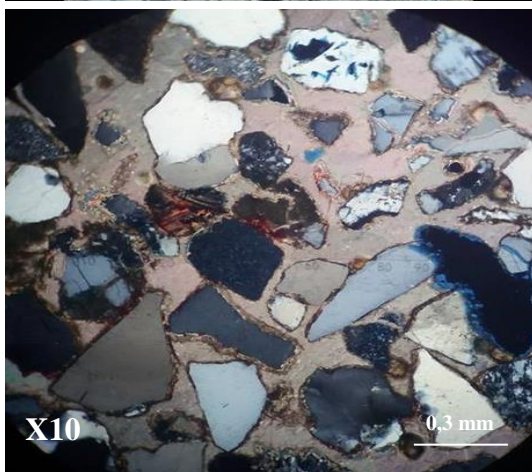


Figure 77: A) *Meniscus observed from microscopy in the well 7226/2-1.* B) *Typical calcite cemented sample of the well 7226/2-1. Note the small mechanical compaction prior to cementation.*

Some evidences such as meniscus (Fig.77) in the cement on the upper part of the well 7226/2-1 (1378m depth) indicate a vadose origin of the cement (Hanken et al.2010). The blockier appearance of the cement in the lower part of the core associated with the possible presence of siderite glaeboles (sample 1414, 40m) suggest a phreatic origin of the calcite cement in the lower part the well 7226/2-1 (Fig.77) (Hanken et al. 2010). These observations confirm the theory from the siderite cementation and may represent as well a shift from meteoric to mixed marine pore water up-core.

Minor amounts of calcite may have resulted from the albitization of detrital plagioclase releasing Ca ions (Salem et al, 2000). The albitization of K-feldspar is observed in all the sandstones samples studied for this thesis. The albitization is pervasive and reaches the point of total replacement of grains in the well 7122/6-2. This reaction is controlled kinetically by the consumption of K^+ in the illitization process (Aagaard et al. 1990). Therefore, albitization also participates in the formation of the extensive illite observed in some samples in the well 7122/6-2. Albitization does not change the reservoir properties by itself but the release of calcium might participate in some of the cement observed in both wells and reduces the porosity.

The carbonate cemented layers seem to conserve the feldspar grains from extensive dissolution. Indeed, when these layers are absent in the interval from 1384m to 1394m depth, the K-feldspars dissolution degree is averaging at 3-4° whereas elsewhere it averages at 2-3°. The lack of cyclic cemented intervals in the well 7122/6-2 may have contributed to the lower amount of feldspars observed, 5% compared to 7% of the total rock volume in the well 7226/2-1.

Deep burial diagenesis:

In the studied samples, most of the reservoir potential is lost during the near-surface to shallow burial. The small leftover porosity will be partly filled by chlorite platelets, in the well 7226/2-1, and illite and quartz cement, in the well 7122/6-2, during deep burial. The chlorite coating recrystallized during burial will be the base of further recrystallization as platelets during the deep burial (Bjørlykke & Jahren, 2010; Jahren & Aagaard, 1989). The chlorite platelets form by precipitation from the pore waters, by grain replacement cement and from the precursors (Jahren & Aagaard, 1989). This formation will occur at temperatures higher than 80°C (Aagaard et al, 2000). In both wells the first thin coating is present at the intergranular contact but the platelets are present only in the open pore space enhancing the post compaction time frame for this recrystallization.

The recrystallization of kaolinite to dickite has been observed in both wells. At 2000-3000m burial the temperatures reach 70-90°C, the kaolinite composed of thin booklet like grains will be progressively replaced by thick, blocky crystals of dickite. The direct dissolution-reprecipitation process is not likely to have happened extensively in both of wells, because it creates a disruption in the stacking pattern of kaolinite and each time kaolinite was observed

the stacking pattern was conserved. The transformation to dickite is then believed to have been made through progressive burial. The blocky dickite is dominating at depths superior to 4kms and temperatures higher than 130°C (Luo et al., 2009); the well 7122/6-2 is then believed to display dickite. Few crystals were observed but the intense illitization might explain this lack of observation. (Fig.78)

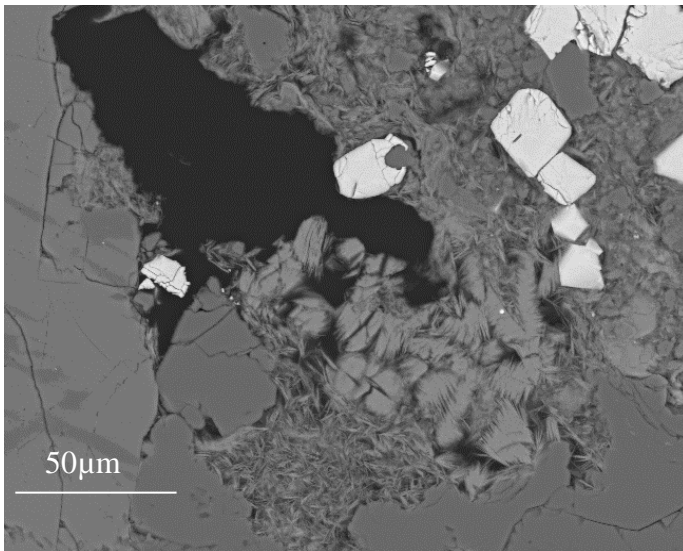


Figure 78: SEM picture of Illitized kaolinite grains in the well 7122/6-2

Quartz cementation is believed to occur mostly after the formation of chlorite in both wells. The cementation is presumably sourced by closely-associated intergranular pressure-dissolution of detrital quartz (Bjørlykke & Egeberg, 1993; Luo et al., 2009, Morad et al, 2000). Pressure dissolution is most extensive in sandstones rich in mica and illitized grain coatings such as the samples of the well 7122/6-2 (Bjørkum & Nadeau, 1998; Luo et

al., 2009). This catalytic effect is responsible for the large cementation in the well 7122/6-2.

The precipitation of quartz cement is closely associated with the precipitation of illite in the well 7122/6-2. As soon as the quartz starts to precipitate, the system becomes undersaturated in silica with respect to smectite and chemical processes can start acting such as the illitisation of smectite and later of kaolinite as follows:

- *Smectite + K-feldspar = illite + chlorite + quartz (Boles and Franks, 1979)*
- $KAlSi_3O_8 + Al_2Si_2O_5(OH)_4 = KAl_3Si_3O_{10}(OH)_2 + 2SiO_2 + H_2O$
K-Feldspar + Kaolinite = Illite + Quartz

The well 7122/6-2 had been buried deeper than the well 7226/2-1, with temperatures around 140°C while the well 7226/2-1 reaches only 100°C. The rate of quartz precipitation increases exponentially with increasing temperature and doubles up to 4 times between 100-140°C (Bjørlykke & Egeberg, 1993). This could explain the more extensive quartz cementation observed in the well 7122/6-2.

Nevertheless, quartz cementation is also a function of the surface area available for cementation (Bjørlykke & Egeberg, 1993). The grains of the samples in the well 7226/2-1 are systematically coated by chlorite/siderite, the surface available is drastically reduced, explaining the low cementation. Moreover, the deposits of the well 7122/6-2 are smaller grain size than the ones of the well 7226/2-1 and it has been shown that smaller grain size develop more quartz cement due to higher surface area available for cementation (Walderhaug, 1996). The higher degree of quartz cementation in the well 7122/6-2 is believed to be caused by the association of more surface area available, due to the lack of chlorite coatings and smaller grain size, and higher burial temperature.

Illite was extensively observed in the well 7122/6-2 forming needle like structures but also as furry patches. Illite has not been observed directly in the well 7226/2-1 but was found in the mineralogical analysis in small percentages. Illite can form from many alteration processes. In the well 7122/6-2 it mainly comes from the alteration of smectite since it is often found as mixed layers with chlorite, but part of it may also come from the illitization of kaolinite as observed on the figure 78. The formation of illite from smectite occurs in a temperature range of 70-100°C (Bjørlykke, 1998), which both wells have reached during their burial. The formation of illite from kaolinite occurs above 130°C because of the field of stability of kaolinite and k-feldspar. From the reconstructed burial temperature, illitization of kaolinite probably only took place in well 7122/6-2. The illitization of smectite rich intervals such as the ones of the well 7122/6-2 may improve slightly the reservoir quality as illite has a lower specific surface area than smectite (Bjørlykke, 1998).

Most of the samples of the well 7122/6-2 contain mostly quartz grains and clay matrix which has been identified to be mixed illite and chlorite. This kind of mineral assemblage is stable up to high temperatures because they are all metamorphic minerals (Bjørlykke, 2010). With increasing overburden and temperature, this assemblage is not likely to change but will develop the pronounced cleavage typical of shales due to the higher degree of parallel orientation of the sheet silicate minerals (e.g. illite, chlorite) observed in the studied samples of the well 7122/6-2 (Bjørlykke, 2010).

The diagenetic history reconstruction for both wells is presented in Figure 79.

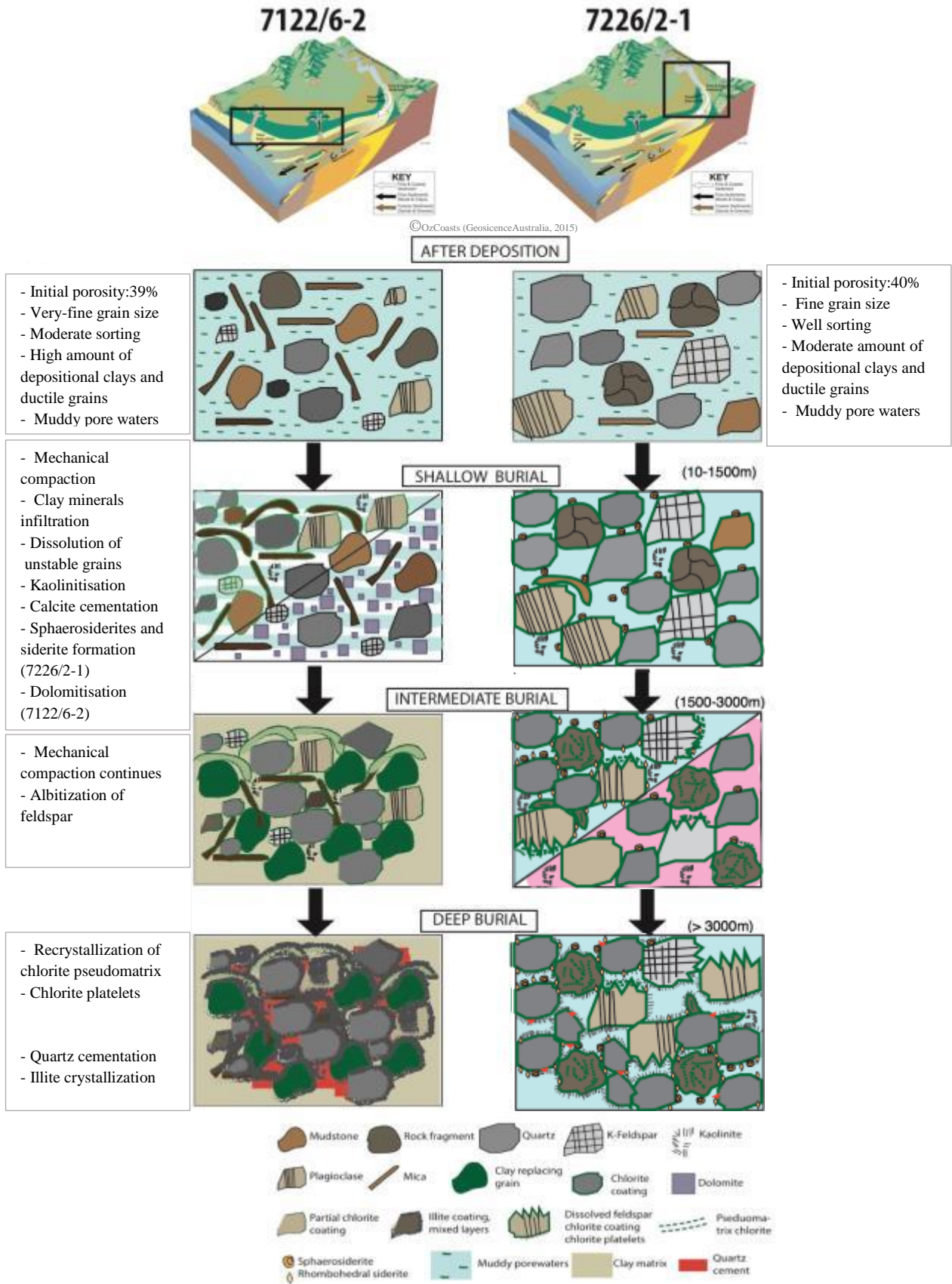


Figure 79: The combined diagenetic history for the well 7122/6-2 and the well 7226/2-1. The rectangle text boxes on the left side resume the main diagenetic processes occurring jointly as well as individually. When the square box is shared in two, it indicates that difference occurred in the diagenesis for the samples of the cores.

6.3 Permeability evolution:

The reservoir quality for the two wells as they are today is considered as moderate to good for the well 7226/2-1, and poor for the well 7122/6-2. The well 7122/6-2 owns a very low porosity around 5% in average; this value does not record the micro-porosity of the clay minerals. The abundance of clay minerals makes the reservoir potential drop drastically since it highly reduces the permeability. The well 7226/2-1 presents a better porosity averaging at 12% and observed permeability acceptable. Even if the porosity is close to the 10% cut off value defined by the industry, it can be acceptable for a gas reservoir.

The moderately sorted fine to very fine grained deposits disadvantage the well 7122/6-2 compared to the well 7226/2-1 as they compact more than well sorted fine grained deposits (Fig.80). The same parameters also affect the permeability which is lower in the well 7122/6-2 (Fig.80). The permeability is not good for either of the wells with average 0, 5 mD in the well 7122/6-2 and 17 mD in the well 7226/2-1. Those values are well under the usual tens of hundreds of mD usually found in sandstone deposits (Fig.80).

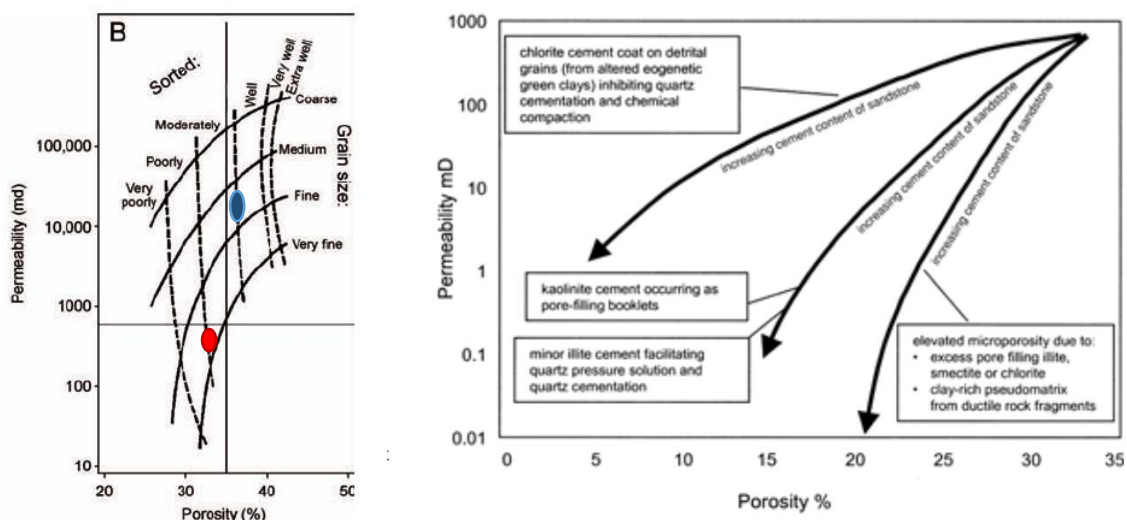


Figure 80: A) Porosity – permeability diagram demonstrating the main differences between types and morphologies of clay minerals in sandstones from Worden & Morad (2003). This figure perfectly illustrates the main initial differences between the two wells due to their difference in assemblages from the depositional environments. B) Graph of the initial porosity and permeability between different grain sizes and sorting in sandstones modified from Nagtegaal (1978). The well 7122/6-2 composed mostly of very fine grains moderately sorted is expected to have a lower initial porosity and permeability compared to the well 7226/2-1 fine grained – well sorted. The red point reflects the well 7122/6-2 and the blue point 7226/2-1.

These values seem extremely low and need to be taken as estimations for the fluctuations within the wells, but cannot be used solely as an indicator. To quantify the permeability in

these wells, helium permeability measurements or CT scans might give better estimations close to the real values.

In addition to the abundant clay minerals in the deposits of the well 7122/6-2, the expansion of biotite grains from shallow burial alterations and the precipitation of microcrystalline carbonate along the planes cause a choking of the adjacent pore throats (Luo et al., 2009). The presence of detrital micas induces a partial deterioration of the porosity and permeability.

6.3.1 Influence of the chlorite coating:

The chlorite coatings around the grains of the fluvial deposits of the well 7226/2-1 retarded the precipitation of quartz overgrowth and hence prevented a greater loss of porosity. However, the extensive chlorite platelets present in many of the samples of the upper core may cause a blockage of the pore throats and thus reducing the permeability (Anjos et al. 2003, Worden & Morad, 2003). The diagenetic siderite cement in the fluvial deposits, particularly in the lower core even if they reduce the porosity, participates to preservation of the permeability as they reduce the surface area for the chlorite platelets growth.

The water saturation contained in the chlorite crystals micro-porosity will increase the overall saturation. This process will affect the oil saturation evaluation from resistivity log (Anjos et al. 2003; Morad et al, 2000).

6.3.2 Influence of other clay minerals diagenesis:

The clay rich matrix samples observed in the well 7122/6-2 display high amount of void space but the scale is micrometre or smaller associated with a poor interconnectivity. These parameters play the role to baffle the fluid flow and destroy the reservoir potential (Hurst & Nadeau, 1995). Clay aggregates are observed in both wells but are far more abundant in the well 7122/6-2. They have a small effect on the porosity but abundant pseudomatrix in some samples of the well 7226/2-1 can behave like plugs or baffles and reduce the permeability as well (Worden & Morad, 2003). Clay coatings preserve porosity in sandstones that have been subjected to less compaction due to partial cementation (Quartz, calcite) but in sandstones lacking such framework support, such as in the well 7122/6-2, illitic clays enhance pressure dissolution (Salem et al., 2000) involved in the quartz cementation process.

6.3.3 Influence of the dolomite diagenesis :

The carbonate intervals may be as detrimental as useful if they are laterally extensive and may prevent the flow of gas from below the oil/water contact and from above the gas/oil contact (Bjørlykke & Jahren, 2010). Dolomitization process has been proven to enhance the reservoir quality in carbonate sequences creating enlarged pore spaces as a result of an increase of crystal size. Limestone mud-dominated assemblages have mud sized particles (<20 μm) and very small pore spaces. The effect of dolomitization will create crystal sizes ranging from 10 μm or less to more than 200 μm with corresponding pore sizes (Lucia et al, 2003). The result of dolomitization will be an enhanced porosity and permeability. This enhancement is at the condition that no deep-burial neomorphism happened (Rahimpour-Bonab et al, 2010). Indeed, the recrystallization during burial as observed in the well 7122/6-2, will form fabric-destructive dolomites and drastically reduce the reservoir quality (Rahimpour-Bonab et al, 2010).

6.3.4 Influence of the sphaerosiderites and siderite cement:

The sphaerosiderites and rhombohedral cement reduce slightly the permeability from 24mD to 22mD in average (Fig.81). These authigenic deposits have a negative impact on the permeability. However, they tend to form as clusters and may explain why the reduction of permeability compared to the intervals where they are absent (upper core) is not so important.

Table 8 summarizes the processes influencing the reservoir quality for both wells in view to characterize them as poor for the well 7122/6-2 and moderate-good for the well 7226/2-1.

Table 8: Comparison of the mineralogical, diagenetic and textural influences on the reservoir quality between the two wells. The relative abundance of the minerals for the well 7122/6-2 are calculated for the sandstone intervals and do not reflect the mudstone intervals.

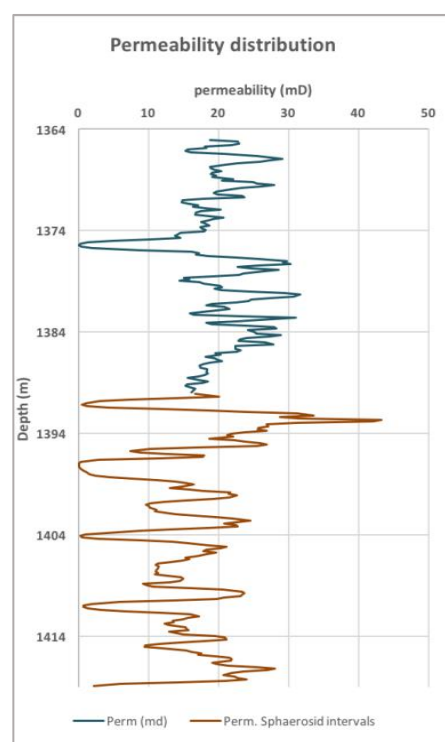


Figure 81: Permeability distribution with separation between the zones with and without sphaerosiderites and rhombohedral cement.

		Hammerfest Basin 7122/6-2	Bjarmeland Platform 7226/2-1	Influence on the reservoir quality
INITIAL COMPOSITION	QUARTZ	Abundant: 26,8%	Abundant: 39,73%	☒ Resistant to mechanical compaction
	ROCK FRAGMENTS	Small: 5,8%	Moderate: 11,2%	☒ Early dissolution preserve feldspar from dissolution (less kaolinite) ☒ Ductile response to compaction
	VOLCANIC DEPOSITS	Moderate	Low	☒ Enhances the development of clay minerals in the pore space and smectite coating.
	MICAS	Low: 1,73 % (higher in mudstones intervals)	Low: 0,8%	☒ Ductile response to compaction ☒ Source of pseudomatrix chlorite ☒ Enhances quartz cementation
AUTHIGENIC MINERALS	CHLORITE COATINGS	Absent or partial	Abundant and continuous	☒ Preserves porosity by inhibiting quartz cementation
	CALCITE CEMENT	Small: 5,5%	Moderate: 22%	☒ Reduces porosity in cemented interval ☒ Produces barriers to fluid flow, inhibiting grain dissolution
	DOLOMITE	Moderate: 22%	Absent	☒ Destroys porosity and permeability
	SPHAEROSIDERITES SIDERITE CEMENT	Absent	Small (Lower core)	☒ Reduces slightly the porosity ☒ Prevents extensive chlorite platelets
			4%	☒ Acts as support during compact and avoid part of the pressure-dissolution of grains. ☒ Reduces permeability
	ILLITE	Small: 5%	Very small: 2%	☒ Reduces permeability ☒ Enhances quartz cementation
QUARTZ CEMENT	Small: 4%	Very small: 1,9%	☒ Destroys porosity	
TEXTURE	GRAIN SIZE	Very-fine sandstone / mudstone	Fine to medium sandstone	☒ Small grain size decreases compressibility of the rock hence compaction. ☒ Mudstones compact intensely with small burial
	IGV	Very high >40% (max 51%)	High 22-47% (av.33%)	☒ Post compaction porosity, reveals the degree of influence of authigenic mineral phases on reservoir quality
	MECHANICAL COMPACTION	No data	Moderate: 4-22% (av.17%)	☒ Loss of initial porosity due to the mechanical compaction
	CHEMICAL COMPACTION	High: 40%	Moderate: 4-31% (av.32%)	☒ Loss of initial porosity due to the chemical compaction
	MATRIX INFLUENCE ON INITIAL POROSITY LOSS	Very high: 59%	Moderate: 22%	☒ Matrix (clay) increases the rock compressibility (more friction between grains). ☒ Reduces porosity
	AVERAGE TOTAL POROSITY	Small 5%	Moderate 12%	☒ Actual porosity available for hydrocarbon storage
	APPARENT PERMEABILITY	Very Small	Moderate	☒ Actual permeability available for fluid flow
RESERVOIR EVALUATION		POOR	MODERATE	Possible gas reservoir

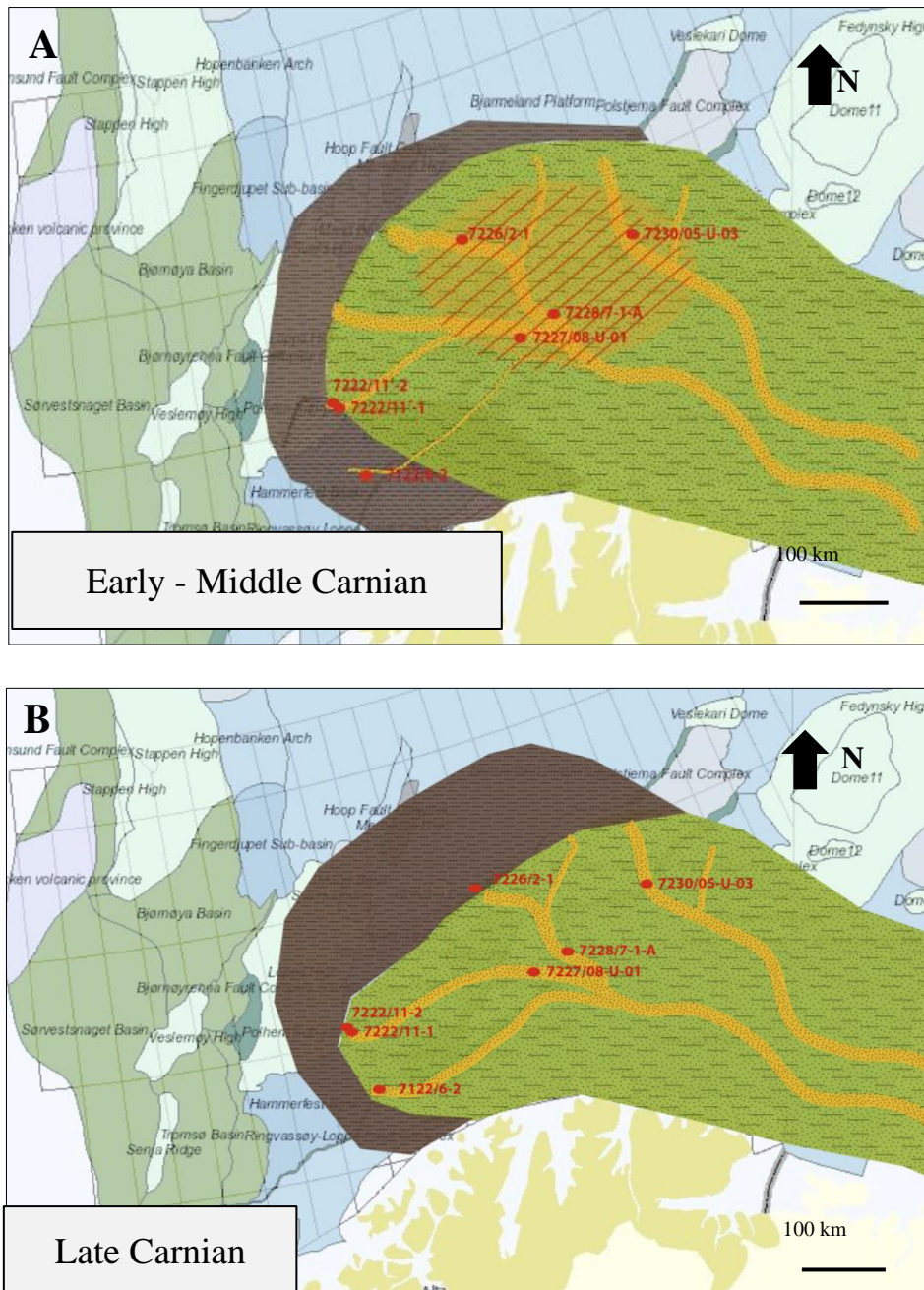
6.4 Geographical extent of the Snadd Formation reservoir quality

The Snadd Formation has been the subject of many studies, in term of depositional environment, climate reconstruction, but also reservoir quality. The thick sandstones packages are a common characteristic observed in many places in the Barents Sea: Loppa high, Bjarmeland platform, Fingerdjupet basin and Nordkapp basin (Line, 2015; Stensland, 2012; Auset, 2012). Those thick sandstones have, in general, good reservoir potential with considerable conserved porosity post mechanical compaction due to chlorite coating.

The presence of the sphaerosiderites concretions could be linked with low mechanical compaction effect, therefore lower quartz cementation. They are a feature observed fairly consistently in the Early Carnian sandstones, notably in the Nordkapp Basin (Auset, 2012, Line, 2015) (Fig. 82). These siderites are not observed in all the provinces of the Snadd formation. In the Loppa high siderite is observed as cement and associated with kaolinite are the main cause of porosity and permeability depletion from chemical compaction (Gyenis, 2016; Line, 2015).

The Early – Middle Carnian deposits seem to have a better reservoir potential than the Late Carnian deposits in the east whereas the Late Carnian deposits seems to be leading in the west. This is to replace in the climatic conditions changing during the Triassic and particularly the shift from regression to transgression at its onset during the Late Carnian (Klausen et al., 2015; Worsley, 2008). This transgression will bring more mud in the deposits reducing their reservoir potential in the south-western Barents Sea. Moreover, the climatic conditions also change and become more humid enhancing the weathering and degrading more of the reservoir potential.

The upper part of the Late-Carnian deposits of the well 7122/6-2 is composed of nice sandstone deposits similar to the ones of the Early Carnian deposits (well 7226/2-1). Same characteristics are found in the Late Carnian deposits of the wells 7222/11-1 and 7222/11-2 on the southern Bjarmeland platform (Fig.82). The shift in the sandstones packaging from west to east seems to indicate a change of the progradation direction of the delta system within the Carnian (Fig.82).



Well name	Age of the cored Snadd Formation
7122/6-2	Late Carnian
7222/11-1	Late Carnian
7222/11-2	Ladinian-Carnian
7226/2-1	Early Carnian
7227/08-U-01	--- not found---
7228/08-U-02	Early Carnian
7230/05-U-03	Ladinian

Figure 82: Maps reconstructed the possible depositional environments from the Snadd Fm in southwestern Barents Sea for the middle Carnian (A) to Late Carnian (B). The origin of the channels is inspired from Klausen et al (2015) and Glørstad et al (2010). The striped area refers to the main observation site of sphaerosiderites grains, and values only for the Early-Middle Carnian. The brown area represents the area influenced by tides whereas the green constitutes the coastal/flood plain environments disturbed by channel in yellow.

VII. Conclusion:

The reservoir quality of the Snadd Formation in the studied locations show poor potential for oil, but the deposits of the Bjarmeland platform reveal a moderate to good potential as a gas reservoir. The following conclusions about the reservoir characterization of the Snadd Formation can be established:

- The depositional environments are decisive when considering the potential of a reservoir. The well 7122/6-2 loses all its potential due to the high content of mud in the depositional environment, deposited as matrix. The higher amount of volcanic derived sediments in the well 7122/6-2 of the Hammerfest Basin, associated with a smaller transport distance, lead to the extensive alteration of the volcanic sediments. Those alteration leads to the formation of cement as these sediments were precursors for pore filling authigenic clay minerals.
- The grain-supported intervals of well 7122/6-2, developed poor reservoir quality due the large amount of matrix but also from the chemical compaction. Illitization and quartz cement destroyed the porosity and permeability. The presence of quartz cement is partly due to large amount of mica and illite enhancing the cementation. The higher temperature range and lack of chlorite coating explained the extensive quartz cementation. This low potential is reinforced by the presence of the dolomite intervals presenting burial diagenetic neomorphism destroying the possible gain in porosity in early diagenesis dolomitization.
- The fluvial sandstones of the well 7226/2-1 show a better potential with a normal porosity loss from mechanical compaction and a low influence of chemical compaction. The chemical compaction is reduced due to effective chlorite coating inhibiting quartz cementation preserving the residual porosity of the deposits. Nevertheless, the authigenic chlorite platelets associated with the coating reduce the permeability of some samples as they grow extensively and fill the pore space.
- The presence of sphaerosiderites in the well 7226/2-1, even if it reduces slightly the porosity, might inhibit the extensive growth of chlorite platelets in the deepest half of the core. However, they are also associated with a small reduction in permeability

- The sphaerosiderites and associated rhombohedral cement counteract the effect of mechanical compaction reducing it to 4% of porosity reduction in the lower part of the core 7226/2-1. Their soft deformation can undergo more pressure without breaking of the grains as the pressure is acting on a greater surface area. Their presence will lead to less fracturing of the framework grains and therefore less fresh surface area available for quartz cementation.
- The interpreted channel deposits of the Bjarmeland Platform, well 7226/2-1, make it a good reservoir for gas purposes as the stacked point bar deposits formed a 60m thick unit. The assessment of the lateral stacking patterns requires more than one well to be made. From this study the stacking is believed to be short lived since the marine transgression ended the sandstone deposition in the Late Carnian.
- The abundance of lithic fragments in the Bjarmeland Platform affects the reservoir quality by two opposite roles. In early diagenesis, they reduce the porosity by allowing more mechanical compaction as they desegregate, but with depth they will reduce the rock fracturing therefore reduce the quartz cementation. The long grain contact type resulting from the mechanical compaction will lead to reduced permeability. The early dissolution of lithic fragments will delay the dissolution of feldspars and associated precipitation of kaolinite in the pore space. However, their dissolution by meteoric leaching in early diagenesis produce authigenic chlorite.
- The calcite cemented intervals observed in the Bjarmeland Platform might act as a barrier to the fluid flow. They prevent the dissolution of feldspars and precipitation of kaolinite and therefore preserve the porosity from chemical compaction in the underlying beds. This hypothesis is valid if the calcite layers are laterally continuous.
- The study of the deposits in both wells reveals a tidal influence increasing towards the end of the Carnian, resulting in reduction in reservoir quality. For the Snadd formation. The Early Carnian owns a better potential. The difference in reservoir quality between the wells is mostly due to a difference in depositional environments and matrix content. The greater burial depth and associated chemical compaction of the well 7122/6-2 also explains the poor quality found.

Further work :

The potential of the Early Carnian deposits on the Bjarmeland Platform might be worth using more well data to estimate the stacking pattern and lateral extend of the channel deposits. The transgression taking place in the Late Carnian might have created seals through shale deposition and create good potential to develop gas reservoirs.

References:

- Aagaard, P., Jahren, J. S., Harstad, A. O., Nilsen, O., & Ramm, M.** (2000). Formation of grain-coating chlorite in sandstones. Laboratory synthesized vs. natural occurrences. *Clay Minerals*, 35(1), 261-261.
- Aagaard, P., Egeberg, P. K., Saigal, G. C., Morad, S., & Bjorlykke, K.** (1990). Diagenetic Albitization of Detrital K-Feldspars in Jurassic, Lower Cretaceous and Tertiary Clastic Reservoir Rocks from Offshore Norway, II. Formation Water Chemistry and Kinetic Considerations. *Journal of sedimentary Research*, 60(4).
- Adams, a. e., Mackenzie, w. s., & Guilford, c.** (1984). *Atlas of sedimentary rocks under the microscope*. Longman; Wiley.
- Ali, S. A., Clark, W. J., Moore, W. R., & Dribus, J. R.** (2010). Diagenesis and reservoir quality. *Oilfield Review*, 22(2), 14-27.
- Anjos, S. M. C., De Ros, L. F., & Silva, C. M. A.** (2003). Chlorite authigenesis and porosity preservation in the Upper Cretaceous marine sandstones of the Santos Basin, offshore eastern Brazil: International Association of Sedimentology Special Publication 34. *Clay Mineral Cements in Sandstones. International Association of Sedimentologists, Special Publication*, 34, 291-316.
- Auset, M.** (2012). Sedimentology and Diagenesis of Upper Triassic Sandstones, with Emphasis on the Snadd-Fruholmen Transition, Barents Sea.
- Baig, I., Faleide, J. I., Jahren, J., & Mondol, N. H.** (2016). Cenozoic exhumation on the southwestern Barents Shelf: Estimates and uncertainties constrained from compaction and thermal maturity analyses. *Marine and Petroleum Geology*, 73, 105-130.
- Baker, P. A., & Kastner, M.** (1981). Constraints on the Formation of sedimentary dolomite. *Science*, 213(4504), 214-216.
- Beard, D. C., & Weyl, P. K.** (1973). Influence of texture on porosity and permeability of unconsolidated sand. *AAPG bulletin*, 57(2), 349-369.
- Berglund, L. T., Augustson, J., Færseth, R., Gjelberg, J., & Ramberg-Moe, H.** (1986). The evolution of the Hammerfest Basin. *Habitat of hydrocarbons on the Norwegian continental shelf*, 319-338.
- Berner, R. A.** (1981). Authigenic mineral formation resulting from organic matter decomposition in modern sediments. *Fortschritte der mineralogie*, 59(1), 117-135.
- Bjørlykke, K., Ramm, M., & Saigal, G. C.** (1989). Sandstone diagenesis and porosity modification during basin evolution. *Geologische Rundschau*, 78(1), 243-268.
- Bjørlykke, K., & Egeberg, P. K.** (1993). Quartz cementation in sedimentary basins. *AAPG bulletin*, 77(9), 1538-1548.

- Bjørlykke, K.** (1998). Clay mineral diagenesis in sedimentary basins—a key to the prediction of rock properties. Examples from the North Sea Basin. *Clay minerals*, 33(1), 15-34.
- Bjørlykke, K.** (2010). *Petroleum Geoscience: From sedimentary environments to rock physics*. Springer Berlin Heidelberg.
- Bjørlykke, K.** (2015). *Petroleum Geoscience: From sedimentary environments to rock physics*. second edition. Springer Berlin Heidelberg.
- Bjørlykke, K., & Jahren, J.** (2010). Sandstones and sandstone reservoirs. In *Petroleum Geoscience* (pp. 119-149). Springer Berlin Heidelberg.
- Bjørkum, P. A., & Nadeau, P. H.** (1998). Temperature controlled porosity/permeability reduction, fluid migration, and petroleum exploration in sedimentary basins. *Australian Petroleum Production and Exploration Association Journal*, 38, 453-464.
- Bloch, S., Lander, R. H., & Bonnell, L.** (2002). Anomalously high porosity and permeability in deeply buried sandstone reservoirs: Origin and predictability. *AAPG bulletin*, 86(2), 301-328.
- Bue, E. P., & Andresen, A.** (2014). Constraining depositional models in the Barents Sea region using detrital zircon U–Pb data from Mesozoic sediments in Svalbard. *Geological Society, London, Special Publications*, 386(1), 261-279.
- Chuhan, F. A., Kjeldstad, A., Bjørlykke, K., & Høeg, K.** (2002). Porosity loss in sand by grain crushing—Experimental evidence and relevance to reservoir quality. *Marine and Petroleum Geology*, 19(1), 39-53.
- Chuhan, F. A., Kjeldstad, A., Bjørlykke, K., & Høeg, K.** (2003). Experimental compression of loose sands: relevance to porosity reduction during burial in sedimentary basins. *Canadian Geotechnical Journal*, 40(5), 995-1011.
- Compton, R. R.** (1962). Manual of field geology. *Soil Science*, 93(4), 295.
- Dalrymple, R. W., & James, N. P.** (Eds.). (2010). *Facies Models 4*. Geological Association of Canada.
- Doebelin, N., & Kleeberg, R.** (2015). Profex: a graphical user interface for the Rietveld refinement program BGMN. *Journal of applied crystallography*, 48(5), 1573-1580.
- Doré, A. G.** (1995). Barents Sea geology, petroleum resources and commercial potential. *Arctic*, 207-221.
- Dunn, T. L.** (1992). Infiltrated materials in cretaceous volcanogenic sandstones, San Jorge Basin, Argentina.
- Ehrenberg, S. N.** (1993). Preservation of anomalously high porosity in deeply buried sandstones by grain-coating chlorite: examples from the Norwegian continental shelf. *AAPG Bulletin*, 77(7), 1260-1286.
- Faleide, J. I., Gudlaugsson, S. T., & Jacquart, G.** (1984). Evolution of the western Barents Sea. *Marine and Petroleum Geology*, 1(2), 123IN1129IN5137-128IN4136IN8150.
- Folk, R. L., & Ward, W. C.** (1957). Brazos River bar: a study in the significance of grain size

- parameters. *Journal of Sedimentary Research*, 27(1).
- Folk, R. L.** (1974). *Petrology of Sedimentary Rocks: The University of Texas, Geology 370 K, 383 L, 383 M*. Hemphill.
- Gabrielsen, R. H., & Færseth, R. B.** (1989). The inner shelf of North Cape, Norway and its implications for the Barents Shelf-Finnmark Caledonide boundary. A comment. *Norsk geologisk tidsskrift*, 69, 57-62.
- Gabrielsen, R. H., Faerseth, R. B., & Jensen, L. N.** (1990). *Structural Elements of the Norwegian Continental Shelf. Pt. 1. The Barents Sea Region*. Norwegian Petroleum Directorate.
- Gehring, A. U.** (1990). Diagenesis of ferriferous phases in the Northampton ironstone in the Cowthick quarry near Corby (England). *Geological Magazine*, 127(2), 169-176.
- Glørstad-Clark, E., Faleide, J. I., Lundschie, B. A., & Nystuen, J. P.** (2010). Triassic seismic sequence stratigraphy and paleogeography of the western Barents Sea area. *Marine and Petroleum Geology*, 27(7), 1448-1475.
- Glørstad-Clark, E., Birkeland, E. P., Nystuen, J. P., Faleide, J. I., & Midtkandal, I.** (2011). Triassic platform-margin deltas in the western Barents Sea. *Marine and Petroleum Geology*, 28(7), 1294-1314.
- Gyenis, T.** (2016). Reservoir quality of the Triassic Snadd and Kobbe Formations in the Barents Sea. DUO.UIO
- Hanken, N. M., Bjørlykke, K., & Nielsen, J. K.** (2010). Carbonate sediments. In *Petroleum Geoscience* (pp. 151-216). Springer Berlin Heidelberg.
- Høy, T., & Lundschie, B. A.** (2011). Triassic deltaic sequences in the northern Barents Sea. *Geological Society, London, Memoirs*, 35(1), 249-260.
- Houseknecht, D. W.** (1987). Assessing the relative importance of compaction processes and cementation to reduction of porosity in sandstones. *AAPG bulletin*, 71(6), 633-642.
- Hurst, A., & Nadeau, P. H.** (1995). Clay microporosity in reservoir sandstones: an application of quantitative electron microscopy in petrophysical evaluation. *AAPG bulletin*, 79(4), 563-573.
- Jahren, J. S., & Aagaard, P.** (1989). Compositional variations in diagenetic chlorites and illites, and relationships with formation-water chemistry. *Clay Minerals*, 24(2), 157-170.
- Johansen, S. E., Ostist, B. K., Birkeland, Ø., Fedorovsky, Y. F., Martirosjan, V. N., Christensen, O. B., ... & Margulis, L. S.** (1992). Hydrocarbon potential in the Barents Sea region: play distribution and potential. *Arctic Geology and Petroleum Potential, Norwegian Petroleum Society (NPF), Special Publication*, 2, 273-320.
- Klausen, T. G., Ryseth, A. E., Helland-Hansen, W., Gawthorpe, R., & Laursen, I.** (2015). Regional development and sequence stratigraphy of the Middle to Late Triassic Snadd Formation, Norwegian Barents Sea. *Marine and Petroleum Geology*, 62, 102-122.

- Koochak Zadeh, K. M., Mondol, N. H., & Jahren, J.** (2016). Experimental mechanical compaction of sands and sand–clay mixtures: a study to investigate evolution of rock properties with full control on mineralogy and rock texture. *Geophysical Prospecting*, 64(4), 915-941.
- Krajewski, K. P., & Wozny, E.** (2009). Origin of dolomite-ankerite cement in the Bravaisberget Formation (Middle Triassic) in Spitsbergen, Svalbard. *Polish Polar Research*, 30(3), 231-248.
- Lee, Y. I., & Friedman, G. M.** (1987). Deep-burial dolomitization in the Ordovician Ellenburger Group carbonates, west Texas and southeastern New Mexico. *Journal of Sedimentary Research*, 57(3).
- Line, L.H.** (2015). Reservoir characterization of the Middle - Upper Triassic Kobbe and Snadd Formations in the southwestern Barents Sea: The role of chlorite coating. *Master thesis. DUO UIO*.
- Longman, M. W.** (1982). *Carbonate Diagenesis as a Control on Stratigraphic Traps: With Examples from the Williston Basin* (No. 21). Amer Assn of Petroleum Geologists.
- Lucia, F. Jerry, Charles Kerans, and James W. Jennings Jr.** "Carbonate reservoir characterization." *Journal of petroleum technology* 55.06 (2003): 70-72.
- Luo, J. L., Morad, S., Salem, A., Ketzer, J. M., Lei, X. L., Guo, D. Y., & Hlal, O.** (2009). Impact of diagenesis on reservoir-quality evolution in fluvial and lacustrine-deltaic sandstones: evidence from Jurassic and Triassic sandstones from the ordos basin, china. *Journal of Petroleum Geology*, 32(1), 79-102.
- Maast, T. E.** (2013). *Reservoir quality of deeply buried sandstones—a study of burial diagenesis from the North Sea* (Doctoral dissertation, University of Oslo Norway).
- Matlack, K. S., Houseknecht, D. W., & Applin, K. R.** (1989). Emplacement of clay into sand by infiltration. *Journal of Sedimentary Research*, 59(1).
- Mondol, N. H.** (2015). Introduction to well logs. In *Petroleum Geoscience*. Springer Berlin Heidelberg.
- Morad, S., Ketzer, J. R. M., & De Ros, L. F.** (2000). Spatial and temporal distribution of diagenetic alterations in siliciclastic rocks: implications for mass transfer in sedimentary basins. *Sedimentology*, 47(s1), 95-120.
- Mørk, M. B. E.** (1999). Compositional variations and provenance of Triassic sandstones from the Barents Shelf. *Journal of Sedimentary Research*, 69(3), 690-710.
- Mozley, P. S.** (1989). Relation between depositional environment and the elemental composition of early diagenetic siderite. *Geology*, 17(8), 704-706.
- Nagtegaal, P. J. C.** (1978). Sandstone-framework instability as a function of burial diagenesis. *Journal of the Geological Society*, 135(1), 101-105.
- Nichols, G.** (2009). *Sedimentology and stratigraphy*. John Wiley & Sons.
- Paxton, S. T., Szabo, J. O., Ajdukiewicz, J. M., & Klimentidis, R. E.** (2002). Construction of an

- intergranular volume compaction curve for evaluating and predicting compaction and porosity loss in rigid-grain sandstone reservoirs. *AAPG bulletin*, 86(12), 2047-2067.
- Powers, M. C.** (1953). A new roundness scale for sedimentary particles. *Journal of Sedimentary Research*, 23(2).
- Pye, K., Dickson, J. A. D., Schiavon, N., Coleman, M. L., & Cox, M.** (1990). Formation of siderite-Mg-calcite-iron sulphide concretions in intertidal marsh and sandflat sediments, north Norfolk, England. *Sedimentology*, 37(2), 325-343.
- Rahimpour-Bonab, H., Esrafil-Dizaji, B., & Tavakoli, V.** (2010). Dolomitization and Anhydrite Precipitation in Permo-Triassic Carbonates at the South Pars Gasfield, Offshore Iran: Controls on Reservoir Quality. *Journal of Petroleum Geology*, 33(1), 43-66.
- Riis, F., Lundschie, B. A., Høy, T., Mørk, A., & Mørk, M. B. E.** (2008). Evolution of the Triassic shelf in the northern Barents Sea region. *Polar Research*, 27(3), 318-338.
- Rodrigues, A. G., De Ros, L. F., Neumann, R., & Borghi, L.** (2015). Paleoenvironmental implications of early diagenetic siderites of the Paraíba do Sul Deltaic Complex, eastern Brazil. *Sedimentary Geology*, 323, 15-30.
- Rude, P. D., & Aller, R. C.** (1989). Early diagenetic alteration of lateritic particle coatings in Amazon continental shelf sediment. *Journal of Sedimentary Research*, 59(5).
- Saigal, G. C., & Bjørlykke, K.** (1987). Carbonate cements in clastic reservoir rocks from offshore Norway—relationships between isotopic composition, textural development and burial depth. *Geological Society, London, Special Publications*, 36(1), 313-324.
- Salem, A. M., Morad, S., Mato, L. F., & Al-Aasm, I. S.** (2000). Diagenesis and reservoir-quality evolution of fluvial sandstones during progressive burial and uplift: Evidence from the Upper Jurassic Boipeba Member, Reconcavo Basin, Northeastern Brazil. *AAPG bulletin*, 84(7), 1015-1040.
- Santin, C. E., Abel, M., Goldberg, K., & De Ros, L. F.** (2009) PS Automatic Detection of the Degree of Compaction in Reservoir Rocks Based on Visual Knowledge.
- Scotese, C. R., Gahagan, L. M., & Ross, M. I.** (1987). Phanerozoic plate tectonic reconstructions. Paleooceanographic mapping project. *Institute for Geophysics, University of Texas, Technical Report*, 90.
- Skjold, L. J.** (1998). Triassic sequence stratigraphy of the southwestern Barents Sea.
- Stensland, H.** (2012). Sedimentology and Diagenesis of the Triassic Snadd Formation in the Barents Sea. *Master thesis*.
- Talleraas, E.** (1979). The Hammerfest basin—an aulacogen. In *Norwegian Sea Symposium, Norwegian Petroleum Society, Tromsø* (Vol. 18, pp. 1-13).
- Torskaya, T. S., Jin, G., & Torres-Verdin, C.** (2007, January). Pore-level analysis of the relationship between porosity, irreducible water saturation, and permeability of clastic rocks. In *SPE Annual Technical Conference and Exhibition*. Society of Petroleum Engineers.

- Walderhaug, O.** (1996). Kinetic modeling of quartz cementation and porosity loss in deeply buried sandstone reservoirs. *AAPG bulletin*, 80(5), 731-745.
- Weibel, R., Lindström, S., Pedersen, G. K., Johansson, L., Dybkjær, K., Whitehouse, M. J., ... & Leng, M. J.** (2016). Groundwater table fluctuations recorded in zonation of microbial siderites from end-Triassic strata. *Sedimentary Geology*, 342, 47-65.
- Wentworth, C. K.** (1922). A scale of grade and class terms for clastic sediments. *The Journal of Geology*, 30(5), 377-392.
- Wilson, M. D., & Pittman, E. D.** (1977). Authigenic clays in sandstones: recognition and influence on reservoir properties and paleoenvironmental analysis. *Journal of Sedimentary Research*, 47(1).
- Worden, R. H., & Burley, S. D.** (2003). Sandstone diagenesis: the evolution of sand to stone. *Sandstone Diagenesis: Recent and Ancient*, 4, 3-44.
- Worden, R. H., & Morad, S.** (2003). Clay minerals in sandstones: controls on formation, distribution and evolution. *Clay mineral cements in sandstones*, 1-41.
- Worsley, D.** (2008). The post-Caledonian development of Svalbard and the western Barents Sea. *Polar Research*, 27(3), 298-317.
- Ziegler, A. M., Parrish, J. M., Jiping, Y., Gyllenhaal, E. D., Rowley, D. B., Parrish, J. T., ... & Hulver, M. L.** (1994). Early Mesozoic phytoгеography and climate. In *Palaeoclimates and their Modelling* (pp. 89-97). Springer Netherlands.

APPENDICES

APPENDIX 1: WELL DATABASE

Table 1: Summary of the well database used in this thesis (from NPD, 2016)

Formation	Well	Core Nb	Logged interval(s) (m)	Total length (m)	Sample Nb	Location
Snadd	7122/6-2	1	2452 - 2506	54	18	Hammerfest Basin
Snadd	7226/2-1	1	1365 - 1418	53	18	Bjarmeland Platform

Table 2: Coordinates (degrees and UTM) of the well database

Well	Coordinates (Degrees)	Coordinates (UTM)	Location
7122/6-2	NS: 71° 35' 13.6" N EW: 22° 51' 21.54" E	NS: 7944100.00 EW: 565425.04	Hammerfest Basin
7226/2-1	NS: 72° 53' 31.6" N EW: 26° 35' 39.5" E	NS: 8088712.12 EW: 486678.61	Bjarmeland Platform

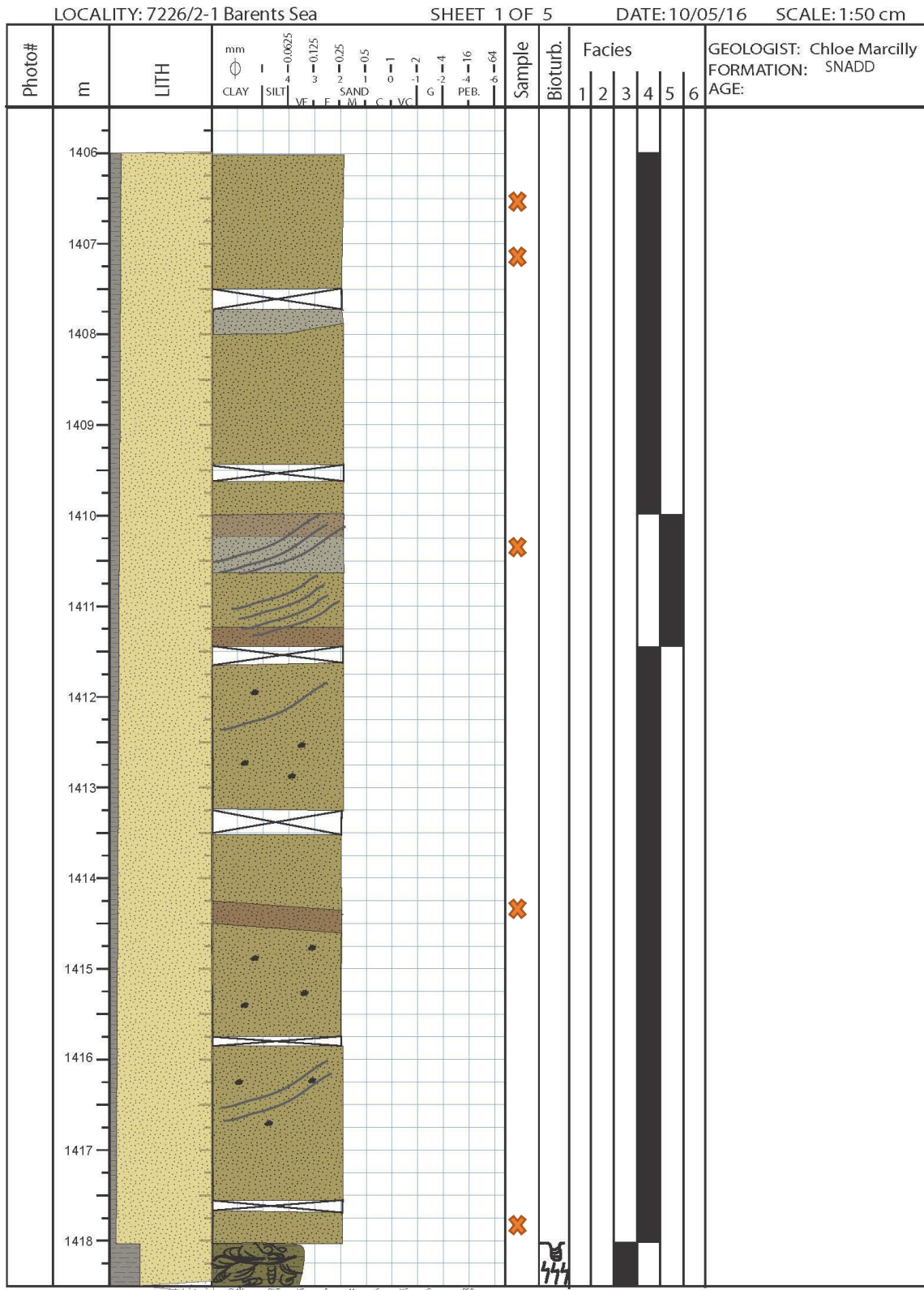
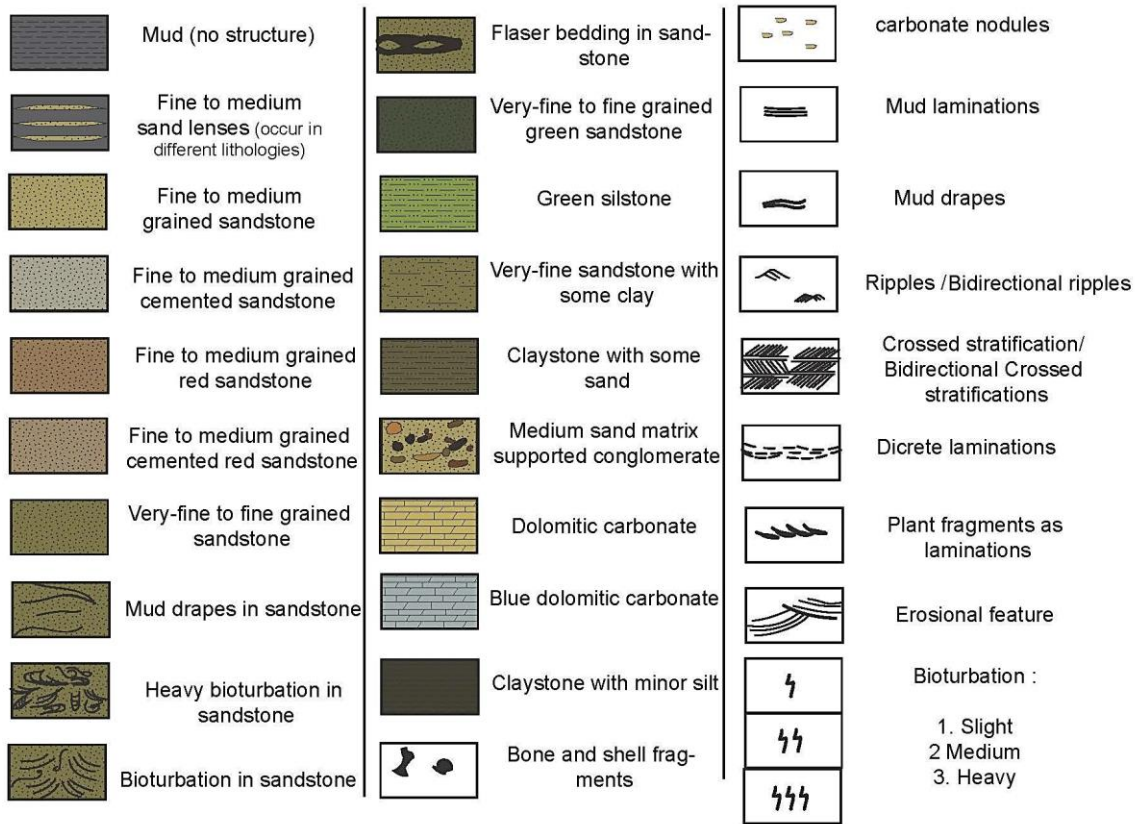


Figure 6: Sedimentary log of the core 7226/2-1 at the scale 1:50cm. Page 1 of 5.

Legend for the logs of Core 7226/2-1 and 7122/6-2



A+ responds to acid treatment **HB** Heterolithic bedding **L-WB** Lenticular to wavy bedding **FB** Flaser bedding

Figure 11: Legend for the logs of the well 7122/6-2 and the well 7226/2-1

APPENDIX 3: PETROPHYSICAL DATA

Table 3: Calculated geothermal gradients for the studied wells. The wells are drilled close to vertical.

Well	Total depth (m MD)	Total depth (m TVD)	Water depth (m)	Kelly brushing elevation (m)	Bottom hole temperature (°C)	Geothermal gradient (°C/Km)
7122/6-2	3070	3070	408	23	100	36
7226/2-1	2992	2991	347	23	96 (estimated from other wells)	34

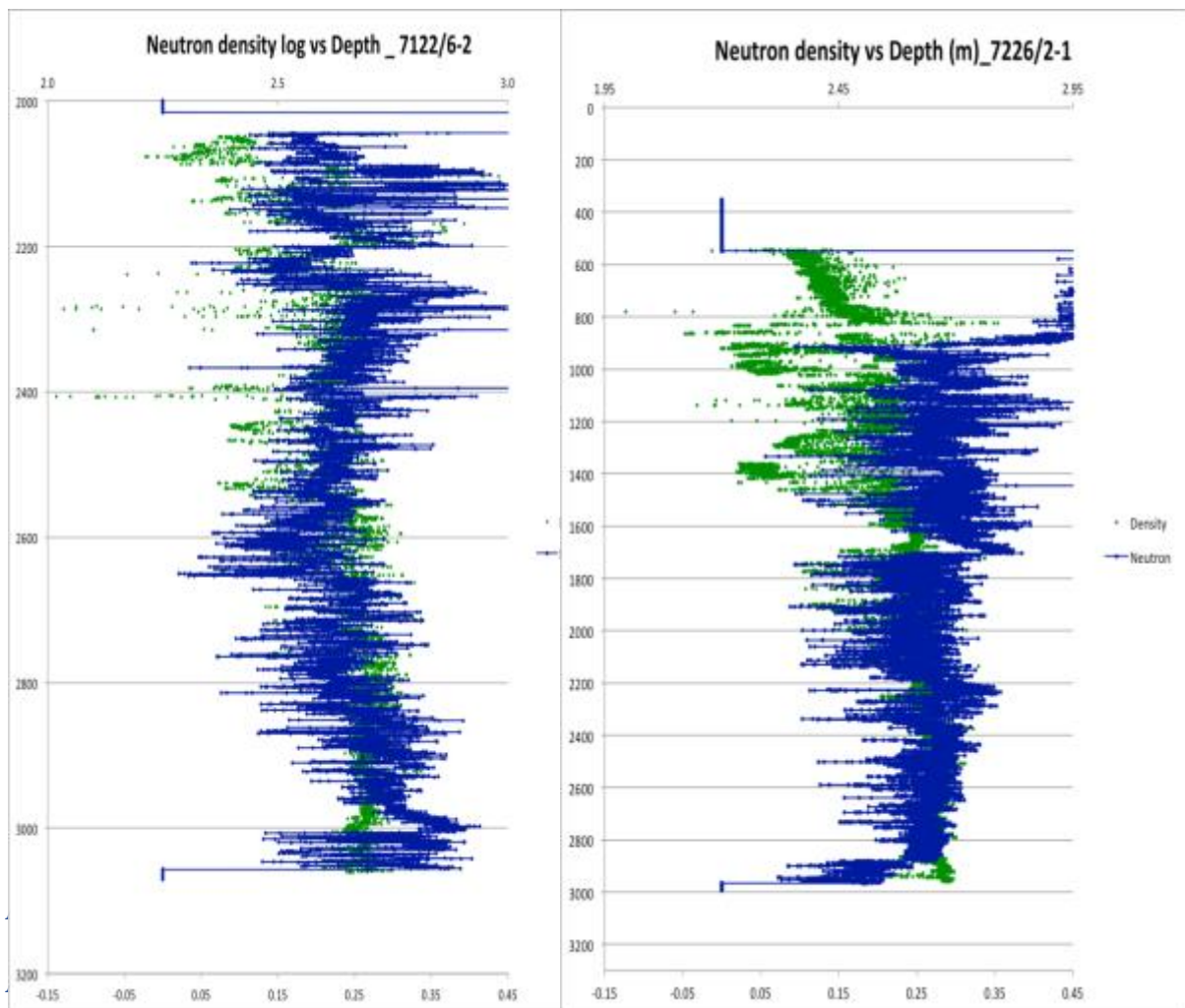


Figure 12: Neutron-density log for the well 7122/6-2 and the well 7226/2-1.

APPENDIX 4: PETROGRAPHICAL DATA

Table 4: Studied samples for the petrographic analysis of the Snadd Formation for the well 7122/6-2. BX: bulk XRD, CFX: clay fraction XRD, PC: point counting, S: SEM.

Well	Sample number	Depth (m)	Facies	Petrographic investigations			
				BX	CFX	PC	S
7122/6-2	W1S1	2452,6	F4				
	W1S2	2456,65	F4				
	W1S3	2458,48	F2				
	W1S4	2463,65	F3				
	W1S5	2465,55	F3				
	W1S6	2468,6	F3				
	W1S7	2471,35	F7				
	W1S8	2473,4	F7				
	W1S9	2476,35	F7				
	W1S10	2481,7	F3				
	W1S11	2484,65	F4				
	W1S12	2487,4	F3				
	W1S13	2489,7	F3				
	W1S14	2492,65	F3				
	W1S15	2496,65	F1				
	W1S16	2499,95	F1				
	W1S17	2503,65	F3				
	W1S18	2506,15	F4				

Table 5: Studied samples for the petrographic analysis of the Snadd Formation for the well 7226/2-1. BX: bulk XRD, CFX: clay fraction XRD, PC: point counting, S: SEM.

Well	Sample number	Depth (m)	Facies	Petrographic investigations			
				BX	CFX	PC	S
7226/2-1	W2S1	1365,9	F5				
	W2S2	1368,7	F5				
	W2S3	1374,7	F5				
	W2S4	1376,4	F5				
	W2S5	1378,15	F5				
	W2S6	1381,2	F5				
	W2S7	1384,6	F5				
	W2S8	1388,6	F4				
	W2S9	1390,8	F5				
	W2S10	1394,6	F5				
	W2S11	1396,6	F5				
	W2S12	1398,6	F5				
	W2S13	1403,2	F4				
	W2S14	1406,6	F4				
	W2S15	1407,2	F4				
	W2S16	1410,35	F5				
	W2S17	1414,4	F4				
	W2S18	1417,8	F4				

APPENDICES

Table 6: Point counting results for the detrital grains for the well 7122/6-2. All the values are expressed in percentage of total volume per sample.

Sample	Detrital grains											Mica	Matrix
	Quartz		Feldspar		Rock fragments								
	Mono	poly	Plagio	Micro	Chert	Epiclast	Lithic	Schistose	Shale fragment	Non-ID			
W1S1	17,9	5,1	6,2	1,0	7,5	0,5	5,0	1,5	4,0	0,5	3,55	23	
W1S2	19,4	3,2	2,5	0,2	0,0	0,0	2,5	1,0	2,0	0,3	3,2	30	
W1S3													
W1S4													
W1S5	23,9	1,8	3,2	1,5	1,5	0,0	1,0	0,8	0,0	0,0	1	52	
W1S6													
W1S7													
W1S8													
W1S9													
W1S10													
W1S11	22,8	3,4	5,0	0,5	2,0	0,0	0,3	0,3	0,3	0,0	2,5	36	
W1S12	32,6	2,5	3,3	2,0	3,0	0,5	0,3	0,8	0,0	0,0	1	28	
W1S13	21,6	4,4	3,7	2,0	8,7	0,0	2,6	0,8	0,0	0,0	1,3	49	
W1S14													
W1S15													
W1S16													
W1S17	29,1	1,9	1,8	2,0	1,3	0,3	1,6	0,3	0,0	0,0	0,5	67	
W1S18	21,5	3,2	4,2	0,3	5,0	0,0	0,5	0,3	0,0	0,0	0,75	19	

APPENDICES

Table 7: Point counting results for the detrital grains for the well 7226/2-1. All the values are expressed in percentage of total volume per sample.

Sample	Detrital grains											
	Quartz		Feldspar		Rock fragments						Mica	Matrix
	Mono	poly	Plagio	Micro	Chert	Epiclast	Lithic	Schistose	Shale fragment	Non-ID		
W2S1	37,7	10,0	5,0	2,5	1,1	0,0	2,0	2,3	0,0		1	11
W2S2	34,4	6,6	6,1	3,7	3,3	1,0	2,2	1,7	3,1		1,5	8
W2S3	33,5	5,5	5,3	2,0	1,3	0,1	2,5	0,5	3,5		0	9
W2S4	34,8	8,2	5,5	1,7	0,8	0,0	4,5	0,0	0,0		1,5	14
W2S5	39,2	9,8	4,1	1,7	1,8	0,1	7,5	0,3	1,0		0	12
W2S6	34,7	3,9	5,5	2,2	0,0	0,0	1,6	3,9	0,0		2,2	19
W2S7	37,8	6,7	4,8	1,0	1,8	0,0	6,3	0,0	1,0		0,8	17
W2S8	35,8	5,4	4,8	3,7	6,0	0,0	3,3	1,5	0,0		1,5	16
W2S9	31,6	4,7	4,3	2,0	5,1	0,0	2,3	0,0	1,4		0,2	10
W2S10	38,4	4,8	3,0	2,0	1,3	0,1	4,8	2,8	0,0		0,5	21
W2S11	29,2	6,8	2,8	2,8	5,5	0,2	5,0	1,3	2,3		0,2	9
W2S12	33,1	5,4	3,5	2,0	3,7	0,0	1,8	0,0	0,3		0,2	8
W2S13	24,6	7,4	2,3	3,2	1,8	0,1	4,0	3,5	0,0		0,2	3
W2S14	30,1	7,1	3,3	2,5	5,9	0,1	2,3	1,3	0,3		0,2	18
W2S15	30,5	5,0	2,8	1,2	0,1	0,0	2,0	0,0	0,3		1,7	18
W2S16	31,9	3,2	1,5	4,5	6,3	0,2	2,5	2,2	0,7		1	10
W2S17	28,1	5,4	2,5	0,5	0,7	0,0	3,9	0,0	0,8		1	6
W2S18	37,0	7,0	6,7	1,3	6,4	0,1	2,3	2,0	1,0		1,2	7

APPENDICES

Table 8: Point counting results for the authigenic and textural results for the well 7122/6-2. All the values are expressed in percentage of total volume per sample.

Sample	Authigenic minerals						Textural analysis	
	Kaolinite	Chlorite		Clay replacing clast	Cement		Porosity	IGV
		Chlorite coating	pseudomatrix		Calcite	Quartz		
W1S1	0,50	2,76	0,25	8,03	2,51	11,04	6,2	37.05
W1S2	0,00	2,01	0,00	7,29	0,00	20,55	8,2	51.3
W1S3								
W1S4								
W1S5	0,00	2,50	0,00	4,25	0,00	1,75	8,5	
W1S6								
W1S7								
W1S8								
W1S9								
W1S10								
W1S11	0,00	1,73	1,73	16,79	0,25	15,25	5,25	44
W1S12	0,00	0,77	0,00	11,23	0,00	9,00	5,3	33.17
W1S13	0,00	1,49	0,00	5,21	0,00	7,50	3	
W1S14								
W1S15								
W1S16								
W1S17	0,00	9,75	0,00	3,75	0,00	0,00	1,5	46.5
W1S18	0,00	0,50	0,00	14,00	13,38	14,37	7,75	47

APPENDICES

Table 9: Point counting results for the authigenic and textural results for the well 7226/2-1. All the values are expressed in percentage of total volume per sample.

Sample	Authigenic minerals						Textural analysis		
	Kaolinite	Chlorite		Clay replacing clast	Cement		Sphaerosiderites	Porosity	IGV
		Chlorite coating	pseudomatrix		Calcite	Quartz			
W2S1	0,0	4,98	1,00	4,73	0,00	0,70	0,5	14,7	26.4
W2S2	0,0	1,00	0,25	5,75	0,00	0,00	0,2	16	22.9
W2S3	0,4	0,00	1,08	7,56	24,20	0,00	0	7,5	29.15
W2S4	0,0	7,61	0,59	3,80	0,00	0,70	0	12,2	28.9
W2S5	0,3	3,00	1,00	7,67	0,00	1,00	0	11,8	23.2
W2S6	0,5	5,23	0,75	7,22	0,00	1,20	0	13	32.65
W2S7	0,0	5,25	3,00	3,75	0,00	0,20	0	11,5	29.45
W2S8	0,0	5,25	0,25	3,00	0,00	0,50	0	11,5	30.25
W2S9	0,0	4,75	0,75	3,50	0,00	0,00	6	12,5	41.45
W2S10	0,0	8,16	0,51	3,83	0,00	0,70	0,5	8,7	33.7
W2S11	0,0	0,52	0,00	5,48	27,25	0,25	0,2	1	35.4
W2S12	0,0	0,00	0,25	5,05	0,00	0,00	22	13	41.5
W2S13	0,0	1,74	0,00	6,96	22,00	0,00	5,5	1,7	40.75
W2S14	0,0	1,50	0,50	3,00	0,00	0,00	10,5	10	37.05
W2S15	0,0	2,27	0,00	2,53	0,00	0,00	7,2	6,7	45.75
W2S16	0,0	0,00	0,50	4,70	21,70	0,00	0,4	6	32.85
W2S17	0,0	0,51	0,25	2,04	0,00	0,00	18,7	7	47.5
W2S18	0,0	0,25	1,00	6,25	0,00	2,50	0	14,1	21.25



















APPENDICES

Table 10: Point counting results for IGV and compactional regimes calculation for the well 7122/6-2.

Samples	Primary porosity (% rock volume)	Cement (% rock volume)				Matrix (% rock volume)	IGV (%rock volume)	Mechanical compaction (% initial porosity (40%))	Chemical compaction (% initial porosity)	Matrix influence (% initial porosity)	Residual porosity (% initial porosity)
		Calcite /quartz cement	Sphaerosiderites	Rhombohedral siderite	Authigenic minerals						
W1S1	6.2	13.6			0.8	16.6	37.1	5.0	34.7	42.4	15.9
W1S2	8.2	20.6			0.0	22.6	51.3	-31.5	52.7	57.8	21.0
W1S3											
W1S4											
W1S5											
W1S6											
W1S7											
W1S8											
W1S9											
W1S10											
W1S11	5.3	15.5			1.8	21.5	44.0	-12.8	39.7	55.1	13.5
W1S12	4.9	9.0			0.0	19.3	33.2	14.9	23.1	49.5	12.5
W1S13											
W1S14											
W1S15											
W1S16											
W1S17	1.5	0.0			0.0	45.0	46.5	-19.2	0.0	115.4	3.8
W1S18	6.8	27.8			0.0	12.5	47.0	-20.5	71.2	32.1	17.3

APPENDICES

Table 11: Point counting results for IGV and compactional regimes calculation for the well 7122/6-2. The yellow stars represent the non-cemented intervals (pure sandstones), orange ones the siderite cemented ones and pink ones the calcite cemented ones.

Samples (m)	Primary porosity (% rock volume)	cement (% rock volume)				Matrix (% rock volume)	IGV (% rock volume)	Mechanical compaction (% initial porosity (40%))	chemical compaction (% initial porosity)	residual porosity (% initial porosity)	matrix influence (% initial porosity)
		Calcite /quartz cement	Sphaerosiderites	Rhombohedral siderite	Authigenic minerals						
W2S1 	14.0	0.7	0.5	0.0	5.0	15.9	26.4	34.0	3.0	15.9	35.0
W2S2 	16.0	0.0	0.2	0.0	1.0	14.6	22.9	42.8	0.5	14.6	40.0
W2S3 	4.7	24.2	0.0	0.0	0.3	0.0	29.2	27.1	60.5	0.0	11.8
W2S4 	12.2	0.7	0.0	0.0	6.5	24.4	28.9	27.8	1.8	24.4	30.5
W2S5 	11.7	1.0	0.0	0.0	2.5	20.5	23.2	42.0	2.5	20.5	29.3
W2S6 	11.7	1.2	0.0	0.0	5.8	35.9	32.7	18.4	3.0	35.9	29.3
W2S7 	11.5	0.2	0.0	0.0	5.3	32.1	29.5	26.4	0.5	32.1	28.8
W2S8 	11.5	0.5	0.0	0.0	5.3	33.3	30.3	24.4	1.3	33.3	28.8
W2S9 	12.5	0.0	6.0	11.2	4.8	17.9	41.5	-3.6	43.0	17.9	31.3
W2S10 	8.7	0.7	0.5	0.0	8.0	40.5	33.7	15.8	3.0	40.5	21.8
W2S11 	0.0	27.5	0.2	0.0	0.5	18.5	35.4	11.5	69.3	18.5	0.0
W2S12 	13.0	0.0	22.0	0.0	0.0	16.7	41.5	-3.8	55.0	16.7	32.5
W2S13 	1.3	22.0	5.5	11.0	1.0	0.0	40.8	-1.9	96.3	0.0	3.1
W2S14 	9.3	0.0	10.5	0.0	1.5	40.5	37.1	7.4	26.3	40.5	23.1
W2S15 	6.7	0.0	7.2	13.0	2.3	42.6	45.8	-14.4	50.5	42.6	16.8
W2S16 	2.8	21.7	0.4	0.0	0.0	20.5	32.9	17.9	55.3	20.5	6.9
W2S17 	6.5	0.0	18.7	16.5	0.5	13.6	47.5	-18.8	88.0	13.6	16.3
W2S18 	14.0	2.5	0.0	0.0	0.3	11.5	21.3	46.9	6.3	11.5	35.0

APPENDICES

Table 12: Bulk XRD results from the well 7122/6-2. The values represented are fractions

Depth (m)	Biotite	Calcite	Calcite mg	Chlorite	dolomite	Illite	Kaolinite	Microcline	Albite	Quartz	Muscovite
2452.6	1.30	2.00	0.90	7.17	0.00	4.10	2.03	5.00	20.00	55.20	2.30
2456.65	0.00	0.73	0.08	4.20	0.09	3.80	1.10	2.50	26.40	49.80	11.30
2458.48	0.60	3.30	2.55	6.02	38.97	4.00	1.50	2.50	9.96	24.50	6.10
2463.65	0.70	0.50	0.00	19.20	0.08	5.30	3.40	1.36	20.10	31.66	17.70
2465.55	0.80	0.40	0.00	5.28	0.30	5.07	7.57	3.47	21.12	31.79	24.20
2468.6	1.20	0.45	0.01	4.90	0.00	4.84	1.50	2.70	19.10	51.10	14.20
2471.35	1.16	0.07	5.40	3.15	71.20	4.08	2.50	2.92	1.53	4.61	3.38
2473,4											
2476.35	1.00	0.10	3.15	2.65	71.00	3.20	2.85	3.10	1.85	8.00	3.10
2481.7	0.70	9.10	0.60	2.50	0.10	3.95	1.95	4.20	15.65	50.00	11.25
2484.65	0.00	2.10	0.00	17.60	0.00	4.00	0.31	4.00	24.52	43.75	3.72
2487.4	0.60	0.90	0.20	5.30	0.40	6.35	1.70	3.60	21.00	45.20	14.75
2489.7	0.00	0.70	0.00	1.00	0.20	5.30	1.00	4.10	24.70	56.80	6.20
2492.65	0.00	2.00	0.00	1.20	0.00	4.40	1.3	2.30	24.90	51.10	12.80
2496.65	1.30	2.20	0.30	3.30	0.20	4.00	1.50	2.80	19.85	54.30	10.25
2499.95	1.55	0.35	0.10	6.00	0.20	4.50	1.3	2.70	20.10	45.50	17.70
2503,65											
2506.15	1.30	14.00	0.70	3.40	0.20	3.70	2.35	3.85	19.60	46.60	4.30

APPENDICES

Table 103: Bulk XRD results from the well 7226/2-1. The values represented are fractions

Depth(m)	Albite	Biotite	Calcite	CalciteMg	Chlorite	Apatite	Illite	Kaolinite	K-Feldspar	Muscovite	Quartz	Siderite	Smectite
1365,9	15,98	0,20	1,13	0,20	9,22	0,20	1,61	0,31	5,42	0,00	53,26	0,51	11,95
1368,7	16,52	0,25	0,33	0,71	4,05	0,51	2,53	0,15	7,24	0,00	58,76	0,12	8,81
1374,7	11,38	0,50	24,77	5,54	3,29	1,01	0,50	3,93	6,95	1,41	39,46	0,15	1,12
1376,4	14,60	0,33	0,41	0,64	4,80	0,21	1,65	0,00	6,73	0,00	62,24	0,00	8,39
1378,15	13,51	0,52	0,31	0,68	5,20	0,21	1,35	0,94	6,39	0,00	62,89	0,10	7,90
1381,2	15,25	1,41	0,68	0,65	5,90	0,14	2,30	2,87	6,68	0,00	57,08	0,37	6,68
1384,6	13,63	0,15	0,62	0,13	27,87	0,13	1,55	0,00	4,13	0,00	44,59	0,13	7,12
1388,6	11,18	0,00	0,61	0,00	31,51	0,12	1,12	0,00	3,25	0,00	44,73	0,15	7,32
1390,8	12,44	0,42	0,26	0,16	1,90	3,76	2,32	0,00	5,66	0,00	62,20	4,01	6,87
1394,6	9,87	0,72	0,45	0,48	4,99	1,31	1,78	0,15	4,89	0,00	65,36	1,30	8,68
1396,6	8,61	0,42	24,75	7,18	3,69	0,30	0,00	0,51	6,27	3,98	42,74	0,58	0,97
1398,6	10,19	0,49	0,43	0,32	3,60	11,80	3,32	0,52	4,76	0,22	49,77	9,14	5,45
1403,2	8,84	0,41	23,49	4,47	2,91	1,49	0,52	2,04	5,35	0,00	40,76	3,87	5,85
1406,6	12,20	0,32	1,23	0,00	4,87	2,52	2,63	0,15	3,73	0,00	59,50	3,50	9,35
1407,2	3,49	0,00	0,32	0,10	72,15	0,71	1,05	0,15	1,44	0,15	17,53	1,24	1,67
1410,35	8,31	0,50	15,34	5,34	19,99	0,16	0,00	0,20	3,98	1,20	41,91	0,61	2,45
1414,4	-	-	-	-	-	-	-	-	-	-	-	-	-
1417,8	17,43	0,14	1,15	0,51	4,08	0,00	2,51	0,00	4,50	0,00	61,19	0,20	8,29

APPENDIX 5: SPHAEROSIDERITES GEOCHEMICAL ANALYSES:

Table 12: Collected geochemically values from the SEM on sphaerosiderites in the center, middle and outer layers for Mg, Fe and Ca elements.

CENTER LAYER				MIDDLE LAYER				OUTER LAYER			
Point n°	Mg (%)	Fe (%)	Ca (%)	Point n°	Mg (%)	Fe (%)	Ca (%)	Point n°	Mg (%)	Fe (%)	Ca (%)
1	2,6	87,6	9,8	1	43,9	21,4	34,7	1	13,6	73,0	13,4
2	2,5	85,8	11,7	2	12,3	76,5	11,2	2	12,1	75,6	12,3
3	3,3	85,8	10,9	3	8,9	81,9	9,1	3	13,1	73,9	13,0
4	3,2	87,2	9,6	4	2,8	87,8	9,4	4	8,5	80,7	10,8
5	3,4	82,6	14,0	5	1,2	87,0	11,7	5	2,5	88,5	9,0
6	3,6	80,7	15,6	6	1,1	87,8	11,2	6	6,2	81,8	12,1
7	0,7	86,6	12,7	7	2,8	85,0	12,1	7	12,3	75,4	12,2
8	1,3	69,9	28,8	8	1,3	87,2	11,5	8	2,1	87,6	10,2
9	2,3	86,5	11,2	9	1,4	87,7	10,9	9	15,9	71,5	12,6
10	2,8	83,7	13,5	10	1,5	88,1	10,4	10	6,6	81,0	12,4
11	1,0	74,0	25,0	11	1,2	86,8	12,0	11	8,2	80,2	11,5
12	2,4	85,1	12,5	12	0,7	89,3	10,1	12	9,6	79,7	10,7
13	1,5	84,8	13,7	13	1,1	89,1	9,8	13	14,4	73,8	11,7
14	0,8	66,6	32,6	14	0,9	90,3	8,7	14	11,2	80,6	8,1
15	4,0	87,2	8,8	15	1,6	88,2	10,2	15	6,5	82,1	11,5
16	1,0	82,1	16,9	16	1,2	90,4	8,4	16	11,5	76,5	12,1
17	0,9	85,0	14,1	17	1,3	87,3	11,4	17	11,9	76,7	11,4
18	2,0	76,1	21,9	18	1,2	89,0	9,8	18	13,3	75,1	11,6
19	2,4	86,7	10,9	19	2,5	86,8	10,8	19	11,8	74,6	13,6
20	2,3	50,7	47,0	20	5,6	85,1	9,3	20	16,3	72,5	11,2
21	1,3	60,3	38,4	21	6,5	83,8	9,6	21	15,7	72,2	12,1
22	3,0	89,7	7,4	22	5,2	86,1	8,7	22	9,4	81,5	9,0
23	1,8	89,6	8,5	23	6,7	82,2	11,1	23	18,0	70,2	11,8
24	2,6	90,0	7,4	24	2,9	89,5	7,6	24	17,2	71,3	11,5
25	5,1	82,3	12,5	25	4,1	88,7	7,2	25	7,9	82,9	9,2
26	1,1	67,8	31,2	26	3,7	86,2	10,0	26	18,7	70,7	10,7
27	1,6	83,4	14,9	27	6,1	84,0	9,8	27	8,3	83,1	8,6
28	0,8	44,2	55,0	28	1,6	86,2	12,3	28	3,2	89,3	7,5
29	1,0	85,5	13,4	29	7,3	84,6	8,1	29	8,8	82,1	9,0
30	1,5	87,3	11,2	30	6,4	84,6	8,9	30	16,1	71,2	12,7
31	1,0	82,8	16,2	31	6,5	84,0	9,5	31	17,3	69,8	12,9
32	1,1	70,6	28,3	32	6,8	82,8	10,4	32	6,1	84,8	9,2
33	4,0	85,9	10,1	33	4,5	87,8	7,8	33	15,3	72,3	12,4
34	1,4	86,6	12,0	34	7,5	81,5	11,0	34	16,8	71,4	11,7
35	2,5	90,4	7,0	35	6,1	82,5	11,4	35	15,9	73,6	10,5
36	2,2	90,8	6,9	36	5,9	86,3	7,8	36	6,8	84,5	8,6
37	1,5	56,1	42,3	37	4,4	84,7	10,8	37	13,4	75,7	10,8
38	5,4	74,4	20,2	38	8,2	85,2	6,5	38	13,1	76,1	10,8
39	1,4	76,8	21,8	39	8,1	83,6	8,3	39	9,4	79,3	11,3
40	4,1	69,0	26,9	40	7,9	84,0	8,2	40	9,1	82,1	8,9
41	1,5	67,3	31,2	41	5,4	84,3	10,3	41	7,9	80,2	11,9
42	1,5	53,8	44,7	42	6,6	83,9	9,5	42	15,3	72,5	12,2
43	1,9	51,0	47,0	43	8,5	83,8	7,7	43	16,1	70,7	13,2
44	1,6	75,6	22,8	44	8,5	82,2	9,4	44	7,7	80,0	12,3
45	1,7	79,8	18,5	45	3,5	84,0	12,5	45	7,6	80,5	11,9
46	3,7	89,8	6,5	46	4,7	85,7	9,6	46	10,8	77,0	12,1
47	3,7	90,8	5,5	47	7,6	85,0	7,4	47	15,5	71,0	13,5
48	1,5	75,8	22,7	48	8,1	84,8	7,1	48	8,6	79,2	12,2
49	3,2	87,6	9,3	49	6,0	85,7	8,3	49	15,5	71,9	12,6
50	1,1	48,6	50,3	50	8,7	84,2	7,1	50	8,4	79,5	12,0
51	1,1	58,9	40,0	51	8,6	82,2	9,2	51	18,4	70,2	11,4
52	1,9	86,7	11,4	52	6,2	86,7	7,1	52	2,6	87,4	10,0
53	1,5	89,7	8,8	53	2,6	86,0	11,4	53	8,3	81,4	10,3
54	2,6	87,9	9,4	54	6,2	85,5	8,3	54	7,8	80,9	11,3
55	4,8	81,3	14,0	55	2,6	87,9	9,4	55	4,0	84,1	11,9
56	4,0	91,6	4,4	56	6,6	86,1	7,3	56	2,7	85,8	11,5
57	3,0	84,7	12,4	57	6,5	84,6	8,8	57	2,3	87,8	9,9
58	1,4	53,2	45,4	58	6,8	85,0	8,1	58	2,6	85,9	11,5
59	4,7	88,5	6,8	59	4,9	83,9	11,1	59	2,6	86,0	11,4
60	4,5	90,8	4,7	60	4,6	84,9	10,5	60	2,3	88,2	9,5
61	5,9	85,3	8,7	61	2,8	86,0	11,2	61	3,1	87,0	9,9
62	1,2	84,1	14,7	62	7,4	82,7	9,9	62	2,9	85,9	11,3
63	6,6	84,9	8,5	63	2,8	86,4	10,7	63	3,8	85,2	11,0
64	2,8	88,8	8,4	64	8,3	84,8	6,9	64	7,8	80,8	11,3
65	3,2	89,6	7,1	65	5,1	87,5	7,4	65	2,7	87,4	10,0
66	0,9	83,2	15,9	66	7,3	84,8	7,9	66	4,4	83,7	11,9

Table 13: Collected geochemically values from the SEM on sphaerosiderites in the center, middle and outer layers for Mg, Mn and Ca elements.

CENTER LAYER				MIDDLE LAYER				OUTER LAYER			
Point n°	Mg (%)	Mn (%)	Ca (%)	Point n°	Mg (%)	Mn (%)	Ca (%)	Point n°	Mg (%)	Mn (%)	Ca (%)
1	18,4	12,0	69,6	1	54,4	2,6	43,0	1	48,8	3,3	47,9
2	16,0	8,5	75,5	2	50,9	2,8	46,4	2	47,9	3,5	48,6
3	21,6	7,1	71,3	3	48,4	2,1	49,5	3	48,4	3,6	48,0
4	23,3	6,8	69,9	4	22,3	3,2	74,4	4	42,1	4,5	53,4
5	15,3	22,7	62,0	5	9,2	3,6	87,1	5	20,2	8,0	71,7
6	13,1	30,6	56,3	6	8,1	6,8	85,1	6	32,4	4,5	63,1
7	4,4	17,0	78,6	7	17,8	5,3	76,9	7	49,3	1,9	48,9
8	2,5	41,6	56,0	8	9,5	2,9	87,5	8	15,7	9,4	74,9
9	13,7	20,1	66,2	9	10,6	4,7	84,6	9	55,0	1,3	43,7
10	13,8	19,3	66,9	10	12,1	4,0	83,9	10	33,5	3,8	62,7
11	2,4	38,9	58,7	11	8,3	8,2	83,5	11	40,5	2,6	56,9
12	13,0	19,9	67,1	12	5,5	12,3	82,2	12	46,6	1,3	52,1
13	8,3	17,8	73,9	13	10,2	3,5	86,4	13	53,9	2,2	43,9
14	1,4	41,7	56,9	14	8,8	10,8	80,4	14	48,0	17,1	34,8
15	28,0	10,3	61,7	15	13,2	3,1	83,7	15	34,8	3,4	61,9
16	4,0	28,8	67,2	16	11,5	7,0	81,5	16	47,6	2,2	50,2
17	5,3	11,0	83,7	17	9,2	7,4	83,3	17	50,4	1,4	48,2
18	5,2	38,4	56,4	18	9,9	6,0	84,1	18	52,4	2,0	45,6
19	14,8	18,8	66,3	19	17,8	4,9	77,3	19	45,8	1,3	52,9
20	3,0	35,3	61,6	20	36,7	1,9	61,4	20	57,9	2,5	39,6
21	2,0	35,7	62,3	21	39,0	3,7	57,3	21	55,4	2,0	42,6
22	25,7	10,4	63,9	22	35,5	5,1	59,4	22	49,5	3,2	47,3
23	13,6	23,3	63,1	23	36,5	3,2	60,4	23	59,2	2,1	38,7
24	22,6	13,8	63,6	24	25,5	6,7	67,8	24	59,4	0,9	39,7
25	27,9	3,7	68,4	25	33,9	5,7	60,3	25	45,1	2,6	52,4
26	2,0	38,1	59,8	26	26,1	4,0	70,0	26	62,4	1,9	35,7
27	6,3	36,3	57,4	27	36,7	4,4	58,9	27	45,9	6,3	47,8
28	0,9	33,5	65,6	28	9,6	16,8	73,6	28	27,0	10,3	62,7
29	4,8	33,4	61,8	29	44,7	5,1	50,1	29	47,6	3,9	48,5
30	7,9	32,2	59,9	30	40,6	3,1	56,3	30	54,8	1,8	43,4
31	3,6	38,5	57,8	31	40,2	1,3	58,6	31	56,5	1,2	42,3
32	2,3	38,0	59,7	32	38,7	2,7	58,6	32	38,1	4,4	57,5
33	26,4	6,4	67,3	33	35,3	3,4	61,3	33	54,6	1,0	44,4
34	8,8	17,1	74,0	34	39,2	3,4	57,3	34	57,8	1,8	40,4
35	21,7	17,9	60,3	35	34,4	1,2	64,4	35	58,7	2,7	38,6
36	18,4	24,2	57,3	36	41,0	5,5	53,6	36	42,5	4,0	53,5
37	2,1	39,2	58,7	37	25,6	11,7	62,6	37	53,4	3,5	43,1
38	14,0	33,3	52,7	38	52,7	5,4	41,9	38	53,6	2,4	44,0
39	3,4	42,2	54,4	39	47,3	4,4	48,3	39	44,4	2,4	53,2
40	7,9	40,0	52,0	40	47,2	3,7	49,1	40	48,2	4,6	47,2
41	2,6	42,2	55,2	41	32,9	4,6	62,5	41	39,7	0,6	59,7
42	2,0	37,0	61,0	42	39,7	3,4	56,9	42	54,4	2,1	43,5
43	2,5	36,2	61,2	43	50,1	4,7	45,2	43	54,4	1,2	44,4
44	3,7	42,5	53,8	44	45,4	4,6	50,1	44	38,1	1,3	60,6
45	5,3	37,1	57,6	45	19,6	10,0	70,4	45	38,7	1,0	60,3
46	23,6	35,5	40,9	46	30,7	6,9	62,4	46	45,9	2,9	51,2
47	28,5	29,5	42,0	47	48,3	4,3	47,4	47	53,0	1,1	45,9
48	3,5	45,0	51,6	48	51,6	3,4	44,9	48	40,7	1,8	57,4
49	15,2	39,8	44,9	49	40,4	3,1	56,5	49	54,7	0,6	44,7
50	1,3	36,5	62,2	50	50,3	8,3	41,4	50	41,1	0,5	58,4
51	1,6	39,2	59,1	51	47,2	2,3	50,5	51	61,2	0,7	38,1
52	9,6	33,3	57,2	52	43,6	6,6	49,8	52	19,4	5,3	75,2
53	9,2	36,2	54,6	53	17,3	5,1	77,6	53	43,5	2,5	54,0
54	15,1	30,8	54,1	54	40,9	4,8	54,3	54	39,7	2,6	57,7
55	24,1	5,1	70,8	55	20,0	8,1	72,0	55	24,5	2,5	73,0
56	41,1	12,8	46,1	56	45,3	4,8	49,8	56	17,7	6,3	76,0
57	14,1	26,9	59,0	57	40,6	4,6	54,8	57	17,2	7,4	75,4
58	1,9	37,5	60,6	58	43,3	5,2	51,5	58	17,5	6,0	76,5
59	34,3	15,9	49,7	59	29,3	4,6	66,1	59	17,7	5,9	76,4
60	43,2	11,4	45,5	60	28,4	7,0	64,5	60	17,6	8,8	73,6
61	39,1	3,3	57,6	61	18,8	5,1	76,1	61	22,3	5,8	71,9
62	4,4	42,4	53,1	62	40,9	5,0	54,2	62	19,1	5,7	75,2
63	41,9	4,7	53,4	63	19,7	5,7	74,6	63	25,3	1,8	72,9
64	16,9	32,7	50,4	64	45,4	16,6	38,0	64	40,4	1,1	58,5
65	19,6	37,5	42,9	65	38,3	6,8	54,9	65	19,9	6,6	73,6
66	66,5	7,4	84,8	66	46,2	4,2	49,6	66	26,3	2,9	70,8